University of California
Los Angeles

An Indirect Search for Dark Matter with VERITAS

A dissertation submitted in partial satisfaction
of the requirements for the degree
Doctor of Philosophy in Astronomy

by

Matthew Dunseth Wood

2010

The dissertation of Matthew Dunseth Wood is approved.

L. Vese

D. Saltzberg

S. Furlanetto

V.V. Vassiliev, Committee Chair

University of California, Los Angeles

2010

To my parents.

Table of Contents

List of Figures

List of Tables

Acknowledgments

I would first like to thank my adviser Vladimir Vassiliev who has very patiently guided me through my development as a scientist in the last six years. His input and feedback in the course of my thesis research have been invaluable, and it has truly been a privilege to work with him. I am especially grateful for his help in editing this thesis. I would also like to thank Rene Ong for his supervision during my first year and the guidance he has provided during my graduate school career.

I would like to thank the past and present members of the UCLA VERITAS group, Amanda, Steve, Pratik, Ozlem, Ken, and Tim, who have contributed to a stimulating and enjoyable work environment. Thanks to Steve for teaching me everything I know about programming and C++ and especially for his enomorous contribution in writing the analysis code that was integral to completing this thesis. Thanks to Amanda for her patience and all of her help and feedback on topics both hardware- and science-related. Thanks to Tim for being a great officemate during these past two years.

I would like to thank everyone who contributed to the construction and operation of VERITAS. Working together on VERITAS and seeing it come to fruition has been a tremendously rewarding experience. Thanks to the staff, students, and postdocs at the Whipple Observatory – especially Jeremy Perkins and Ken Gibbs who were always working tirelessly behind the scenes to keep VERITAS running smoothly. Thanks to all the members of the VERITAS collaboration. It has been a pleasure working with you.

Finally I'd like to thank my parents who have always loved and supported me. Without their encouragement, I would not have been able to achieve what I have in life.

Vita

1981	Born, Stony Brook, New York, USA.
1999–2003	University of Chicago
2003	B.A. Physics with specialization in Astrophysics, University of Chicago.
2003-2004	Research Assistant, Northwestern University, Evanston, IL, USA
2004–2010	University of California, Los Angeles
2004–2005	Teaching Assistant, Department of Physics and Astronomy, UCLA.
2005–2010	Research Assistant, Department of Physics and Astronomy, UCLA.
2006	M.S. Astronomy, University of California, Los Angeles.
2010	Ph.D. Astronomy, University of California, Los Angeles.

Publications

Acciari, V. A. et al., VERITAS Search for VHE Gamma-ray Emission from Dwarf Spheroidal Galaxies, 2010, The Astrophysical Journal, 720, 1174.

Wood, M. D. et al., A Search for Dark Matter Annihilation with the Whipple 10 m Telescope, 2008, The Astrophysical Journal, 678, 594.

Abstract of the Dissertation

An Indirect Search for Dark Matter with VERITAS

by

Matthew Dunseth Wood

Doctor of Philosophy in Astronomy

University of California, Los Angeles, 2010

Professor V.V. Vassiliev, Chair

Dark matter (DM) is a fundamental component of the standard cosmological paradigm known as ΛCDM and is believed to be the dominant form of matter in the Universe. Although the existence of DM is supported by a variety of observational evidence, the particle constituent of DM remains unknown. Weakly Interacting Massive Particles (WIMPs) are a generic DM particle candidate that satisfy the observed properties of DM and are independently motivated by extensions to the Standard Model (SM) of particle physics. The self-annihilation or decay of WIMPs is generically expected to produce showers of stable secondary particles including gamma-rays with energies up to the rest mass of the WIMP. This thesis reports the observation of ten sources conducted with the Very Energetic Radiation Imaging Telescope Array System (VERITAS) to search for the gamma-ray signature of WIMPs. Upper limits on the gamma-ray flux from these sources are reported and used to infer constraints on the particle physics properties of the WIMP.

CHAPTER 1

Introduction

One of the great successes of modern astrophysics has been the development of a standard cosmological paradigm that provides a model for the evolution of the Universe on large scales (much larger 1 Mpc) from $t \sim 10^{-3}$ s to the present day. However, the understanding of the underlying nature of several key components of this cosmological picture is currently incomplete. Based on a variety of observational data, the currently accepted model of the Universe is one that includes two invisible components – dark matter (DM) and dark energy. Thus far we have only succeeded in studying these components indirectly through their gravitational influence. The identity of DM and dark energy remains a mystery and is currently the object of intense scientific research.

This thesis presents the results of an indirect search for the particles composing DM undertaken with the Very Energetic Radiation Imaging Telescope Array System (VERITAS) – a ground-based observatory sensitive to gamma-ray photons in the very-high-energy (VHE) regime above 100 GeV. The existence of DM is supported by multiple sources of evidence encompassing observations that extend from cosmological scales to individual galaxies. There is significant scientific reason to believe that DM is not composed of ordinary matter such as leptons, baryons, and photons. For example, many promising DM particle candidates are motivated by extensions to the Standard Model (SM) of particle physics. This chapter describes the diversity of astrophysical evidence that supports the cur-

rent model of DM and reviews some of the most theoretically favored candidates for the DM particle. The chapter concludes with a discussion of the experimental techniques that are currently used to search for the DM particle and the specific role of DM searches with VHE gamma rays.

1.1 Cosmological Evidence

The most widely accepted theory for the origin and evolution of the Universe is the Big Bang model. According to this model, the Universe began approximately 10^{10} years ago from a hot dense state in thermodynamic equilibrium from which it has subsequently expanded. The Big Bang model is supported by several key pieces of observational evidence: the homogeneity and isotropy of the Universe on large scales, the redshift of distant galaxies, and the existence of the cosmic microwave background (CMB). During the last decade, cosmological data of increasing sensitivity and precision have led to the development of more quantitative cosmological theories that are built on the Big Bang framework. The current most widely accepted theory is the cosmological concordance model known as ΛCDM.

In the ΛCDM model the current energy density of the Universe is divided among three main components: baryonic matter, cold dark matter (CDM), and dark energy. Baryonic matter consisting primarily of the constituents of normal atoms (protons, neutrons, and electrons) comprises only 5% of the total energy density while DM and dark energy comprise 23% and 72% respectively. To the precision of current measurements, the properties of dark energy are consistent with a *cosmological constant*, Λ, with an equation of state corresponding to a vacuum energy density, while the DM component is best modeled as a cold collisionless fluid. In the following sections the theoretical framework of the ΛCDM

model and the cosmological data that provide the strongest evidence for DM are briefly outlined. These data probe the dynamics of the Universe over a wide range of times and physical states from the epoch of Big Bang Nucleosynthesis (BBN) ($t \sim 100$ s) to recombination ($t \sim 10^5$ yr) and the subsequent era of galaxy formation and dark-energy accelerated expansion ($t \gtrsim 10^9$ yr).

1.1.1 Friedmann-Robertson-Walker Cosmology

The ΛCDM cosmology is founded on general relativity and the assumption of homogeneity and isotropy on large scales. The most general spacetime metric satisfying these conditions is the Friedmann-Robertson-Walker (FRW) metric,

$$ds^2 = c^2 dt^2 - a(t)^2 \left[\frac{dr^2}{1 - kr^2} + r^2 \left(d\theta^2 + \sin^2 \theta d\phi^2 \right) \right], \tag{1.1}$$

where (r, θ, ϕ) are comoving spherical coordinates, $a(t)$ is the *scale factor* describing the size of the Universe with cosmic time ($a = 1$ at present), and k is a constant describing the spatial curvature ($k = 0, -1, +1$ for universes that are flat, negatively curved, and positively curved respectively). The evolution of the scale factor for a universe containing components with a total energy density ρ and relativistic pressure p is determined by the equations of general relativity which reduce to the two Friedmann equations,

$$H^2 \equiv \left(\frac{\dot{a}}{a} \right)^2 = \frac{8\pi G}{3c^2} \rho - \frac{kc^2}{R_0^2 a^2}, \tag{1.2}$$

$$\left(\frac{\ddot{a}}{a} \right) = -\frac{4\pi G}{3c^2} \left(\rho + 3p \right), \tag{1.3}$$

where R_0 is the current radius of curvature and H is the Hubble parameter. The Hubble parameter describes the rate of change of the scale factor and its current value, the *Hubble Constant*, has a measured value, $H_0 = 100h$ km s^{-1} Mpc^{-1} with $h = 0.742 \pm 0.036$ (Riess et al., 2009). Through the Friedmann equations

the energy/matter content of the Universe directly influences its spatial curvature and dynamics. A universe with a total energy density equal to the *critical density*,

$$\rho_c \equiv \frac{3c^2 H_0^2}{8\pi G}, \tag{1.4}$$

has a spatially flat metric ($k = 0$). It is customary to measure the energy density of different components of the Universe in units of the critical density usually denoted as $\Omega(t) = \rho(t)/\rho_c$. In terms of the present-day density parameter, Ω_0, the first Friedmann equation can be rewritten as

$$\left(\frac{\dot{a}}{a}\right)^2 \frac{1}{H_0^2} = \Omega(t) + \frac{1 - \Omega_0}{a^2}. \tag{1.5}$$

There are several components contributing to the energy density of the Universe at present: non-relativistic matter ($\Omega_{m,0}/a^3$) with equation of state $p = 0$, radiation ($\Omega_{r,0}/a^4$) with equation of state $p = \rho/3$, and dark energy ($\Omega_{\Lambda,0}$) for which energy density remains constant with equation of state $p = -\rho$. In the context of the cosmological studies, the scale factor a is frequently expressed through the redshift, $1 + z = 1/a$.

1.1.2 Cosmic Microwave Background

Perhaps the strongest evidence for DM comes from the study of the cosmic microwave background (CMB) fluctuations. During the epoch of recombination ($z \sim 1100$), electrons and protons combined to form neutral hydrogen atoms causing the Universe to become suddenly transparent to photons. This radiation which became decoupled from thermodynamic equilibrium with electrons and protons is known as the CMB. The CMB has a nearly perfect blackbody radiation spectrum with $T = 2.725$ K and temperature fluctuations (anisotropies) present at the scale of 10^{-5}. These anisotropies are the signature of acoustic sound waves in the photon-baryon fluid at recombination that were driven by

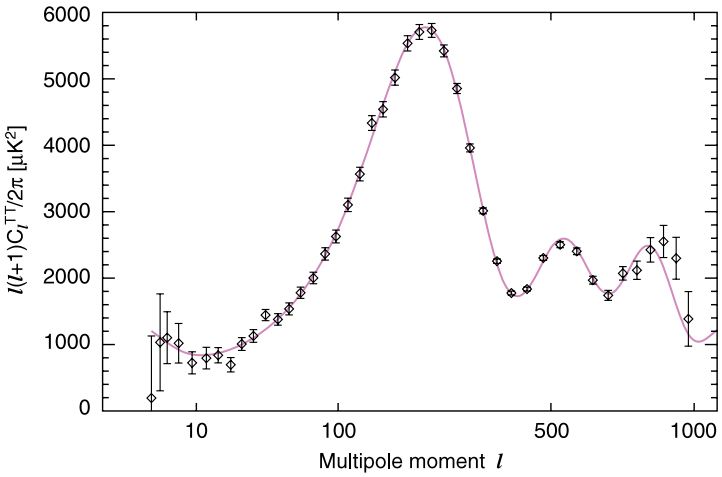

Figure 1.1 CMB angular power spectrum measured using the five-year WMAP data set. The solid line indicates the best fit ΛCDM model with ($\Omega_m h^2$, $\Omega_b h^2$, h) = $(0.131, 0.0227, 0.724)$. Figure taken from Nolta et al. (2009).

perturbations in the gravitational potential. After the photons decoupled, the phases of the acoustic modes were frozen and appear today as a series of peaks and troughs in the observed angular power spectrum (see Figure 1.1). Analysis of the positions and amplitudes of the peaks can be used to constrain a variety of cosmological parameters including the ratio of DM to baryon energy density at the time of recombination. From the analysis of the five-year WMAP data set (Komatsu et al., 2009), the best fit parameters for the energy density in baryons, matter, and dark energy assuming a ΛCDM cosmological model are

$$\Omega_b h^2 = 0.02273 \pm 0.00062 \quad \Omega_m h^2 = 0.1326 \pm 0.0063 \quad \Omega_\Lambda h^2 = 0.742 \pm 0.030, \tag{1.6}$$

indicating the existence of a significant non-baryonic matter component in the Universe primarily responsible for the gravitational potential perturbations at the epoch of recombination.

1.1.3 Big Bang Nucleosynthesis

Big bang nucleosynthesis (BBN) is the epoch during which the expansion of the Universe reduced the rate of the interaction between protons, neutrons, and neutrinos thereby freezing the abundances of the light elements such as deuterium (D), helium-3 (^{3}He), helium-4 (^{4}He), and lithium-7 (^{7}Li). These relic abundances are sensitive to the total baryonic content of the Universe through the ratio of the number density of baryons to photons expressed in terms of the baryon-to-photon ratio parameter $\eta_{10} \equiv n_b/n_\gamma \times 10^{10}$. BBN began when the temperature of the Universe was cool enough to allow the formation of deuterons ($\sim 10^9$ K). Free neutrons were rapidly converted to ^{4}He through a sequence of reactions involving D, ^{3}He, and ^{3}H. The production of ^{4}He continued until $T \sim 10^8$ K ($t \sim 10^3$ s) when the temperature became insufficient to sustain further reactions, leaving a small residual fraction of unprocessed D and ^{3}He. The relic abundance of ^{7}Li is determined by a more complex chain of reactions. After BBN, the relic abundances of the light elements remained frozen until the epoch of star formation when these primordial abundances were altered by stellar nucleosynthesis. The sensitivity of the light element abundances to η_{10} arises because a higher baryon-to-photon ratio allows BBN to start earlier resulting in a more efficient production of ^{4}He and lower abundances of D and ^{3}He. If all interactions during BBN are described by the SM of particle physics, the relative abundances of the light elements can be predicted to high accuracy as a function of η_{10} (see Figure 1.2).

Among the light elements produced during BBN, deuterium has the greatest sensitivity to η_{10}. Deuterium is destroyed but not created by stars and thus any measurement of the deuterium abundance sets a strict lower limit on the relic abundance. The best estimates of the relic deuterium abundance come from the study of neutral hydrogen absorbers in the emission spectra of distant

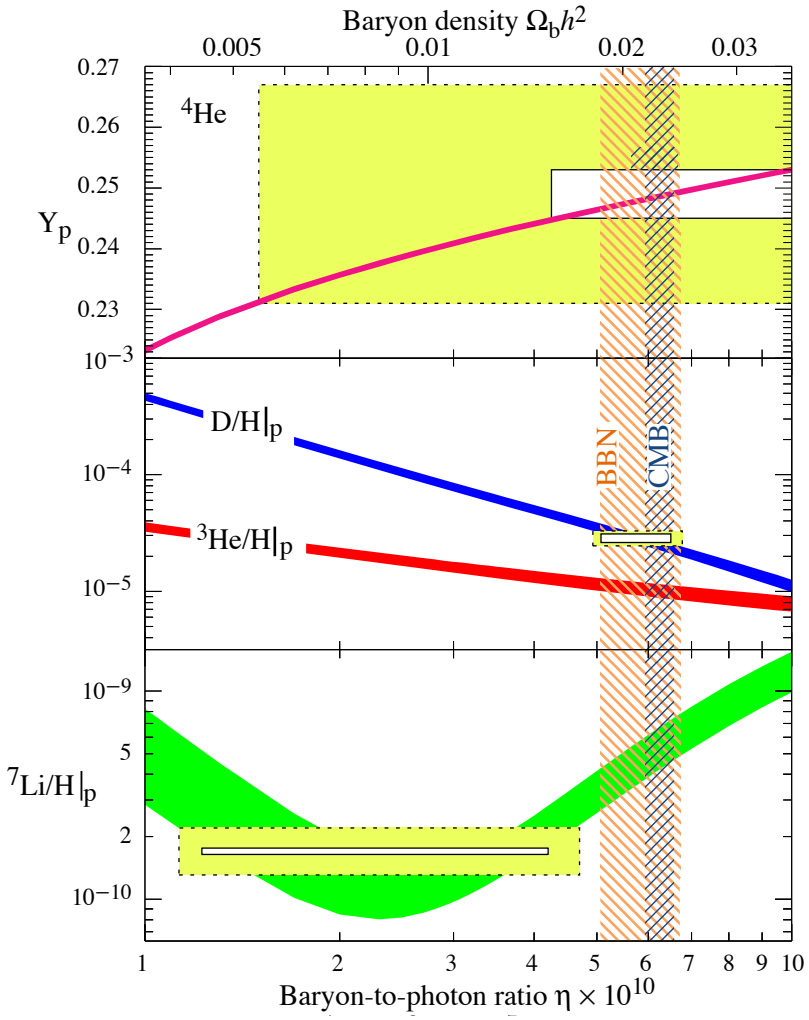

Figure 1.2 Predicted abundances of D (blue), ^{3}He (red), ^{4}He (purple), and ^{7}Li (green) as a function of the baryon-to-photon ratio (η). The width of each band indicates the theoretical uncertainty in its calculation. Hashed vertical bands show the 95% C.L. interval on η inferred from BBN abundances and CMB measurements. Figure taken from Particle Data Group et al. (2008).

quasars. An average of the measured deuterium abundances from six quasar systems indicate a value of $\eta_{10} = 6.0 \pm 0.4$ (Steigman, 2007) that corresponds to an energy density in baryons of $\Omega_b h^2 = 0.0219 \pm 0.002$. If the Universe is assumed to be flat ($\Omega_0 = 1$) as implied by measurements of the CMB, baryonic matter cannot comprise more than $\sim 5\%$ of the total energy density of the Universe and an additional non-baryonic component is required. This value is in remarkable agreement with energy density in baryons measured by WMAP.

1.1.4 Large Scale Structure

The observed large scale distribution of galaxies also requires a significant non-baryonic component. According to the standard theory of structure formation, the structures that exist today in the form of stars, galaxies, and clusters of galaxies grew from initial perturbations in the gravitational potential that are thought to be seeded by quantum fluctuations during epoch of inflation. As the Universe evolved from this initial inflationary state, the regions with a density higher than the average background density (expressed in terms of the density contrast $\delta(\mathbf{x}) = (\rho(\mathbf{x}) - \langle\rho\rangle)/\langle\rho\rangle$) were able to grow due to gravitational collapse. During the matter-dominated epoch, density fluctuations grew as $(1+z)^{-1}$ until $\delta \sim 1$ when they entered a non-linear regime in which they collapsed and formed gravitationally bound structures.

In a universe containing only baryonic matter, the growth of density perturbations on scales less than a Jeans mass is inhibited prior to recombination by the coupling of matter and radiation. The amplitude of the temperature fluctuations in the CMB implies that the largest density contrasts in baryonic matter at the time of recombination had an amplitude of $\sim 10^{-5}$. In a matter-dominated universe, these density contrasts could only grow by a factor of 10^3 between re-

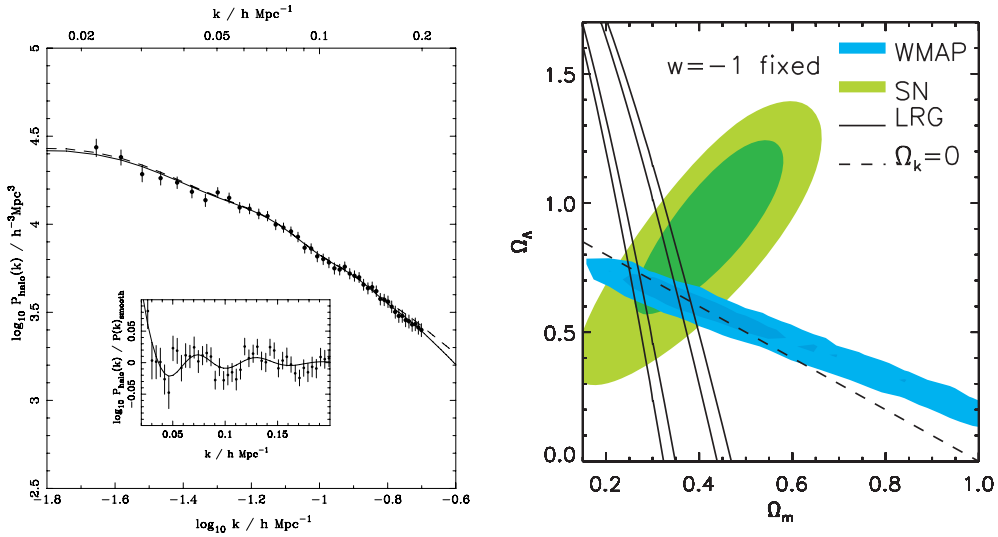

Figure 1.3 **Left:** Reconstructed power spectrum of the DM halo density field traced by luminous red galaxies (LRGs) in the SDSS Seventh Data Release. Solid black line shows the best-fit ΛCDM model to both the SDSS LRG sample and the five-year WMAP data set with $(\Omega_m, \Omega_b, \Omega_\Lambda) = (0.291, 0.0474, 0.709)$. Figure taken from Reid et al. (2010). **Right:** Comparison of independent constraints on $(\Omega_m, \Omega_\Lambda)$ inferred from the SDSS LRG sample (black lines), WMAP five-year data set (blue shaded contours), and the Union type Ia supernovae data set (Kowalski et al., 2008) (green shaded contours). Figure taken from Reid et al. (2010).

combination ($z \sim 1100$) and today which is insufficient to form the present-day structures with $\delta \gg 1$. The existence of DM provides a simple solution to this problem. Because DM decouples from radiation at early times, density fluctuations in DM could begin growing during the epoch of matter-radiation equality. After recombination, the baryons collapsed into the existing density perturbations of DM, and the baryon density perturbations rapidly grew to the same amplitude as the DM perturbations. Recent studies of the matter power spectrum measured by large redshift surveys such as the Sloan Digital Sky Survey (SDSS; York et al. 2000) have allowed structure formation models incorporating DM to be tested more quantitatively (see Figure 1.3). With the assumption of a flat universe, the analysis of the matter spectrum measured from the luminous red galaxy (LRG) sample in the SDSS Data Release 7 implies $\Omega_m h^2 = 0.14 \pm 0.01$. As shown in Figure 1.3 the region in the $(\Omega_m, \Omega_\Lambda)$ parameter space preferred by measurements of large scale structure is in good agreement with the independent constraints derived from the CMB (Komatsu et al., 2009) and surveys of type Ia supernovae (Kowalski et al., 2008).

1.2 Astrophysical Evidence

Observations of gravitationally bound systems have long supported the existence of a significant nonluminous matter component in the Universe. The earliest evidence for DM is attributed to Fritz Zwicky who observed a velocity dispersion for galaxies in the Coma cluster that was much larger than would be expected from the luminous matter in this system (Zwicky, 1933). Despite these early observations, the DM hypothesis was not widely accepted until the detailed measurements of galactic rotation curves (Rubin & Ford, 1970) that demonstrated a significant DM component in spiral galaxies. The presence of DM has since been

clearly identified in a variety of systems spanning a wide range of spatial scales from the dwarf galaxies to galaxy clusters. For a review of the observational evidence for DM see Bertone et al. (2005).

1.2.1 Spiral Galaxies

Prior to the advent of precision cosmological measurements, the observation of the rotation curves of spiral galaxies provided some of the strongest evidence for the existence of DM. The visible matter in a spiral galaxy can be modeled in terms of both a bulge and disk component with the mass in the disk component falling exponentially as a function of distance from the center. Stars and gas in the disk travel in approximately circular orbits around the galactic center and these motions can be used to study the mass enclosed at each radius,

$$M(r) = \frac{v_c(r)^2 r}{G}, \tag{1.7}$$

where G is Newton's gravitational constant and $v_c(r)$ is the circular velocity at radius r. In principle the rotational velocity can be measured with any luminous tracer of the matter distribution. Measurements of galactic rotation curves are typically carried out by observing the spectral lines associated with the rotational transitions of CO and the 21 cm line of neutral hydrogen (HI).

If the gravitational potential of the galaxy is dominated by visible matter, the velocity curve should decline as $r^{-1/2}$ at the periphery of the galaxy when the enclosed mass of the luminous matter saturates. However, observations of many spiral galaxies have found rotation curves that are flat or rising with radius out to the visible extent of the disk. These observations suggest that spiral galaxies are embedded in a large DM halo. Figure 1.4 illustrates the measured rotation curve of the nearby spiral galaxy M33.

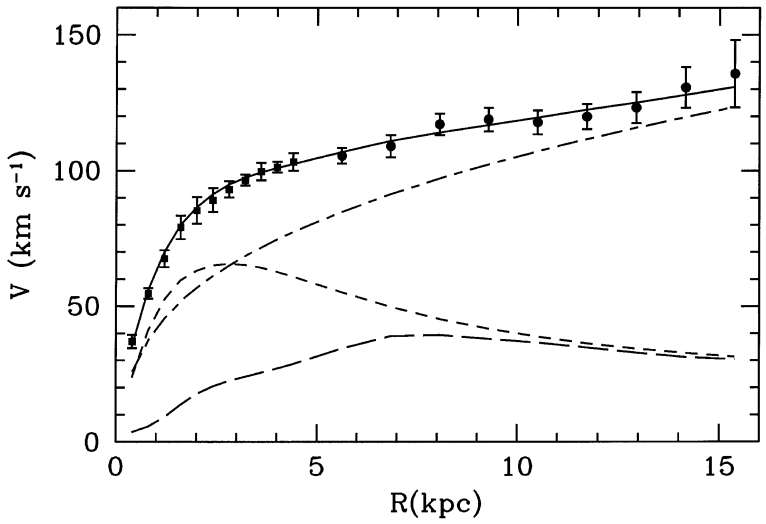

Figure 1.4 Rotation curve (points) of the spiral galaxy M33 measured with 21 cm transition of HI. The solid curve indicates the best fit model for the measured rotation curve with contributions from a DM halo (dot-dashed line), a stellar disk (short dashed line), and a gaseous disk (long dashed line). Figure taken from Corbelli & Salucci (2000).

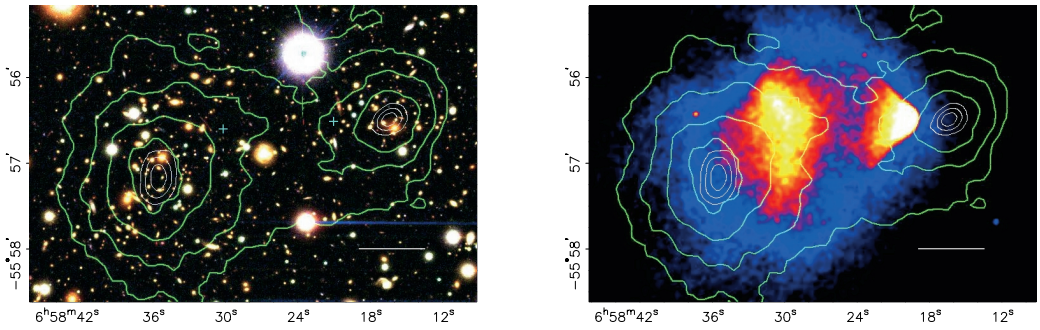

Figure 1.5 Optical (**left**) and x-ray (**right**) images of the merging galaxy cluster 1ES 0657-558. Green contours indicate the surface mass density reconstructed from the gravitationally lensed background galaxies. Figure taken from Clowe et al. (2006).

1.2.2 Merging Galaxy Clusters

Perhaps the most compelling evidence for the existence of DM on non-cosmological scales comes from the observation of several unique colliding galaxy clusters (Clowe et al., 2006; Bradač et al., 2008). In these systems, the majority of the baryonic mass is present in the form of hot x-ray emitting intracluster plasma. As the galaxy clusters collide the plasma responds to pressure forces while the collisionless stars pass through unimpeded resulting in a spatial separation between these two components. The "Bullet cluster" 1E 0657-558 was one of the first such systems in which this separation could be clearly observed (Clowe et al., 2006). The projected mass density profile of the system inferred from gravitational lensing of background galaxies by the foreground galaxy cluster (see Figure 1.5) shows a clear offset between the gravitational mass and the main baryonic plasma component in the system. This observation demonstrates that the dominant mass component in this system must be in some invisible and collisionless form. A

second merging cluster system, MACS J0025.41222, has been subsequently observed to demonstrate a similar separation between the dominant gravitational and baryonic mass components (Bradač et al., 2008).

1.2.3 Dwarf Spheroidal Galaxies

The dwarf spheroidal (dSph) galaxies of the Milky Way (MW) are the smallest and least luminous galaxies in which DM has been unambiguously detected. The dSphs are faint satellites of the MW having stellar luminosities $< 10^7 L_\odot$ and are characterized by old, metal-poor stellar populations. The majority of dSphs are found at a distance of 20–100 kpc from the MW enabling detailed studies of their internal kinematics from the line of sight motions of individually resolved stars. The stellar velocity dispersions in these systems are much greater than would be inferred from the distribution of luminous matter implying the presence of an extended DM halo. The number of known dSphs has significantly grown in recent years with the discovery of a new population of very low luminosity systems (10^3–10^4 $L_\odot$) (Willman et al., 2005; Irwin et al., 2007; Belokurov et al., 2007) with data from the SDSS. Despite being significantly fainter than previously known systems, these *ultrafaint* dSphs appear to have DM halo of similar mass to larger systems (Strigari et al., 2008a; Walker et al., 2009) and thus have extremely high mass-to-light ratios, $M/L \sim 1000$.

1.3 DM Candidates

Although there is overwhelming astrophysical evidence for the existence of DM, its particle constituent is unknown. The astrophysical data impose significant constraints, however, on the properties of a plausible candidate DM particle. The

combination of measurements of CMB anisotropies, light element abundances from BBN, and large scale structure of the Universe indicate that DM must be in a non-baryonic form that was cold (non-relativistic) during the structure formation epoch. Furthermore the total energy density in DM particles must satisfy the relic density required by ΛCDM, $\Omega_{DM}h^2 = 0.1131 \pm 0.0034$ (Komatsu et al., 2009). This second constraint implies that the DM particle must be stable with a lifetime exceeding or at least comparable to the age of the Universe. To prevent efficient interaction of DM particles through electromagnetic channels and the formation of anomalous heavy isotopes that have been excluded by direct searches, the DM particle should also preferably be neutral (Taoso et al., 2008).

1.3.1 Weakly Interacting Massive Particles

There are many particle candidates proposed from theoretical considerations that satisfy the properties of astrophysical DM (Taoso et al., 2008). However several favored candidates discussed in this thesis are additionally motivated by cosmological considerations. For example, a thermal relic of the early Universe with a mass and interaction cross section on the weak scale will naturally produce the present-day DM density. Such a candidate is generically referred to as a weakly interacting massive particle (WIMP). The relic density of WIMPs is determined by the process of freeze-out when the rate of the interactions of the WIMPs through which they are coupled to the other components of the Universe becomes smaller than the rate of the expansion of the Universe (Kolb & Turner, 1990). This occurs when $T \simeq m_{\rm WIMP}/20$ indicating that the WIMP at the decoupling time is non-relativistic. Prior to freeze-out, the chemical potential of WIMPs must be equal to zero and therefore the equilibrium number density of

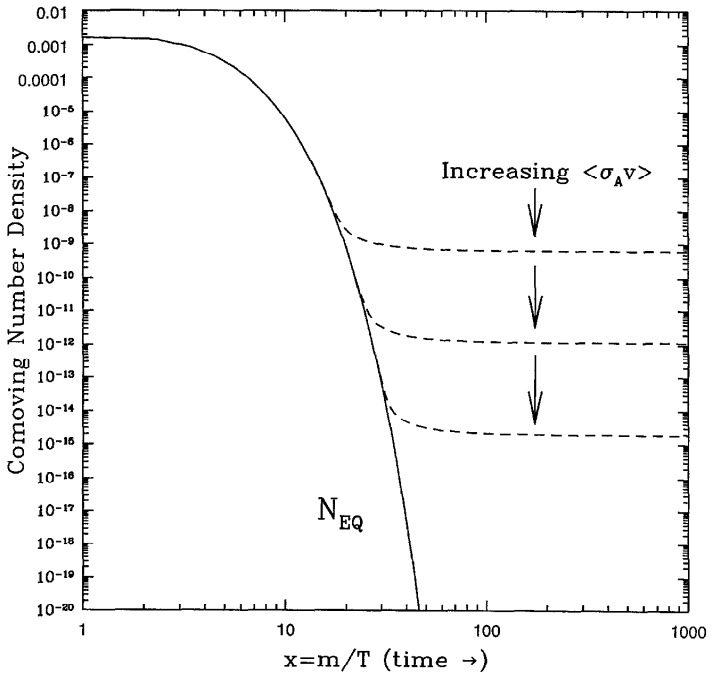

Figure 1.6 Evolution of the comoving number density of WIMPs as a function of inverse temperature in units of the WIMP mass. The solid line indicates the equilibrium solution for WIMP number density while the three dashed lines illustrate the freeze-out densities for three values of the thermally averaged annihilation cross section. Figure taken from Jungman et al. (1996).

WIMPs declined exponentially with temperature according to

$$n^{eq} = g\left(\frac{m_{\rm WIMP}kT}{h^2}\right)^{3/2}\exp\left(-\frac{m_{\rm WIMP}c^2}{kT}\right), \tag{1.8}$$

where g is the number of internal degrees of freedom of the WIMP. The equilibrium number density was maintained until the rate of WIMP interactions dropped below the expansion rate of the Universe ($\Gamma \lesssim H$) at which point the number density was frozen. The simplified time evolution of the WIMP number density, n, during freeze-out is governed by the Boltzmann equation,

$$\frac{dn}{dt} + 3Hn = \langle\sigma_A v\rangle\left[n^2 - (n^{eq})^2\right] \tag{1.9}$$

where H is the hubble expansion rate and $\langle\sigma_A v\rangle$ is the thermally averaged cross section for WIMP self-annihilation. Numerical solutions for the WIMP number density versus temperature for different values of $\langle\sigma_A v\rangle$ are illustrated in Figure 1.6. As the thermally averaged annihilation cross section is increased, the relic density of WIMPs drops. An approximate relationship between the relic density and the annihilation cross section for a particle with a weak-scale mass (Jungman et al., 1996) is given by

$$\Omega_{\rm WIMP}h^2 \simeq \frac{3\times10^{-27}\ {\rm cm}^3\ {\rm s}^{-1}}{\langle\sigma_A v\rangle}. \tag{1.10}$$

Thus to first order the WIMP relic density is independent of mass, and a cross section on the order of the weak scale is needed to produce the observed relic density. An upper bound on the WIMP mass comes from the unitarity limit on the thermal relic, $m_{\rm WIMP} \lesssim 120$ TeV (Griest & Kamionkowski, 1990). Accelerator searches for the WIMP suggest a lower bound of $m_{\rm WIMP} \gtrsim 10$ GeV (Bottino et al., 2003).

The SM of particle physics describes elementary particles of matter and their interactions in terms of the strong, weak, and electromagnetic forces. The SM

is in excellent agreement with experimental data collected at particle colliders, and therefore a successful DM particle candidate should fit into the framework of SM or its possible extensions. The weakly-interacting neutrino is the only known SM particle that could be considered as a possible DM candidate. However, the cosmological constraint on the energy density of all left-handed neutrinos of $\Omega_\nu h^2 < 0.0072$ from CMB observations (Komatsu et al., 2009) excludes neutrinos from constituting the majority of DM. Because the light weakly-interacting neutrinos would be hot (relativistic) during structure formation, their non-dominant contribution to DM is also consistent with observational evidence from structure formation (Section 1.1.4). Although a weakly-interacting neutrino is not compatible with the characteristics of the WIMP, several possibilities within extensions to the SM exist. Two of the most well-developed frameworks for physics beyond the SM are Supersymmetry (Section 1.3.3) and Universal Extra Dimensions (Section 1.3.4) both of which predict potential WIMP candidates.

1.3.2 Axions

Independent of the observational evidence for DM there are strong reasons to believe that the SM is incomplete and part of a more fundamental theory that would predict the existence of new particles. Axions are a non-WIMP DM candidate that were originally proposed to explain the absence of CP violation in strong interactions and provide a mechanism for the vanishingly small dipole moment of the neutron (Peccei & Quinn, 1977; Dress et al., 1977). Although the existence of the axion is motivated by particle physics, it becomes a viable candidate for DM if its mass is in the range 10^{-6}–10^{-2} eV. Axions with masses above this range are excluded by laboratory searches, stellar evolution constraints, and models for the neutrino emission from SN1987A. In order for very light axions to constitute

cold DM they must be produced non-thermally. The misalignment mechanism (Preskill et al., 1983) is an example of such a production mechanism for axions in the early Universe and results in an axion relic density of

$$\Omega_a h^2 \simeq 0.3 \left(\frac{6\ \mu\text{eV}}{m_a} \right)^{7/6}, \tag{1.11}$$

where m_a is the axion mass (Particle Data Group et al., 2008). An axion produced via this mechanism is therefore expected to have $m_a \simeq 10\ \mu$eV in order to have the correct DM relic density ($\Omega_a h^2 \simeq 0.1$). However other non-thermal production mechanisms could satisfy the DM relic density constraint for significantly larger or smaller axion masses. The best constraints on cosmological axions come from the Axion Dark Matter Experiment (ADMX) which uses a microwave cavity to search for the conversion of axions to microwave photons and has ruled out interesting regions of axion parameter space in the mass range 1.9–3.53 μeV (Asztalos et al., 2010). Although axions are a well-motivated DM candidate, the signatures of their interaction with ordinary matter are outside of the detectability range of the experimental techniques utilized in this thesis.

1.3.3 Supersymmetric DM Candidates

The theory of supersymmetry (SUSY) is an extension to the SM in which particles with the required properties of the WIMP can often emerge naturally. SUSY is based on the only known nontrivial symmetry relating the properties of spacetime bosons and fermions that has not been experimentally discovered. A consequence of this symmetry is that every particle in the SM must have a *superpartner* with spin differing by 1/2 unit. One of the original theoretical motivations for SUSY was its ability to address the hierarchy problem of the SM – the large difference between the electroweak (~ 100 GeV) and the Planck ($\sim 10^{19}$ GeV) energy scales. Radiative corrections to the mass of the SM Higgs boson (the only particle in the

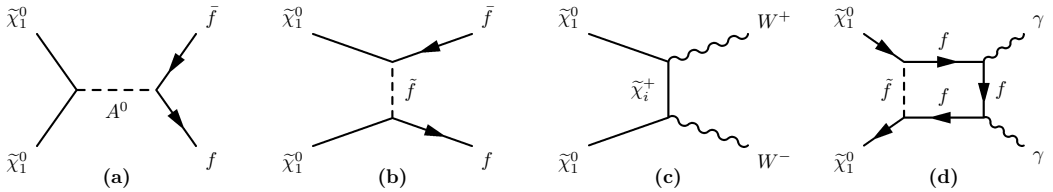

Figure 1.7 Representative diagrams contributing to the annihilation of the neutralino: s-channel pseudoscalar higgs boson (A^0) exchange to fermions (**a**), t-channel sfermion ($\tilde{f}$) exchange to fermions (**b**), t-channel chargino exchange to W bosons (**c**), and one loop t-channel sfermion exchange to two photons (**d**). Feynman diagrams reproduced from Jungman et al. (1996) and Bergström & Ullio (1997).

SM model that has not been discovered) lead to a quadratic divergence that is constrained at a high energy scale where new physics is assumed to appear. The introduction of new scalar superpartners in SUSY at approximately the Higgs boson mass scale cancels this quadratric divergence (Haber & Kane, 1985). Another motivation for SUSY theories is that they provide a mechanism to unify the gauge coupling constants of the strong, weak, and electromagnetic forces at a single high energy scale. Such a unification is critical for grand unified theories that seek to incorporate the fundamental forces into a larger gauge group (Georgi & Glashow, 1974). Because no supersymmetric particles have been detected, supersymmetry is assumed to be a broken symmetry with supersymmetric particle masses at some higher energy scale. If supersymmetry is associated with the origin of the electroweak scale, it is natural for the supersymmetric particle masses to be $\sim$TeV.

The simplest realization of SUSY is the minimal supersymmetric extension of the standard model (MSSM) (for a review see Haber & Kane 1985) that intro-

duces the minimum number of new particles to the SM:

- A set of spin-0 superpartners to the quarks and leptons referred to as *squarks* and *sleptons*.
- A set of spin-1/2 superpartners to the SM gauge bosons, the *gluinos* ($\tilde{g}$), *winos* ($\tilde{W}^{\pm}, \tilde{W}^{0}$), and *binos* ($\tilde{B}$), which are collectively referred to as *gauginos*.
- Two SM spin-0 complex higgs doublets, $H_d = (H_d^0, H_d^-)$ and $H_u = (H_u^0, H_u^+)$, giving mass to down-type and up-type fermions respectively.
- Two charged and two neutral spin-1/2 *higgsinos* ($\tilde{h}^{\pm}$, $\tilde{h}^{0}_{1,2}$).

The supersymmetric fermionic states with the same quantum numbers mix to produce the following mass eigenstates:

- Four *neutralinos* ($\tilde{\chi}^0_1$, $\tilde{\chi}^0_2$, $\tilde{\chi}^0_3$, $\tilde{\chi}^0_4$) which are linear combinations of the binos, winos, and neutral higgsinos.
- Two pairs of *charginos* ($\tilde{\chi}^{\pm}_1$, $\tilde{\chi}^{\pm}_2$) which are linear combinations of the winos and charged higgsinos.

In order not to violate experimental limits on the lifetime of the proton, the MSSM also imposes a new discrete symmetry known as R-parity (Dimopoulos & Georgi, 1981). Supersymmetric particle have $R = -1$ while SM particle have $R = 1$. The conservation of R-parity in interaction and decay processes guarantees that the lightest supersymmetric particle (LSP) will be stable and thus makes it a plausible DM candidate (Ellis et al., 1984).

The MSSM does not provide an explicit model for the mechanism of supersymmetry breaking but instead introduces a set of soft (low-energy) supersymmetry-breaking terms in the Lagrangian that are treated as free parameters of the model.

Including all couplings, masses, and mixing angles, the fully unconstrained MSSM has more than 100 free parameters. A simplification of the large MSSM parameter space can be achieved by adopting a specific renormalization procedure that relates the full MSSM parameter space at low energies (∼TeV scale) to a reduced parameter set defined at high energies (unification scale). A widely considered SUSY framework of this type is minimal supergravity (mSUGRA) (Nilles, 1984) in which SUSY breaking is mediated by gravitational effects. This framework reduces the full MSSM to five parameters: a scalar unification mass (m_0), a gaugino unification mass ($m_{1/2}$), a universal trilinear coupling constant (A_0), the ratio of the vacuum expectation value of the two Higgs fields ($\tan\beta$), and the sign of the higgsino mass parameter (sign(μ)). Alternatively a purely phenomenological approach to setting MSSM parameters can be adopted (pMSSM) that does not provide a mechanism for SUSY-breaking but assigns common values to the low-energy SUSY parameters. A specific realization of the pMSSM used in this work is the seven parameter set defined by the DarkSUSY package (Gondolo et al., 2004).

Two of the most frequently considered DM particle candidates within the MSSM are the gravitino ($\tilde{G}$), the spin-3/2 superpartner of the graviton, and the lightest neutralino ($\tilde{\chi}_1^0$). Because the gravitino coupling is suppressed by the Planck energy scale, its interaction and annihilation rates would be extremely weak making direct experimental detection of relic DM particles impossible. Gravitinos with the correct relic density can be produced thermally if they are very light ($m_{\tilde{G}} \simeq 100$ eV) and would constitute warm DM at the time of structure formation (Pagels & Primack, 1982). However, observational constraints from structure formation which imply $m_{\tilde{G}} \gtrsim 2$ keV (Seljak et al., 2006) currently disfavor these models. Heavy gravitinos ($m_{\tilde{G}} \simeq 1$ TeV) would satisfy the cold DM requirement and could be produced by late decays of the next-to-lightest

supersymmetric particle (NLSP) (Feng et al., 2004).

The lightest neutralino has the best prospects for experimental detection and is generically expected to be the LSP in the mSUGRA framework. Hereafter in this thesis the term neutralino is used to refer to the lightest neutralino ($\chi \equiv \tilde{\chi}_1^0$). Since neutral vector fields are self-conjugate, the corresponding supersymmetric partners (e.g. the neutralinos) are Majorana fields and self-annihilate. The neutralino has couplings suppressed at the weak energy scale and therefore could potentially be detected through either self-annihilation or scattering off of nucleons. The leading neutralino self-annihilation channels are those to fermion-antifermion pairs and gauge boson pairs (see Figure 1.7).

1.3.4 Universal Extra Dimensions

Another proposed extension to the SM that generically predicts the existence of WIMPs are theories of Universal Extra Dimensions (UED). In these theories, all SM particles propagate in one or more compact extra dimensions with a compactification radius R. For UED models with a single extra dimension, precision electroweak measurements constrain $R^{-1} \gtrsim 300$ GeV (Appelquist et al., 2001). As a result of the existence of these compactified extra dimensions, every SM particle has an associated set of excited states, Kaluza-Klein (KK) excitations, with identical SM quantum numbers and masses $m \sim nR^{-1}$ where n is the excitation quantum level. Momentum conservation in the extra dimensional space leads to conservation of KK parity which in analogy to R-parity in SUSY models makes the lightest KK-excited particle (LKP) stable and thus a potentially good DM candidate. The most promising candidate for the LKP is the first KK excitation of the B hypercharge gauge boson denoted as $B^{(1)}$. The $B^{(1)}$ can generically satisfy constraints on the DM relic density generated through the thermal freeze-out

process if its mass is in the range 500–800 GeV (Servant & Tait, 2003). A recent review of the phenomenology of UED models is given in Hooper & Profumo (2007).

1.4 DM Searches

The task of identifying the WIMP particle has motivated several complementary experimental techniques. Particle accelerators such as the Large Hadron Collider (LHC) can potentially discover WIMPs by direct production in collisions with a center of mass energy greater than the rest mass of the WIMP (for a review see Feng 2010). Direct detection experiments search for WIMP-nucleon recoils using low-background detectors (for a review see Spooner 2007). Finally, indirect dark matter searches use ground- or space-based detectors to search for the secondary particles produced by the annihilations or decays of WIMPs (for a review see Bertone et al. 2005). Ideally the unambiguous identification of the WIMP would be achieved using multiple techniques. The conclusive association between a WIMP particle candidate discovered at the LHC and astrophysical DM would require its detection through direct or indirect methods. Indirect detection of the WIMP with gamma rays in principle allows the direct association of WIMP particle properties with DM properties in astrophysical systems. The search for VHE gamma-ray signatures from WIMP self-annihilation is the prime focus of this thesis.

1.4.1 Accelerator Searches

The detection of new physics signatures in particle accelerator experiments may provide evidence for the nature of DM. Searches for supersymmetric particles at

the e^+e^- collider LEP at CERN set lower limits on the masses of charged supersymmetric particles in the range 80–100 GeV (Particle Data Group et al., 2008). Within the mSUGRA framework with unified gaugino masses, these constraints imply $m_\chi \gtrsim 50$ GeV (Bottino et al., 2004). The currently operating LHC with a center-of-mass design energy of 14 TeV should be sensitive to new particles at the TeV scale. However, since the WIMP is stable and weakly-interacting, direct production of WIMP pairs is invisible and the detection of the other direct production signatures is challenging (Feng, 2010). In the case of SUSY, the best detection prospects would arise from the production of heavier superparticles that would decay via a cascade of quark and gluon jets to the LSP. These events should be detectable at LHC by searching for signatures of missing transverse energy. Because the center-of-mass energy in each LHC interaction is unknown, the extraction of precise masses and cross sections of the LSP which would allow the unambiguous identification with DM is challenging. Baltz et al. (2006) showed that for some optimistic SUSY benchmark scenarios the LHC could measure the mass of the neutralino to 5–10% accuracy and place a constraint on its relic density of ∼50%. If LHC discovers signatures of SUSY, the precise determination of the properties of the supersymmetric particles would be best accomplished with a future high-energy e^+e^- collider such as the proposed International Linear Collider (Baltz et al., 2006). Because of the difficulties of WIMP identification and characterization in accelerator searches, complementary search techniques are critical.

1.4.2 Direct Detection

A widely pursued method of direct detection of WIMP DM is to search for the signatures of the interactions of these particles with ordinary matter such as

nuclear recoils in terrestrial detectors. The energy transferred to nucleons in these interactions can be detected through the ionization, scintillation, or heat (phonons) generated in the detecting medium. Assuming an isotropic distribution of WIMPs with an RMS velocity 230 km s^{-1} characteristic of the gravitational potential of the Milky Way at the location of Earth, the anticipated kinetic energies of the WIMPs are $\sim$ 50 keV for a 100 GeV WIMP and would impart energies of 10s of keV in these recoils. In general, the scattering cross section can be divided into spin-dependent and spin-independent terms. The latter is proportional to the atomic mass of the nucleus and is expected to give the dominant contribution to the detection rate for the majority of WIMP models. Because the anticipated detection rates are extremely low ($<$ 1 event kg^{-1} day^{-1}), low background operation and large detection mass are critical. To achieve these requirements, the majority of current direct dark matter detectors employ at least two detection signatures and are typically located in deep underground facilities to reduce background from cosmic rays. Unlike the annihilation cross section, the WIMP-nucleon scattering cross section is not expected to be directly connected to the DM relic density and therefore is WIMP model-dependent. For instance, scans of the mSUGRA parameter space have found models satisfying the DM relic density with spin-independent cross sections spanning a large range, 10^{-6}–10^{-12} pb (Ellis et al., 2005; Roszkowski et al., 2007). It is possible to generate SUSY models for which the annihilation cross section is effectively zero.

Current direct detection experiments have achieved a sensitivity to spin-independent interaction cross sections of $\sim 10^{-7}$ pb (10^{-43} cm^2) and are probing regions of the parameter space for supersymmetric WIMP models (see Figure 1.8). The Cryogenic Dark Matter Search (CDMS) uses solid-state cryogenic Ge and Si detectors to measure both ionization and phonon signatures of WIMPs. An experiment that uses a similar technique is EDELWEISS (Sanglard et al., 2005).

CDMS-II has reported the best limits on the WIMP cross section of $< 4 \times 10^{-8}$ pb for a WIMP mass of 70 GeV. Another class of direct detection experiments use noble liquids such as liquid xenon as a detection medium and measure simultaneously the prompt scintillation photons and ionization generated by nuclear recoils. The XENON10 (Aprile et al., 2009) and ZEPLIN III (Lebedenko et al., 2009) experiments are both examples of detectors of this type and have reported limits of comparable sensitivity to CDMS-II.

The DAMA experiment which searches for the scintillation signature of WIMPs using low-background NaI crystals is the only experiment to have reported a signal that could be interpreted as DM. The DAMA collaboration report an annual modulation in their data with a statistical significance of 8.9σ which is consistent with the expected modulation in the WIMP velocity due to the orbital motion of the Earth (Bernabei et al., 2008). Although the DAMA result was originally believed to be in contradiction with other experimental limits, recent theoretical work has shown that it may be compatible with a very low mass WIMP ($m_\chi \sim 10$ GeV) which would evade the bounds set by other experiments (Petriello & Zurek, 2008; Savage et al., 2009a,b). However, the mass and nucleon scattering cross section of such a WIMP is outside of the conventional region of parameter space predicted by SUSY. Ultimately the confirmation of the DAMA result can only be achieved by the measurement of the compatible signature in an independent experiment. Future direct detection experiments such as SuperCDMS (Schnee et al., 2005) and XENON100 (Aprile & XENON Collaboration, 2010) should have a sensitivity to spin-independent cross sections in the regime 10^{-9}–10^{-10} pb and should significantly clarify the experimental picture.

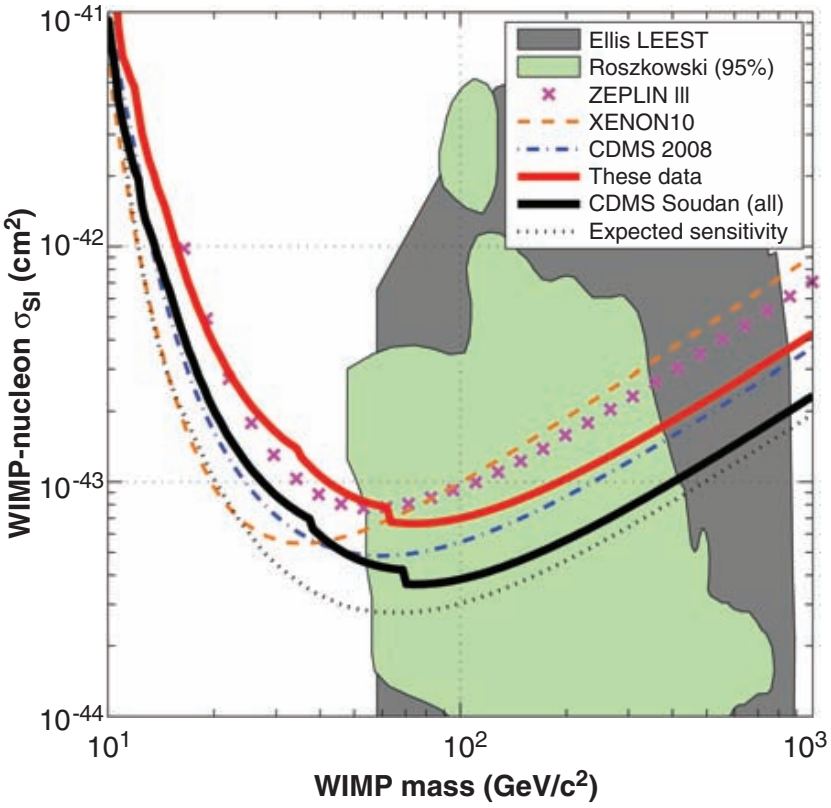

Figure 1.8 Comparison of upper limits on the WIMP-nucleon spin-independent cross section as a function of WIMP mass. The solid black line, dashed orange line, and purple crosses show the limits obtained by the CDMS-II (CDMS II Collaboration, 2010), XENON10 (Aprile et al., 2009), and ZEPLIN III (Lebedenko et al., 2009) experiments respectively. Shaded regions indicate the allowed parameter space for certain SUSY models. Figure taken from CDMS II Collaboration (2010).

1.4.3 Indirect Detection

The indirect detection of DM can potentially be achieved by searching for any of the secondary particles produced by WIMP annihilations, interactions, or decays. If they are Majorana particles, WIMPs can annihilate into fermion and gauge boson pairs that hadronize into showers of secondary particles. The long-lived charged secondaries (electrons, positrons, protons, antiprotons, etc.) diffuse through galactic magnetic fields from the production site to the Solar System. Neutral secondaries such as gamma rays and neutrinos are unperturbed by magnetic fields and thus can be mapped back to the source of annihilation whether in the galaxy or extragalactic. Enhanced neutrino fluxes can also be produced in the cores of the Sun and Earth due to capture of WIMPs in the gravitational wells of these bodies by the WIMP-nucleon scattering (Bergström et al., 1998a). By studying the fluxes of these cosmic-ray species at Earth, the signatures consistent with DM could be identified.

The detection of several unusual features in the high energy ($E > 10$ GeV) cosmic-ray electron and positron spectra has recently stimulated the debate about a possible DM origin. The PAMELA satellite (Picozza et al., 2007) reported a measurement of the positron fraction ($e^+/(e^+ + e^-)$) that shows a rapid rise between 10 GeV and 100 GeV (Adriani et al., 2009a) which is larger than predicted by models for cosmic-ray propagation (see Figure 1.9). A harder than expected total electron spectrum ($e^+ + e^-$) was also reported by the Fermi-LAT (Abdo et al., 2009a) in the 100–700 GeV regime and in the 300 GeV–1 TeV regime by H.E.S.S. (Aharonian et al., 2008a, 2009a). Taken together these measurements imply a new source of high energy electrons and positrons that could arise from either astrophysical origin or from a more exotic production mechanism such as DM annihilation. A conventional astrophysical explanation for these measure-

ments is particle acceleration by one or more nearby sources such as pulsars (Hooper et al., 2009; Yüksel et al., 2009). A WIMP interpretation (e.g. the neutralino or KK particle) is disfavored by the antiproton-to-proton ratio measured by PAMELA (Adriani et al., 2009b) as well as by the large boost factors needed for a WIMP particle with a standard weak scale annihilation cross section. Stimulated by these experimental observations various alternative DM particle models that annihilate preferentially to leptons and have cross sections enhanced by the Sommerfeld mechanism have been proposed (Cirelli et al., 2009; Cholis et al., 2009).

Among the secondary particles produced in WIMP annihilations, gamma-rays have a unique capability to relate WIMP as a particle to the astrophysical DM problem. Because gamma-rays produced in WIMP annihilations point back to the source of annihilation, astrophysical foregrounds can be significantly reduced by searching for signals in the direction of regions with a high density of DM. The rate of WIMP annihilations is proportional to the square of the local WIMP density and thus the annihilation signal is expected to be highly concentrated in the cores of DM halos. The gamma-ray spectrum of the WIMP self-annihilation also has several distinctive features: strong spectral curvature, a sharp break at the WIMP mass, and a possible enhancement at the spectral endpoint due to annihilations to mono-energetic gamma-rays as well as internal brehmsstrahlung processes (see Chapter 4 for further discussion). The sensitivity, spatial resolution, and energy resolution of the current gamma-ray ground-based observatories such as VERITAS (Weekes et al., 2002) and H.E.S.S. (Hofmann & H. E. S. S. Collaboration, 2003) and the space-based Fermi-LAT (Atwood et al., 2009) make them ideally suited to search for these features. The detection of multiple gamma-ray sources with the spectral characteristics of the WIMP would allow a conventional astrophysical origin to be conclusively ruled out.

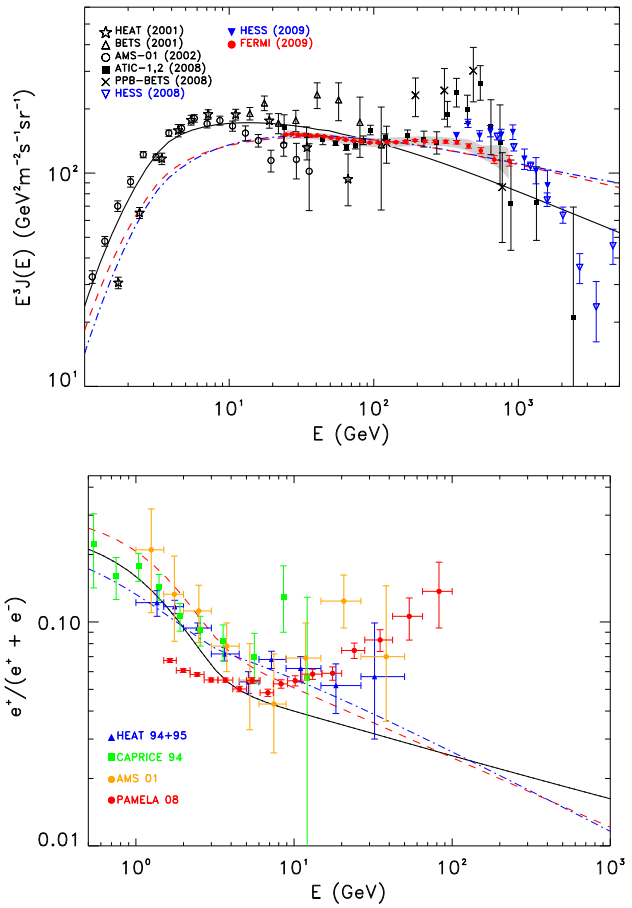

Figure 1.9 **Top:** Total cosmic-ray electron flux ($e^+ + e^-$) as a function of energy as measured by Fermi-LAT (Abdo et al., 2009a), H.E.S.S. (Aharonian et al., 2008a, 2009a), and various other experiments. The three lines show diffusive cosmic-ray propagation models generated with GALPROP (Moskalenko & Strong, 1998) using different input parameters for the cosmic-ray injection spectrum. Figure taken from Grasso et al. (2009). **Bottom:** Positron fraction ($e^+/(e^+ + e^-)$) measured by the PAMELA satellite (Adriani et al., 2009a). The three lines correspond to the same theoretical models shown in the top figure. Figure taken from Grasso et al. (2009).

The most promising nearby targets for DM searches include the Galactic Center, local group galaxies, dwarf spheroidal galaxies (dSphs) of the Milky Way, and the cores of galaxy clusters. The cores of galactic systems are typically also the regions with the highest baryonic content, and thus an important consideration is the possibility of confusion with standard astrophysical sources. Baryons may also play a significant role in shaping the present DM density in the central regions of these objects making prediction of self-annihilation fluxes uncertain.

The Galactic Center (GC) has long been considered an attractive candidate for indirect DM searches (Berezinsky et al., 2006; Bergström et al., 1998b; Bertone et al., 2002) due to its proximity and the large central DM density inferred from stellar kinematic studies (Klypin et al., 2002; Battaglia et al., 2005; Xue et al., 2008). However the detection of DM self-annihilation is complicated by the presence of many astrophysical sources in this region. Observations by H.E.S.S. lead to the detection of a VHE source (HESS J1745-290) coincident with the GC (Aharonian et al., 2004) with a spectrum that can be described by a featureless powerlaw up to 7 TeV with an index $\Gamma \simeq 2.2$. This spectrum is incompatible with both neutralino and KK emission models (Aharonian et al., 2006). Analyses that have treated the point-source in the GC as an astrophysical power-law background have placed limits on the thermally average self-annihilation cross section of $\sim 10^{-23}$ cm^3 s^{-1} for a 1 TeV WIMP. A significant systematic involved in deriving these limits is the extrapolation of the MW halo density profile down to very small scales (< 10 pc) where large uncertainties exist due to both the limited resolution of CDM simulations and the largely unknown role of baryonic matter.

Although the robust predictions of the WIMP gamma-ray luminosity are challenging, systems with a large central baryonic content such as the cores of glob-

ular clusters and galaxies are attractive targets for DM searches. After the GC, the closest galactic nuclei of mass comparable to the Milky Way are the local group galaxies M31, M32, and M33 which are $\sim$ 100 times more distant than the GC. The globular clusters are of a comparable distance to the GC but are much less massive. Both classes of systems however are interesting in the context of scenarios in which a high concentration of baryonic matter in the cores played a significant role in enhancing the central DM density. VHE observations of M31/M32 were previously reported by HEGRA (Aharonian et al., 2003), the Whipple 10m (Wood et al., 2008), and CELESTE (Lavalle et al., 2006).

Dwarf spheroidal galaxies have been extensively studied as potential DM annihilation gamma-ray sources (Baltz et al., 2000; Tyler, 2002; Strigari et al., 2007; Bergström & Hooper, 2006; Colafrancesco et al., 2007) due to their large observed mass-to-light ratios (M/L). The shape of the DM density profiles in these systems can be directly constrained by studying their stellar kinematics (Strigari et al., 2007, 2008b; Martinez et al., 2009). Astrophysical backgrounds in these systems are expected to be negligible due to their relatively low baryonic content and lack of active star formation. Limits on the gamma-ray flux from dwarf galaxies have been reported by STACEE (Driscoll et al., 2008), MAGIC (Albert et al., 2008; Aliu et al., 2009), Whipple 10m (Wood et al., 2008), H.E.S.S. (Aharonian et al., 2008b, 2009b), and the Fermi-LAT (Abdo et al., 2010a; Scott et al., 2010).

This thesis presents the results of a search for gamma-ray emission from ten targets observed by VERITAS, and the work reported here has served as the basis for the VERITAS publication (Acciari et al., 2010). The targets selected for observations include five dwarf galaxies, two local group galaxies, and three globular clusters. Chapter 2 describes the VERITAS instrument and outlines contribution of the author to the development and construction of the VERITAS

observatory. Chapter 3 describes the procedures developed and used to analyze the data. Some of the methods explained have been significantly advanced or adapted to VHE gamma-ray astronomy for the first time. Chapter 4 discusses the general characteristics of the DM annihilation signal and the relevant considerations for estimating the DM annihilation flux from a given astrophysical source. Chapter 5 presents the core results of this work, the data analysis and the constraints on the WIMP particle that were inferred from the VERITAS observations. The summary of the place of this work in the broad studies of the nature of DM is given in the conclusion, Chapter 6.

CHAPTER 2

VERITAS Instrument

The self-annihilation of WIMP particles is generically expected to produce fluxes of gamma-rays with a broadband spectrum extending up to the rest mass of the WIMP. For the preferred WIMP mass range (10 GeV–100 TeV), the typical energy density spectrum peaks in the 1–100 GeV regime. The observation of astrophysical gamma-ray sources in this energy regime is accomplished by utilizing two types of instruments: space-based satellites and ground-based imaging atmospheric Cherenkov telescopes (IACTs).

Space-based instruments such as the former EGRET (Thompson et al., 1995) and the currently operating Fermi-LAT (Atwood et al., 2009) detect gamma-rays directly by tracking the conversion of the gamma-ray to an electron-positron pair and measuring the electromagnetic energy deposited in a calorimeter. The size of space-based instruments is significantly limited by the feasibility and cost of launching a large detector into orbit and thus they have relatively small collecting areas ($\sim$ m^2). This limitation sets a practical upper limit for observations of gamma-ray photons to $\lesssim$ 100 GeV due to rapidly falling fluxes of astrophysical gamma-rays with increasing energy. The small collection area of these instruments is partially offset by their large field-of-view ($\sim$ 2 steradians for Fermi-LAT) and high duty cycle.

The IACTs study gamma-rays with energy larger than a few 10s of GeV from the ground by imaging the Cherenkov light emitted by the electromagnetic (EM)

cascades originating when gamma-ray photons interact with the Earth's atmosphere. The EM cascade proceeds through the alternating sequence of production of electron-positron pairs and bremsstrahlung radiation. The energy of the secondary particles is rapidly reduced by these mechanisms with a simultaneous rapid increase of the number of particles in the cascade. The size of the cascade grows until the particle energies fall below the threshold at which the dominant mechanism of energy losses becomes ionization ($\sim$ 83 MeV). The height at which the the number of particles in the cascade is largest (shower maximum) depends logarithmically on the primary gamma-ray energy and for a 300 GeV photon occurs at $\sim$ 10 km. Charged particles in the EM cascade (electrons and positrons) polarize the atmosphere and emit Cherenkov radiation polarization waves if their velocity exceeds the speed of light in the medium. Cherenkov radiation is a cylindrical wave emitted at the angle $\theta = \cos^{-1}(1/(n\beta))$ with respect to the trajectory of the particle, where n is the index of refraction of the atmosphere and $\beta = v/c$. The Cherenkov light has an intrinsic differential spectrum proportional to $d\lambda/\lambda^2$. By the time these photons reach the observation level on the ground, the photons with the wavelength below 280 nm are absorbed by the atmosphere. Therefore the observable Cherenkov light is broadband and peaks at $\sim$ 330 nm.

A pool of Cherenkov light centered on the trajectory of the primary gamma-ray is formed by the sum of the Cherenkov light emitted by the secondary charged particles in the cascade. The Cherenkov angle depends on the atmospheric density and varies from nearly 0° at high alitudes (above 30–40 km) to $\sim$ 1.2° at the observation level. Because the Cherenkov light from an EM cascade is emitted by particles distributed over the cascade trajectory, the interplay between the changing Cherenkov angle and the height of the emission distributes the Cherenkov light over the pool with a characteristic radius of 130 m. This area of $\sim 10^5$ m^2 rather than the aperture of the detector determines the effective col-

lecting area of IACTs and allows efficient detection of astrophysical gamma-ray photons with energies above a few tens of GeVs.

The Whipple 10m telescope (Cawley et al., 1990) pioneered the imaging atmospheric Cherenkov technique and reported the first detection of a VHE gamma-ray source, the Crab Nebula (Weekes et al., 1989). This has been accomplished through the development of concept of imaging Cherenkov light. Cherenkov light from the cascade arrives at the observation level nearly simultaneously with the time spread of $\sim$ 6 ns. The short duration of the light shower is used to detect the faint Cherenkov flashes in the atmosphere against the night sky background (Galbraith & Jelley, 1953). A second innovation, pioneered by the HEGRA instrument (Pühlhofer et al., 2003), was the development of arrays of IACTs that could stereoscopically observe the same event. The overwhelming background of the imaging atmospheric Cherenkov technique are the isotropic cosmic rays that generate similar EM cascades and Cherenkov light showers. The stereoscopic information obtained by observation with multiple telescopes significantly increases the gamma-ray angular resolution and improves the background rejection capabilities of this technique.

The energy threshold of currently operating IACT arrays depends on the aperture of the telescopes and for 12m class instruments is in the regime 80–150 GeV. This threshold is determined by the faintest light showers that can be effectively reconstructed against the ambient night sky fluctuations requiring $\sim$ 50–100 detected photons per event. The current generation of IACT observatories have achieved a gamma-ray flux sensitivity level of a fraction of 1% of the Crab Nebula flux in the regime around 1 TeV where the highest sensitivity is achieved.

VERITAS is an array of four imaging atmospheric Cherenkov telescopes (IACTs) located at the base camp of the Fred Lawrence Whipple Observatory

(FLWO) in southern Arizona (1268 m above sea level, N31°400'30", W110°57'07"; Weekes et al. 2002). Single telescope operations began in early 2005 with the completion of the first telescope (T1). The second and third telescopes (T2 and T3) were completed in 2006 and full four telescope operations began in April 2007. A significant upgrade to the array was undertaken in Summer 2009 with the relocation of the first telescope T1. Figure 2.1 illustrates the former and current array configurations. This thesis is based on the data collected during the period 2007–2010 when the telescope operated as a full array with both configurations. This chapter describes the main hardware and online software components of the VERITAS observatory comprising the telescope optics (Section 2.1), camera (Section 2.2), trigger system (Section 2.3), and data acquisition (DAQ) (Section 2.4).

2.1 Telescope Optics

Each VERITAS telescope has a 12 meter diameter primary reflector that utilizes the segmented Davies-Cotton (DC) optical design (Davies & Cotton, 1957). The reflector consists of a tubular steel optical support structure (OSS) onto which 342 identical hexagonal mirror facets are mounted having a total mirror area of $\sim$ 106 m^2. Each mirror facet has an edge-to-edge dimension of 61 cm and a spherical figure with a radius of curvature of 24 m. Mirrors are composed of slumped, ground, and polished glass with an aluminum coating and an anodized aluminum overcoating that achieves 85% reflectance between 280 nm and 450 nm and 92% reflectance at 320 nm (Roache et al., 2008) (see Figure 2.2). Measurements of mirror reflectivity have shown an average $\sim$ 3% loss of mirror reflectivity per year due to weathering. In order to maintain high mirror reflectivity, mirrors are continuously stripped and recoated at an on-site facility at the FLWO at a rate of $\sim$ 350 mirrors (one telescope) per year.

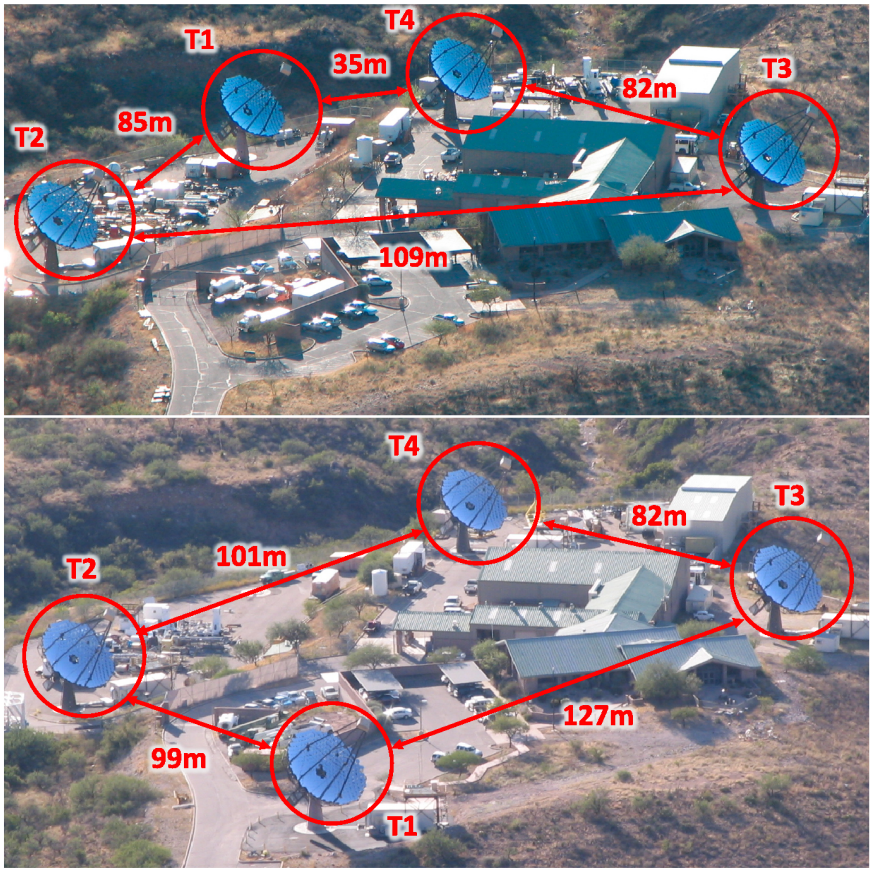

Figure 2.1 Image of the four telescope VERITAS array in its former (2007 - 2009; **top**) and current geometrical layout (2009 - present; **bottom**). Overlaid on the image is the identifying number of each telescope (T1, T2, T3, and T4) and the physical distances along the array perimeter. Photos courtesy of Steve Criswell, FLWO.

The VERITAS optical system (OS) is designed to achieve an optical point-spread-function (PSF) that at the edge of the 3.5 degree field-of-view (FoV) is approximately contained within the angular size of the camera pixels (0.15°). The finite size of the ideal VERITAS PSF arises from the contribution of both *facet* and *global* aberrations. Facet aberrations which are dominated by astigmatism scale with the inverse f-number of the individual facets ($f_{facet}/39$ for VERITAS) and can in principle be reduced by decreasing the facet size. Global aberrations dominated by coma scale with the inverse square of the f-number of the composite reflector (f/1.0 for VERITAS). The on-axis PSF FWHM (50% containment diameter) is primarily determined by the contribution of facet aberrations. The off-axis performance is dominated by global aberrations and rapidly degrades with increasing field angle (ψ) due to the effects of coma ($\sim \psi$) and astigmatism ($\sim \psi^2$). The ideal PSF of the VERITAS OS has a FWHM of 0.037° and 0.088° for a point-source at field angles of 0° and 1° respectively (Fegan & Vassiliev, 2005).

The accurate alignment of the individual mirror facets is critical to achieving a PSF approaching the ideal VERITAS PSF. Due to various non-idealities in the VERITAS OS, the FWHM of the VERITAS PSF is generally larger than its theoretical value with misalignment of individual mirror facets making the dominant contribution to the PSF spotsize (Fegan & Vassiliev, 2005). Misalignment of mirrors is caused by both limitations in the alignment technique and gravitational deformations of the OSS which change as the telescopes slew in elevation and cause mirrors to shift out of alignment. The mirror alignment is therefore optimized to achieve the best PSF spotsize at the elevation of $\sim 65°$ where most observations are made.

Prior to 2009, the alignment of the VERITAS mirrors was performed with

a laser-based alignment tool placed at the 2F point of the reflector. Mirrors were adjusted until the return beam was aligned with the outgoing beam. This technique is limited due to a varying distance from individual facets to the 2F point of the reflector and an average on-axis FWHM of $\sim 0.08^\circ$ at 65° elevation was achieved which is more than two times the ideal PSF value (0.037°). An improved alignment technique was deployed in 2009 that uses a reflector-facing wide field-of-view camera mounted in the telescope focal plane (McCann et al., 2010). Images of the individual facets of the primary reflector are taken while scanning around a bright star. Analysis of these images are used to calculate a set of adjustments to be applied to individual mirror facets. The VERITAS telescopes do not have an active mirror adjustment mechanism and are adjusted manually once every observing season. Application of the new mirror alignment technique to the VERITAS telescopes improved the optical PSF by $\sim 30\%$ achieving an on-axis FWHM of $\sim 0.06^\circ$ at 65° elevation (see Figure 2.2).

2.2 Camera

The focal plane of each telescope is instrumented with 499 Photonis XP 2970/02 photomultiplier tubes (PMTs) with a physical diameter of 2.86 cm and packed with an angular separation of 0.15° (see Figure 2.3). The PMTs have a ten-stage dynode chain with a nominal gain of 2×10^5 at 850 V. The PMT photocathode achieves a peak quantum efficiency of $\sim 25\%$ at 320 nm that approximately coincides with the peak of the Cherenkov light spectrum from atmospheric cascades detected at the ground level. The signal from each PMT anode is AC coupled and amplified by a low-noise preamplifier integrated into the PMT base with a gain of 6.66 and a bandwidth of 300 MHz. Signals from the preamplifier are transmitted to the trigger and DAQ systems (Sections 2.3 and 2.4) via a 45 m coaxial cable

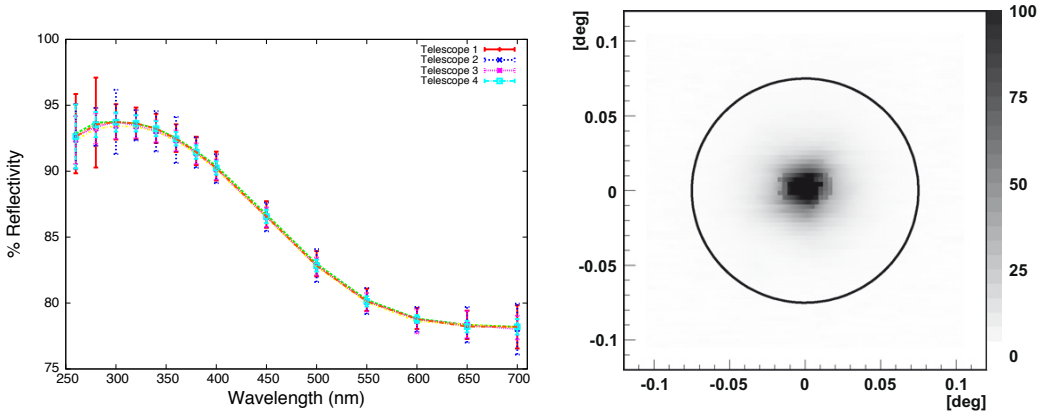

Figure 2.2 **Left:** Average mirror reflectivity of the four VERITAS telescopes as a function of wavelength. Error bars indicate the dispersion of the reflectivity of individual facets. Figure taken from Roache et al. (2008). **Right:** On-axis image of a star measured at $\sim 70^{\circ}$ elevation after mirrors were aligned with the new mirror alignment technique. The black circle indicates the size of the VERITAS PMT (0.15°). Figure taken from McCann et al. (2010).

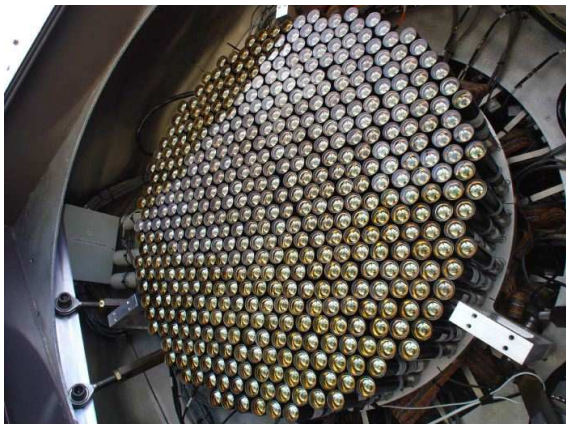

Figure 2.3 An image of the 499-pixel VERITAS camera with light concentrator plate removed.

(RG-59) which results in a signal dispersion and reduction of its peak amplitude by $\sim 25\%$. Voltage is supplied to each PMT by a commercial system consisting of two HV crates (CAEN Model SY1527 and SY2527) located in the control trailer of each telescope. The DC component from each PMT anode is fed into a current monitoring system with a resolution of 0.5 μA and a 10 Hz readout rate. The PMT operating currents are caused by night sky background and are typically in the range 3–12 μA. PMTs are automatically disabled if the instantaneous current measurement exceeds 40 μA or 30 μA for greater than 4 seconds. An array of light concentrators mounted on a flat plate is installed in the camera focal plane. The light concentrators capture a fraction of the light that would otherwise be lost in the dead space between PMTs and improve stray light control at large incident angles. Further details of the telescope optics and camera systems can be found in Holder et al. (2006).

2.3 Trigger System

VERITAS employs a three level trigger system to detect the short-duration Cherenkov flashes generated by cosmic- and gamma-ray-initiated cascades while suppressing events initiated by the night-sky background (NSB) and local muons. The efficient operation of the trigger system is critical for the detection of low-energy events ($E \lesssim 150$ GeV) that are typically dim and difficult to distinguish from noise fluctuations. In the following sections the three levels of the trigger system (L1, L2, and L3) operating at the level of the pixel, camera, and telescope array respectively are described. The inputs to the trigger system are the analog signals from the camera PMTs. A second copy of these analog signals is also fed to the DAQ system (Section 2.4). Events satisfying all trigger criteria result in the production of an L3 trigger that initiates a readout by the DAQ system.

2.3.1 Level 1 Trigger

The L1 trigger operates at the pixel level and uses a constant fraction discriminator (CFD) to generate a logic pulse when the preamplified output of a PMT exceeds a programmable threshold. This system was designed and 2500 CFD boards were fabricated at UCLA and their operation is maintained at the VERITAS observatory by the UCLA group. A schematic of the CFD circuit is shown in Figure 2.4. Logic pulses generated by the CFDs in each telescope are the input to the L2 trigger system (Section 2.3.2) and have a programmable width of 4–25 ns. An important design characteristic of the CFD is the timing jitter which sets a lower limit on the width of the resolving time window that can efficiently identify CFD pulses coincident between neighboring pixels. The conventional CFD design minimizes the timing jitter of the CFD trigger pulse by using two discriminators: threshold (TD) and zero-crossing (ZCD). A pulse that triggers the CFD must

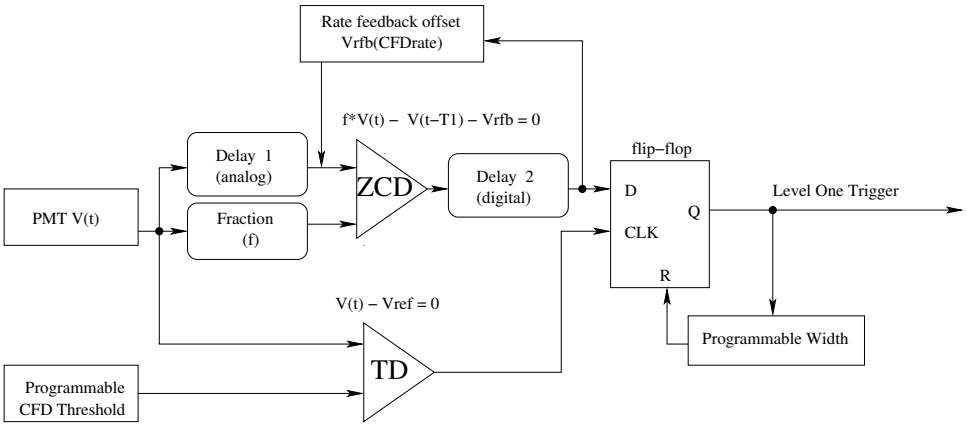

Figure 2.4 Schematic of the CFD (L1) trigger system. Figure taken from Hall et al. (2003).

trigger the ZCD while exceeding the minimum amplitude set by the TD. The circuit used to form the ZCD trigger sums an inverted copy of the input pulse delayed by 2.5 ns with a copy attenuated by the CFD fraction (0.4) and fires when the sum of these signals crosses the zero point. For a fixed pulse profile, in the absence of the NSB fluctuations this circuit generates a CFD trigger at the time independent of the pulse amplitude.

To adapt the conventional CFD to operation in the presence of the NSB fluctuations an additional circuit, the rate-feedback (RFB) loop, has been developed and implemented. The RFB circuit is a novel feature of the VERITAS CFD and dynamically adjusts the ZCD offset in response to changes in the ZCD trigger rate determined by the NSB. Three benefits are delivered by this circuit. First it dynamically minimizes the timing jitter caused by NSB, and in its absence, it functions as the ideal CFD design. Secondly, the RFB circuit stabilizes the VERITAS trigger rate against variations in the NSB rate caused by the different

night sky brightness levels in galactic or extragalactic fields or during observations conducted with partial moonlight. The strength of the RFB response is controlled by a programmable coupling constant, the RFB setting, that can be defined in the range 0–250 mV/MHz and responds to changes in the ZCD trigger rate on a time scale of $\sim$ 1 s. The third benefit is due to additional filtering capability which is brought by the CFD design allowing suppression of the CFD trigger based on the pulse time characteristics. Pulses that significantly exceed the CFD threshold always trigger the CFD regardless of their time profile. However pulses which are near the CFD threshold are rejected if the risetime of the pulse is too fast causing the amplitude of the pulse to fall below the CFD TD threshold before the ZCD has fired. Because the Cherenkov pulse has a time profile which is intrinsically broader than the narrowest pulses formed by single NSB photons, this criteria rejects a fraction of NSB pulses which exceed the CFD threshold while allowing a fraction of Cherenkov-like pulses to pass the trigger requirements.

Figure 2.5 illustrates the dependence of the total array trigger rate (L3 rate) on the CFD threshold setting for four values of the RFB setting. The total trigger rate in this figure is the sum of two contributions: a slowly rising component from cosmic-ray triggers and a steep component at low CFD thresholds from NSB triggers. Increasing the RFB setting effectively shifts the NSB component to lower threshold values without significantly impacting the rate of cosmic-ray triggers. However if RFB setting is excessively large the suppression of the cosmic-rays will occur. The RFB setting of 52 mV/MHz was adopted for full array operation in 2007 as a compromise between operation threshold and cosmic-ray trigger efficiency. The other standard operating parameters of the L1 trigger system are a threshold of 50 mV and a CFD output width of 10 ns. Investigation of the CFD performance and trigger efficiency for small cosmic-ray events has

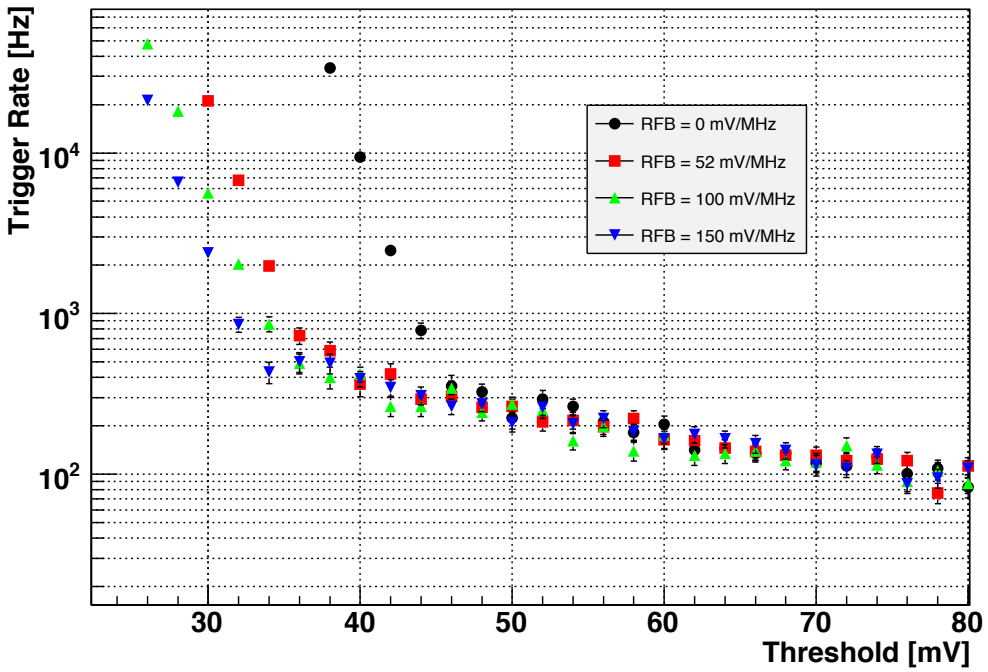

Figure 2.5 L3 trigger rate as a function of CFD threshold for four RFB settings. Figure taken from Wood et al. (2007).

been conducted and was discussed in Wood et al. (2007).

2.3.2 Level 2 Trigger

The L2 trigger operates at the camera level and requires a time coincidence of CFD triggers from at least 3 or 4 adjacent pixels, hence the name pattern selection trigger (PST) adopted for L2. CFD triggers initiated by NSB are randomly distributed in the camera, and the PST can therefore significantly suppress random triggers relative to cosmic rays that typically trigger a group of adjacent pixels. The two main components of the L2 trigger are an ECL signal splitter and a set of 19 PST modules housed in a CAMAC crate. CFD triggers from 469 of the 499 pixels are fed to the custom-built signal splitter that organizes them into 19 overlapping patches of 59 pixels. The signals from each patch are fed to 19 corresponding PST modules that use a lookup table to search for patterns of adjacent pixels on the time scale of $\sim$ 100 ns. The PST modules can be programmed to search for groups of either 3 or 4 pixels. An OR module combines the trigger signals from the 19 PST modules to form a single L2 trigger signal which is sent to the L3 trigger (Section 2.3.3). Further discussion of the L2 system developed at Leeds University, UK can be found in Bradbury & Rose (2002).

2.3.3 Level 3 Trigger

The L3 trigger operates at the the telescope array level by requiring time coincidences between the L2 triggers generated by the individual telescopes. In addition to rejecting a fraction of NSB-initiated L2 triggers, the L3 trigger significantly suppresses the rate of triggers from Cherenkov light generated by single particles, mostly muons. Muons that can trigger the L2 typically produce a bright compact image in a single telescope and thus can be efficiently rejected by requiring a time

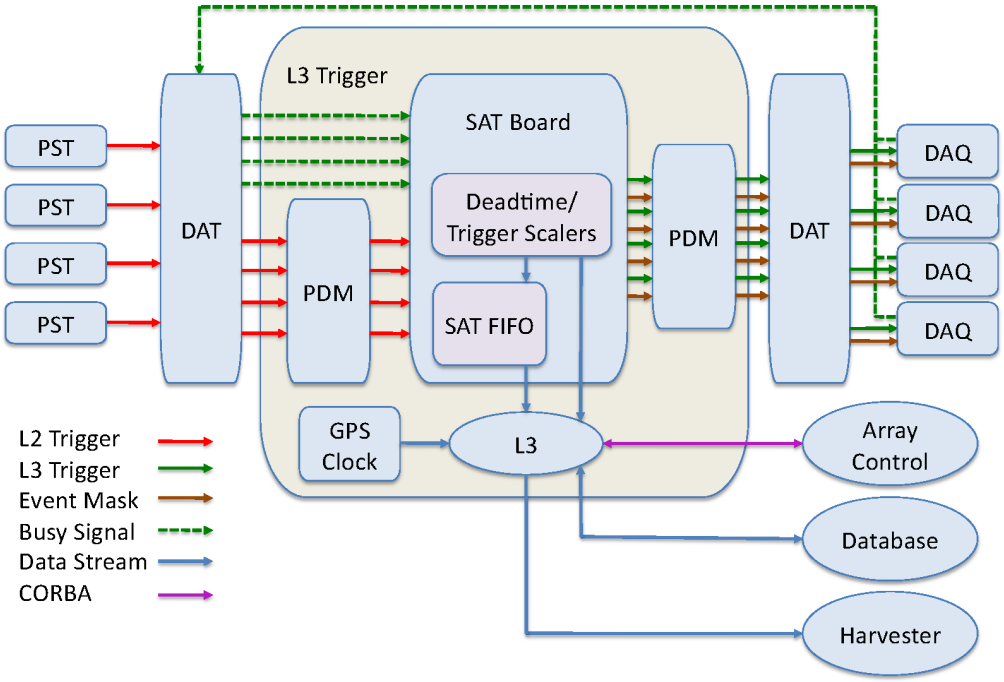

Figure 2.6 Schematic of the VERITAS L3 trigger system. Rounded rectangles and ovals represent hardware and software components respectively.

coincidence of two or more telescope triggers. As the only array-level component of the trigger system, the L3 trigger is also responsible for measuring the total instrument deadtime and monitoring the telescope (L2) trigger rates.

A schematic of the L3 trigger system is shown in Figure 2.6. Trigger signals are transmitted over the ∼80 m distance between the L3 trigger system location and the telescopes by the the Digital Asynchronous Transmission (DAT) modules (White et al., 2008). Each telescope has a receiver/tranceiver DAT module pair linked to a corresponding module pair at the L3 trigger by optical fibre. The conversion of electrical signals to optical signals is achieved using the Infineon 1.25 Gbit/s parallel optical link consisting of a 12 channel, 850 nm VCSEL driven transmitter and PIN diode-array receiver.

The L3 trigger system was developed by UCLA and McGill University, and the author of this thesis was significantly involved in its development. The main hardware components of the L3 trigger are housed in a single 6U VME crate and consist of two pulse delay modules (PDMs) that apply programmable delays to the incoming and outgoing trigger signals, the subarray-trigger (SAT) board responsible for the array/subarray trigger decision logic, a commercial GPS clock (Symmetricom TTM637), and a VME CPU controller (GE Fanuc VMIVME-7807). The software component of the L3 trigger is a persistent multi-threaded daemon process that runs on the L3 VME CPU and is primarily responsible for configuring the L3 VME modules prior to each run and updating the delay settings of the PDMs. The L3 daemon receives commands from the array control program via the CORBA protocol. The L3 CORBA interface provides methods for starting new runs, managing existing runs, and obtaining realtime run diagnostics in the form of trigger rates and deadtimes. L3 diagnostic data is simultaneously logged to the VERITAS database every second. Data associated

with each trigger are transmitted to the Harvester (Section 2.4.3) via a gigabit ethernet connection.

In order to form time coincidences between the L2 triggers, delays are applied by the frontend PDM to the incoming trigger signals from each telescope to bring them into time alignment. Each PDM has 32 independently programmable digital delay lines with a 2 ns step size and a 100 ns to 16 μs range. The PDM delays correct for both differences in propagation time between each telescope and the L3 trigger location (e.g. due to differences in the length of DAT fibres) and the expected delay in the arrival time of the Cherenkov shower wavefront due to varying geometrical orientation with respect to the VERITAS array. The delay applied to the L2 trigger from telescope i is

$$\Delta t_i = \mu_i + \mu_s + \delta_i,$$

where μ_i is a fixed propagation delay, μ_s is a positive constant that ensures the total delay is larger than the intrinsic PDM channel latency (96 ns), and δ_i is the time-varying geometrical shower delay given by

$$\delta_i = -\left(\mathbf{R}_i - \mathbf{R}_0\right) \cdot \mathbf{e}/c = -\left(x_i \sin\theta \sin\phi + y_i \sin\theta \cos\phi + z_i \cos\theta\right)/c,$$

where $\mathbf{e} = (\sin\theta\sin\phi, \sin\theta\cos\phi, \cos\theta)$ is the current array pointing, $\mathbf{R}_i - \mathbf{R}_0 = (x_i, y_i, z_i)$ is the position of telescope i with respect to array reference point $\mathbf{R}_0$, and c is the speed of light. After frontend delays have been applied, a residual timing spread with an RMS of ~ 10 ns remains (see Figure 2.7) due to both the curvature of the Cherenkov shower wavefront and timing jitter in the formation of the L2 trigger. For the outgoing trigger signals, a corresponding compensating delay is applied,

$$\Delta t_i = \mu_s - \delta_i. \tag{2.1}$$

This delay ensures a fixed roundtrip time between the generation of the L2 to

the arrival of the L3 trigger at the telescope DAQ. Delays for different telescopes are updated every five seconds using the current array pointing obtained from the positioner database records.

After frontend delays are applied, the delayed L2 triggers are passed to the SAT board that identifies groups of coincident triggers. The SAT board converts the arrival time of each L2 trigger into a digital timestamp via a time-to-digital converter (TDC) with a time resolution of 1.25 ns. The arrival timestamps are then searched for one or more telescope trigger patterns in the FPGA within a programmable coincidence window of 1.25–125 ns. The set of valid telescope trigger patterns is defined by a programmable trigger lookup table and can be used to include or exclude specific combinations of telescopes. The default L3 trigger configuration requires any combination of at least two telescopes (total telescope multiplicity of two). When a matching trigger pattern is found, an L3 trigger pulse is generated for all telescopes in the array. For telescopes that participated in the trigger decision, the timing edge of this pulse is determined by the arrival time of the corresponding L2 trigger ensuring a fixed propagation time through the L3 trigger system. In addition to the L3 trigger, a 48-bit event mask is transmitted asynchronously to each telescope over three serial data lines. Each event mask contains an 8-bit event type code and a 32-bit event number that uniquely identifies the event within the run. Information related to each event including L2 trigger TDC times, deadtime scalers, GPS timestamp, and the unique event number is saved to a FIFO buffer with a depth of 1024 events. Event records in the SAT FIFO are read out asynchronously by the L3 daemon at a rate of ~ 10 Hz and sent to the Harvester where they are later merged with the event data from the telescopes.

In addition to Cherenkov-shower-initiated triggers identified with an event

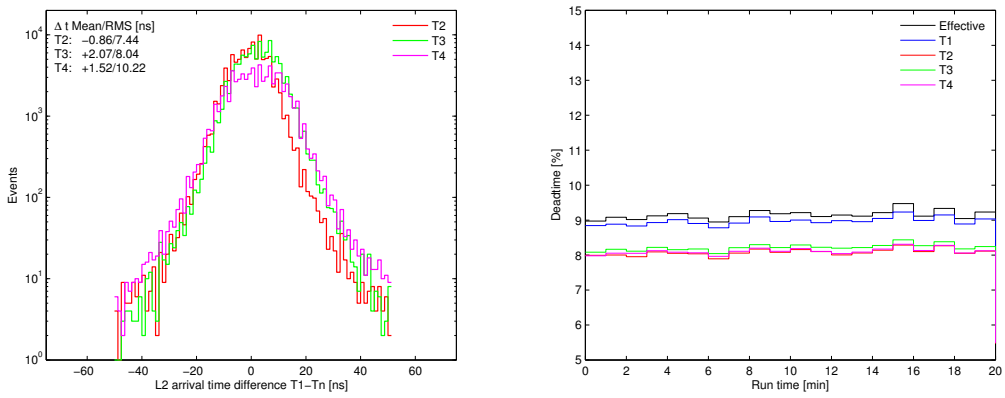

Figure 2.7 **Left:** Distribution of L2 arrival time differences relative to T1 for run 51758 after frontend PDM delays have been applied. **Right:** Deadtime as a function of run time for run 51758 as measured by the L3 deadtime scalers. The solid black line shows the total deadtime. Blue, red, green, and purple lines show the contribution to the total deadtime from each of the telescope DAQ systems.

type code, the L3 system also generates self-triggers at the rate of 1 Hz which are used to calibrate the channels in the absence of Cherenkov events. These events are used to measure the Flash Analog-to-Digital Converter (FADC) pedestal offset and the variance due to fluctuations in the NSB level in each channel. These triggers or pedestal events are generated with a special event type code.

After receiving an L3 trigger, each telescope DAQ stops and reads out a $\sim$ 50 ns portion of the FADC buffer. During readout, the DAQ inhibits the L3 trigger by raising a Busy level which is sent via the DATs. The SAT also self-vetos for 10 μs after an event decision, in order to allow for L3 signal propagation to the telescopes. The SAT board monitors the total deadtime and the deadtime contribution of each telescope with a 10 MHz reference clock and a set of onboard 32-bit scalers (see Figure 2.7). The array deadtime is primarily determined by

the telescope DAQ readout time of ~ 400 μs. For small deadtimes, the deadtime scales linearly with the L3 rate and is approximately 10% for an L3 trigger rate of ~ 220 Hz. A detailed description of the L3 trigger is presented in Weinstein (2008).

2.4 Data Acquisition System

The VERITAS DAQ system is responsible for digitizing the analog signals from the camera pixels and saving these data to disk in the VERITAS Bank Format (VBF). A schematic of the VERITAS DAQ system is shown in Figure 2.8. The core of the DAQ system are the Flash Analog-to-Digital Converter (FADC) boards that perform the digitization of the analog signals (Section 2.4.1). The acquisition of an event is initiated by the L3 trigger distributed to each telescope via the DATs. When the L3 trigger is received, the telescope data acquisition software reads out a portion of the FADC buffer and assembles the data into a telescope event. Data from all array subsystems are finally assembled by the Harvester (Section 2.4.3) and saved to disk. The VERITAS DAQ system is described in Hays (2008).

2.4.1 FADC Boards

The FADC system is the frontend of the VERITAS DAQ chain and consists of a set of 50 10-channel FADC boards distributed across four 9U VME crates (Rebillot et al., 2003). Each FADC channel digitizes the analog signal from a single camera pixel. The input signal to each FADC channel is fanned out to the CFD (amplified by 6) and the high gain FADC channel (amplified by 7.25). Each FADC channel has an 8-bit dynamic range (0–255 digital counts (dcs) with

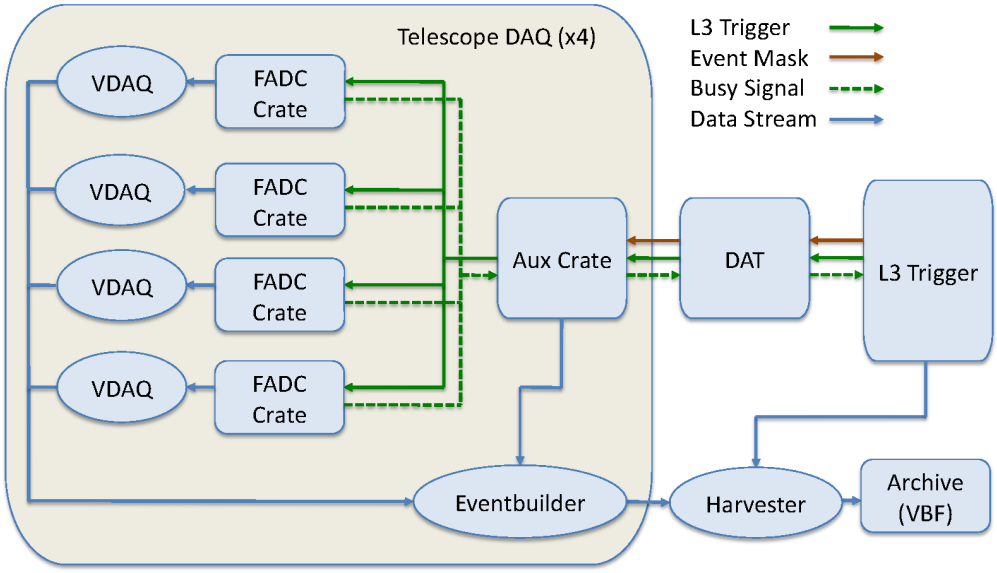

Figure 2.8 Schematic of the VERITAS data acquisition system.

1 dc = 7.81 mV). An automatic HiLo gain-switching feature is implemented to increase the effective dynamic range to 1500 digital counts. The HiLo gain switch activates when a pulse saturates the high gain FADC channel and operates by passing a delayed copy of the original pulse amplified by 1.21 to the FADC circuit. Prior to digitization, a voltage level (pedestal) is introduced with an amplitude of ∼20 dc to allow measurement of both positive and negative fluctuations in the analog signal amplitude. Signals are digitized at 500 Megasamples per second with a circular buffer depth of 32 μs. When a stop signal (L3 trigger) is received, digitization is halted and a portion of the FADC memory buffer is copied to on-board buffer RAM for readout by the VME DAQ system.

2.4.2 Telescope DAQ

The VME DAQ system is responsible for reading out the FADC memory, assembling the data into telescope events, and sending this data to the Harvester over gigabit ethernet. The hardware consists of five VME crates: four FADC crates containing 12 or 13 FADC boards and a clock trigger board (CTB) and one auxiliary crate containing a GPS clock and the master CTB. Each crate also houses a VME CPU controller that runs an instance of the VME Data Acquisition (VDAQ) software. When an L3 trigger is generated, it is first passed to the master CTB from which it is fanned out to the CTBs of the individual crates. Readout of the FADCs is initiated when an L3 trigger is received. After an L3 trigger is received, VDAQ reads out a portion of the FADC circular buffer memory which is determined by a programmable FADC lookback time and window size. In addition to the digitized FADC trace values, the CFD trigger and HiLo gain switch bits are also registered. During readout, a Busy level is transmitted to the DAQ auxiliary crate where it is combined with the Busy levels of the other FADC crates and transmitted to the L3 trigger. This Busy level ensures that the L3 trigger remains inhibited during FADC readout which lasts $\sim$ 400 μs. Each VDAQ process collects the partial event data until its buffer size grows to $\sim$ 2000 events. The event buffer is then transferred to the Event Builder over the Scalable Coherent Interface (SCI) link. The Event Builder is responsible for assembling these data into telescope events and sending them to the Harvester over a gigabit ethernet connection.

2.4.3 Harvester

The array-level data acquisition software, Harvester, runs on a dedicated central server and is responsible for collecting event data from the individual telescope

DAQ systems and the L3 trigger system. Event data are combined into array events by matching the unique event numbers generated by the L3 trigger. Data is saved to a RAID archive in the VERITAS Bank Format (VBF). The VBF format incorporates an FADC trace compression algorithm that reduces the output file sizes by a factor of $\sim$2. A typical VBF file for a 20 minute run taken with an L3 trigger rate of 200–250 Hz is 4–6 GB in size. The raw data in the form of VBF files is analyzed by the VERITAS analysis software (Chapter 3).

CHAPTER 3

Data Analysis

The analysis of VERITAS data proceeds through several stages beginning with the output of the data acquisition and ending with a measurement of the intrinsic properties of a gamma-ray source. The results presented in this thesis were obtained with the *ChiLA* analysis and simulation package developed at UCLA. The primary contributors to this package were Stephen Fegan, Vladimir Vassiliev, and Matthew Wood. Further discussion on many of the topics presented in this chapter can be found in referenced collaboration memos.

The analysis progression is shown as a flow diagram in Figure 3.1. The input to the analysis chain are data files in the VERITAS Bank Format (VBF) produced by the online data acquisition software (Section 2.4). The core analysis routines are divided into three stages each of which creates an intermediate data product that is used as input to the next stage. Intermediate products are saved in the HDF5 format[1], an open-source binary file format designed for large data sets.

A brief outline of the analysis procedure is following. The first two stages (*stage1/stage2*) perform the reconstruction of individual events. The analysis begins at the pixel level with the calculation of pedestal (Section 3.1.1) and gain (Section 3.1.2) calibrations and the determination of the pixel signal from the integral of the FADC trace (Section 3.1.3). Low signal-to-noise pixels in each camera image are removed through the *image cleaning* procedure (Section 3.1.4)

[1] http://www.hdfgroup.org/HDF5/

with the remaining pixels forming the telescope image. The cleaned images from each telescope are parameterized and used to reconstruct the direction, shower core location, and energy of the gamma-ray primary (Section 3.2). The final analysis stage (*stage3*) performs source and background modeling on the distributions of event parameters calculated by *stage2*. A subset of the parameterized event sample is first selected by applying *cuts* to the data (Section 3.3) to reject a large fraction of the hadron-initiated atmospheric cascades that constitute the majority of events. A model for the residual background after cuts is then constructed and used to test for the presence of a gamma-ray excess in the field (Section 3.5). Once a source is identified its intrinsic flux and spectral energy distribution are modeled using gamma-ray Monte Carlo simulations and spectral reconstruction techniques (Section 3.6).

3.1 Calibration and Image Cleaning

The first step in the analysis chain is to assign to each FADC *trace* an integral signal proportional to the number of photons it collected. The trace is a record of the PMT signal amplitude measured at 2 ns time intervals (*samples*). A model for the PMT signal time profile given a distribution of Cherenkov photons $\mu(t)$ is

$$q(t) = G\epsilon \int_{-\infty}^{\infty} f(t-t')\mu(t')dt' + b(t) + q_{\rm ped}, \tag{3.1}$$

where G is the pixel gain in digital counts per photoelectron (DC/PE), ϵ is the pixel photon collection efficiency, $f(t)$ is the single photon response function (whose area is normalized to one), $b(t)$ is an AC component due to the contribution from night sky background photons and electronics noise, and $q_{\rm ped}$ is the pedestal amplitude. The integral signal is found by integrating $q(t)$ over a time window (t_0, t_1). If $t_1 - t_0$ is significantly larger than the width of the single PE

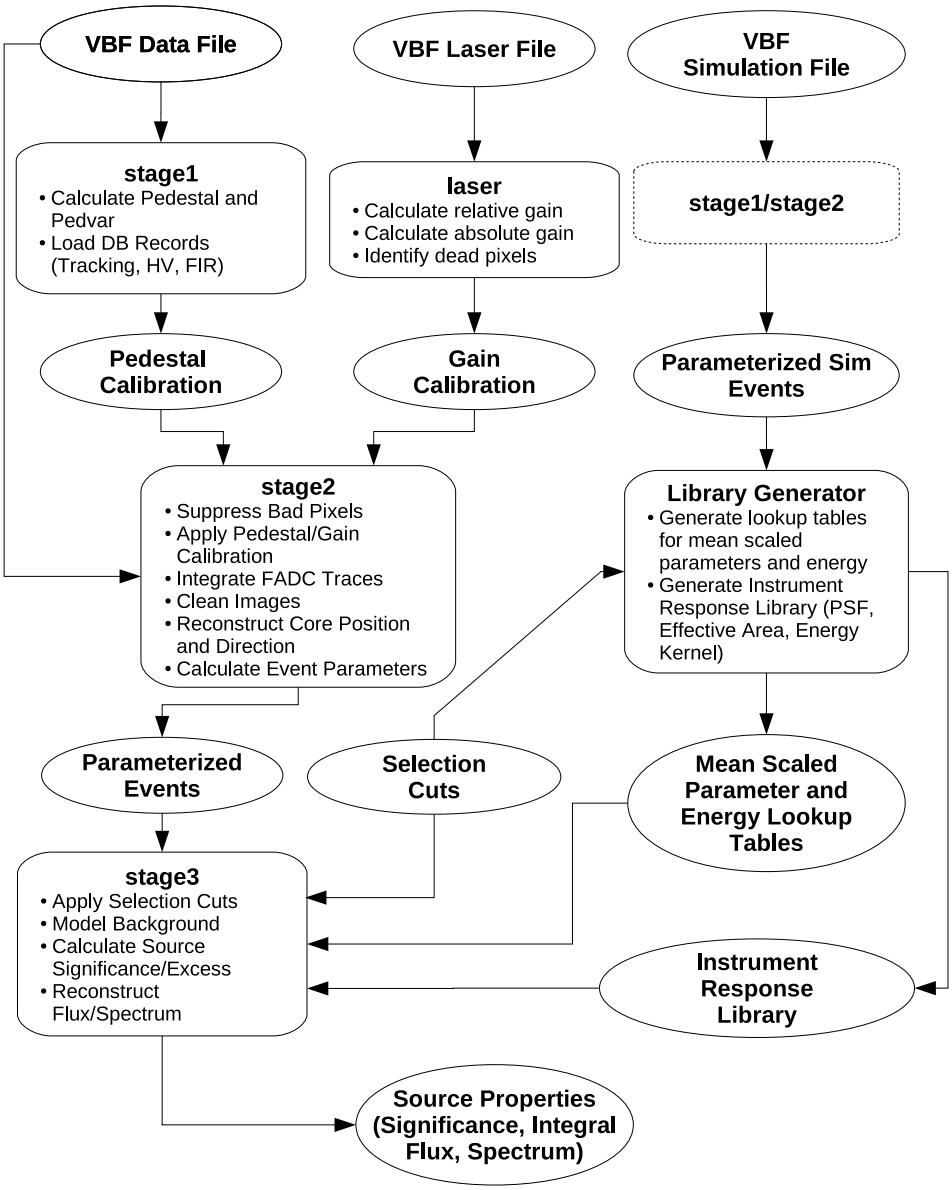

Figure 3.1 Flow diagram for ChiLA analysis package. Data products are shown as ellipses and data processing routines as rounded rectangles.

response function, the integral of Equation 3.1 for pixel i is

$$Q_i = G_i \epsilon_i \frac{s_i}{\langle G\epsilon \rangle} + Q_{\mathrm{ped},i}, \tag{3.2}$$

where Q_i is the value of the FADC trace integral in DC, $Q_{\mathrm{ped},i} = q_{\mathrm{ped},i}\,(t_1 - t_0)$ is the pedestal integral, $s_i \simeq \langle G\epsilon \rangle \int_{t_0}^{t_1} \mu_i(t')dt'$ is the camera-normalized pixel signal, and $\langle G\epsilon \rangle$ is an average of the photon response (DC per photon) over all pixels in the camera. It is assumed that $\langle b(t) \rangle = 0$ since the output of the PMT is AC coupled at the preamplifier. The *relative gain* correction for the pixel photon response is denoted as $g_i = G_i\epsilon_i / \langle G\epsilon \rangle$. Once the trace integral is known, the determination of s_i relies upon the pedestal and gain calibration.

3.1.1 Pedestal Calibration

The pedestal for each FADC channel is determined from the analysis of artificially triggered *pedestal* events that are generated with a constant 1 Hz rate by the L3 trigger (Section 2.3.3). Since the typical rate of the Cherenkov events is 150–250 Hz and the duration of a single flash is 10 ns, the probability of contamination of the pedestal events with Cherenkov photons is $\lesssim 10^{-5}$. The pedestal amplitude q_{ped} for each FADC channel is determined by averaging the trace over the full readout window for all pedestal events,

$$q_{\mathrm{ped},i} = \frac{1}{N_{\mathrm{ped}} \Delta t} \sum_{j}^{N_{\mathrm{ped}}} Q_{ij}, \tag{3.3}$$

where Δt is the width of the readout window and N_{ped} is the number of pedestal events. A typical value for $q_{\mathrm{ped},i}$ in VERITAS is in the range 15–20 DC.

The RMS of the pedestal trace integral distribution or *pedvar* is given by

$$\sigma_{\mathrm{ped},i}(\Delta t) = \left[\frac{1}{N} \sum_{j=1}^{N} \left(Q_{ij}(\Delta t) - q_{\mathrm{ped},i} \Delta t \right)^2 \right]^{1/2}, \tag{3.4}$$

where $Q_{ij}(\Delta t)$ is the value of the pedestal trace integral evaluated with an integration window Δt and N is the number of independent measurements of $Q_{ij}(\Delta t)$ obtained from N_{ped} pedestal events. The pedvar is set by the noise term $b(t)$ in Equation 3.1 and is the sum of contributions from night sky background (NSB) photons, the stochastic response of the PMT, and electronics noise. Under normal operating conditions the contribution from NSB photons dominates since night sky photons are detected by a PMT on average every ~ 10 ns. Unlike the pedestal amplitude, the pedvar can vary significantly between observations due to variations in the intrinsic brightness of different fields (e.g. galactic vs. extragalactic). The rotation of the FoV during an observation run (typically 20 minutes) also introduces a time-dependence to the pedvar which is accounted for by evaluating the pedvar in three minute intervals. For the VERITAS operation regime with a typical integration window of 10–20 ns, the pedvar depends nontrivially on the size of the integration window and is therefore explicitly calculated for all possible values of this parameter. If the integration window is smaller than the length of the FADC readout trace, multiple measurements of the pedvar are made from a single pedestal event by repeatedly shifting the pedestal integration window by the window size plus an additional shift factor of 3 samples. This choice of shift factor (6 ns) ensures that the multiple measurements are uncorrelated and also minimizes the effect the 125 MHz clock noise introduced by the FADC electronics.

3.1.2 Gain Calibration

The pixel gain calibration is measured by recording the short pulse of photons produced by a UV laser that uniformly illuminates the camera focal plane. The laser pulse is intended to mimic the time profile of a Cherenkov shower. These data form a special calibration laser run which is taken nightly and contains

$\sim$ 3000 laser flashes. For each pixel, two calibration constants are calculated: a relative gain correction, g_i, and an absolute gain, G_i. The relative gain calibration corrects for differences in light throughput (product of optical efficiency and absolute gain) across the camera, and the absolute gain calibration converts the gain equalized signal in DCs into a number in PEs that is independent of the PMT gain during a particular observation epoch.

The relative gain correction of a pixel is calculated as

$$g_i = \frac{1}{N} \sum_{j=1}^{N} \frac{s_{ij}}{\langle s_j \rangle}, \tag{3.5}$$

where N is the number of laser flashes, $s_{ij} = Q_{ij} - Q_{ped,i}$ is the laser signal recorded for pixel i and flash j, and $\langle s_j \rangle$ is the camera-averaged laser signal for flash j.

The absolute gain of a pixel is the proportionality constant between the integrated signal measured in digital counts (DCs) and the number of photoelectrons (PEs) captured at the first dynode of the PMT. Its value depends on the PMT gain, the current to voltage conversion factor in the preamplifier, the attenuation in the signal cables, the voltage gain factor at the FADC, and the voltage to DC conversion factor. The photostatistics method (Fegan & Wood, 2008) is a technique for determining the absolute gain, G_i, from the statistics of laser flashes. For a fixed laser flash intensity, n_i photons, the laser signal, s_{ij}, recorded for flash j should closely follow a Poisson distribution with a mean given by,

$$\langle s_i \rangle = n_i G_i \epsilon_i, \tag{3.6}$$

and variance,

$$\sigma_{s_i}^2 = n_i \epsilon_i \left(G_i^2 + \sigma_{q,i}^2 \right) + \sigma_{\mathrm{ped},i}^2, \tag{3.7}$$

where $\sigma_{q,i}^2$ is the variance of the single PE amplitude distribution (which is a function of the PMT gain) and $\sigma_{\mathrm{ped},i}^2$ is the pedestal variance. The absolute gain

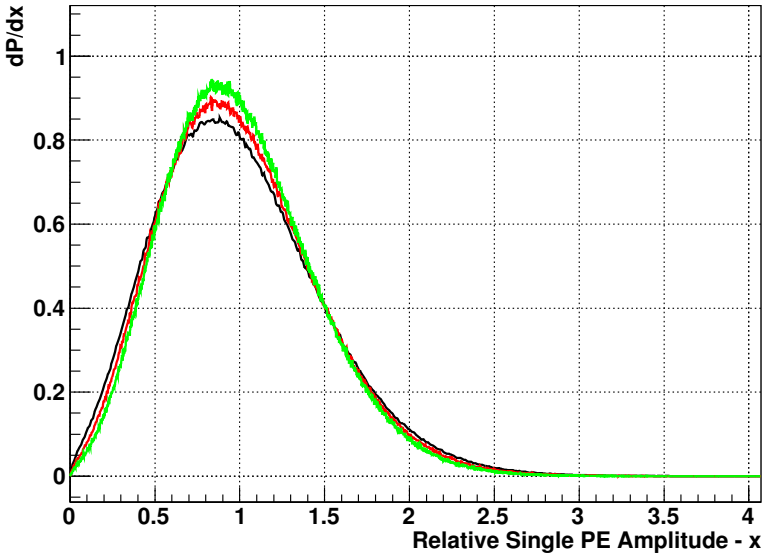

Figure 3.2 **Left:** Simulated p.d.f. for the relative single PE amplitude ($x = n_e/\langle n_e \rangle$) assuming a total gain of 10^5 (black line), 2×10^5 (red line), and 4×10^5 (green line). The RMS (σ_x) of these distributions are 0.484, 0.460, and 0.438.

is thus inferred from the relationship between the mean and variance as,

$$G_i = \frac{\sigma^2_{s_i} - \sigma^2_{\mathrm{ped},i}}{\langle s_i \rangle \, (1 + \alpha^2)}, \tag{3.8}$$

where $\alpha_i = \sigma_{q,i}/G_i$. To correct for intrinsic variations in flash intensity, the flash-equalized laser signal, $\tilde{s}_{ij} = \langle s \rangle \, s_{ij} / \langle s_j \rangle$, is used where $\langle s \rangle$ is the mean laser intensity averaged over all flashes.

The variance $\sigma^2_{q,i}$ of the single PE amplitude is determined by the statistics of the electron multiplication process in the PMT dynode chain. To estimate $\sigma^2_{q,i}$, a simple model of the VERITAS PMT was developed (Fegan & Wood, 2008) in which the p.d.f. for secondary emission at each dynode was represented by a Poisson distribution. Figure 3.2 shows the results of a Monte Carlo simulation

generated with this model. This model is applicable for the nominal VERITAS PMT (Photonis XP2970/02) with ten dynode stages, a gain of 2×10^5, and a gain-voltage relation $g \propto V^{7.4}$. A value $\alpha = 0.46$ was found to be compatible with the single PE PMT simulation and independent of PMT gain to first order. This value was therefore used in the estimation of absolute gains G_i. It must be noted, however, that a significant variation in α has been observed in the sample of VERITAS PMTs (Hanna et al., 2010).

3.1.3 Trace Integration

The FADC trace integral, Q_i, is proportional to the number of Cherenkov photons collected by a pixel and is a summation over the FADC trace amplitudes,

$$Q_i = \sum_{j=j_{\text{start}}}^{j_{\text{end}}} q_{ij}, \tag{3.9}$$

where q_{ij} is the amplitude of sample j and j_{start} and j_{end} are the indices of the first and last samples of the integration window respectively. To minimize the contribution of noise, the trace integration is carried out over a $\sim$ 10–20 ns integration window encompassing the majority of the charge from the Cherenkov pulse. The size of the integration window is determined by the time profile of the typical Cherenkov pulse which is characterized by a rise time of 3–4 ns and tail with a fall time of $\sim$ 10 ns. The pulse arrival time has a dispersion of $\sim$ 4 ns which can be mostly attributed to the intrinsic spread of the Cherenkov photon arrival times, the non-isochronicity of the VERITAS optical system, and the jitter in the formation of the L2 trigger.

The primary trace integration algorithm used in *stage2* defines a dynamic integration window for each trace on the basis of the pulse arrival time and a preliminary measurement of the pulse amplitude. Using a dynamic window

maximizes the signal-to-noise for varying pulse sizes and reduces systematic errors due to timing jitter. The pulse arrival time, t_0, is found by a linear interpolation between the two samples bracketing the amplitude that is 50% of the maximum trace amplitude relative to the pedestal. The start and end times of the trace integration window are pulse height dependent and are defined as

$$\begin{aligned} t_{\rm start}(s_{tot}) &= t_0 - \Delta t_{\rm start} - \max\left(\alpha_{\rm start}\log_{10}\left(\frac{s_{tot}}{100\ {\rm DC}}\right), 0\right) \\ t_{\rm end}(s_{tot}) &= t_{\rm start} + \Delta t_{\rm min} + \max\left(\alpha_{\rm width}\log_{10}\left(\frac{s_{tot}}{100\ {\rm DC}}\right), 0\right), \end{aligned} \tag{3.10}$$

where $\Delta t_{\rm start}$ is the starting point of the integration window relative to t_0, $\Delta t_{\rm min}$ is the minimum size of the integration window, $\alpha_{\rm start}$ and $\alpha_{\rm width}$ define the rate of change of the integration start time and window size per decade of pulse amplitude, and s_{tot} is the pedestal-subtracted trace integral for an integration window encompassing the entire trace. The default values adopted in *stage2* for the four parameters, $\Delta t_{\rm start}$, $\Delta t_{\rm min}$, $\alpha_{\rm width}$, and $\alpha_{\rm start}$, are given in Table 3.1.

3.1.4 Image Cleaning

The image cleaning procedure removes low signal-to-noise pixels from each telescope event. For each pixel the signal-to-noise ratio is given by $\sigma_i = (Q_i - Q_{{\rm ped},i})/\sigma_{{\rm ped},i}$ where $\sigma_{{\rm ped},i}$ is the pedvar corresponding to the integration window size that was used to calculate Q_i. The ChiLA package uses the *regional* cleaning algorithm. Pixels are included in the image if they belong to a contiguous group of at least N (*region size*) pixels that all have σ_i greater than *region threshold*. In addition any pixel is automatically included in the image if it is above the *isolated threshold*. Based on an optimization study with Crab data taken in 2007, the following parameters were adopted 3 (region size), 4.5 (region threshold), and 10 (isolated threshold). Images that do not survive cleaning are excluded from further analysis.

Table 3.1. Summary of standard *ChiLA* analysis settings.

Parameter	Value
Integration Parameters	
Δt_{min}	5 samples
Δt_{start}	0.5 samples
α_{width}	3 samples/decade
α_{start}	0.5 samples/decade
Cleaning Parameters	
Region Size	3
Region Threshold	4.5σ
Isolated Threshold	10σ
Image Quality Cuts	
Minimum Image Size	250 DC
Minimum Image Pixels	3
Maximum Image Distance	1.5 degrees
Minimum Telescopes	2
Lookup Table Options	
Scaled Parameter Weight	1
Telescope Energy Weight	1
Energy Reconstruction Quality Cuts	
Maximum Impact Distance	250 m
Maximum Image Distance	1.3 degrees

3.2 Event Parameterization and Reconstruction

The cleaned telescope images are used to calculate a reduced set of event parameters that include the focal plane image moments (Section 3.2.1), the 3D trajectory of the shower primary (Section 3.2.2), the shower energy (Section 3.2.4), and discrimination parameters for cosmic-ray background rejection (Section 3.2.3).

3.2.1 Telescope Image Parameterization

The basic telescope image parameters are given by the first three moments of the light distribution in the focal plane,

$$\begin{aligned} S_i &= \sum_j s_{ij}, \\ V_i^\alpha &= \frac{1}{S_i} \sum_j s_{ij} p_{ij}^\alpha, \\ T_i^{\alpha\beta} &= \frac{1}{S_i} \sum_j s_{ij} p_{ij}^\alpha p_{ij}^\beta, \end{aligned} \tag{3.11}$$

where i is the telescope index, s_{ij} and p_{ij}^α are the signal and focal plane coordinate, $\alpha = x, y$, of pixel j (Hillas, 1985). The zero moment, S_i, and first moments, $V_i^{x,y}$, are referred to as the image *size* and *centroid* coordinates, respectively. The norm of the vector V_i^α equal to the separation of the centroid from the center of the field of view is the image *distance*. The tensor $T^{\alpha\beta} - V^\alpha V^\beta$ defines the second central moments with eigenvectors corresponding to the principle axes of the image $(\boldsymbol{\varrho}, \boldsymbol{\kappa})$ and eigenvalues (l^2, w^2) referred to as the *length* and *width* $(l > w)$.

3.2.2 Event Geometry Reconstruction

The 3D trajectory of the shower primary is characterized by its arrival direction $\boldsymbol{e}$ and core location $\boldsymbol{R}$. The ChiLA package implements three event reconstruction methods (Vassiliev & Fegan, 2005) that operate on the principle of finding a shower trajectory ($\boldsymbol{e}$,$\boldsymbol{R}$) that minimizes a chi-squared like functional. In *Method 1*, images in the different telescopes are treated independently and the minimization functional is the sum squared distances to the Cherenkov photons collected by the telescopes. *Method 2* optimizes the trajectory parameters based on a simultaneous fit to all images of $\boldsymbol{e}$ and $\boldsymbol{R}$ vectors projected onto the focal plane. *Method 3* performs an optimization in three dimensional space and minimizes the square of the shortest distances of back-projected trajectories of individual photons in all telescopes to the trajectory of the primary. The inclusion of dim and truncated images was found to diminish the performance of these reconstruction algorithms, and therefore a set of quality criteria are used to select a subset of images to be used in reconstruction. The default values of the quality criteria used in *stage2* are given in Table 3.1.

The simplest reconstruction method, *Method 1*, operates on the two dimensional projection of the shower in the focal plane of each telescope. The image axes, ($\boldsymbol{\kappa}$, $\boldsymbol{\varrho}$), are derived independently for each telescope by finding the eigenvectors of the second central momenta. The vector describing the closest approach of the image axis to the projected source position, $\boldsymbol{\xi}$, is given by

$$\boldsymbol{\Delta}_{e,i} = ((\boldsymbol{\xi} - \boldsymbol{V}_i) \cdot \boldsymbol{\varrho_i})\, \boldsymbol{\varrho_i} \tag{3.12}$$

The vector components ξ^α are found by minimizing

$$\chi^2_e = \sum_i S_i \frac{l_i^2 - w_i^2}{w_i^2} \left(\boldsymbol{\Delta}_{e,i} \cdot \boldsymbol{\Delta}_{e,i}\right). \tag{3.13}$$

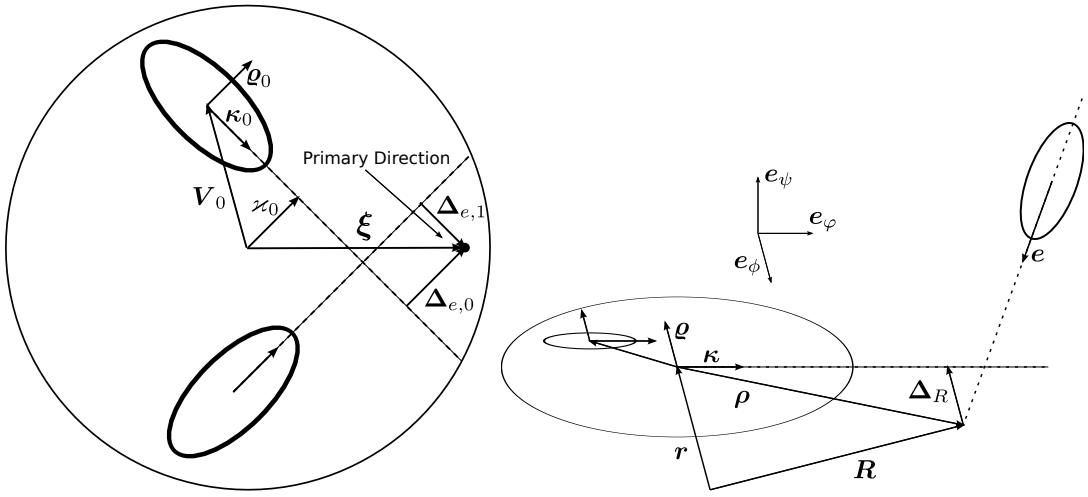

Figure 3.3 **Left:** Illustration of parameters used for reconstruction of the shower direction. **Right:** Illustration of parameters used for reconstruction of the shower core position.

The contribution of each telescope is weighted by both the image size S_i and ellipticity $(l_i^2 - w_i^2)/w_i^2$. The latter factor decreases the effect of the images with nearly degenerate eigenvectors onto the reconstructed position of the source $\boldsymbol{\xi}$. For the reconstruction of the core position, one can likewise define a distance of closest approach between the image axis and the core position relative to the telescope,

$$\boldsymbol{\Delta}_{R,i} = ((\boldsymbol{R} - \boldsymbol{r}_i) \cdot \boldsymbol{\varrho_i})\, \boldsymbol{\varrho_i} \tag{3.14}$$

where $\boldsymbol{r}_i$ is the position of telescope i in the focal plane. The core position, R^α, is then found by minimizing,

$$\chi^2_R = \sum_i S_i \frac{l_i^2 - w_i^2}{w_i^2} \left(\boldsymbol{\Delta}_{R,i} \cdot \boldsymbol{\Delta}_{R,i}.\right) \tag{3.15}$$

Method 1 is most frequently used in this work; the detailed descriptions of *Method 2* and *Method 3* is outlined in (Vassiliev & Fegan, 2005).

3.2.3 Event Identification

A significant challenge for the analysis of TeV gamma-ray data is the overwhelming cosmic-ray background. To isolate gamma-ray signals, one needs to devise a discrimination method between cosmic-ray and gamma-ray initiated Cherenkov showers. A widely used method (Krawczynski et al., 2006) for identifying gamma-ray-like events is based on the introduction of the discrimination parameters,

$$\tilde{p_i} = \frac{p_i - p_{\rm sim}(\rho_i, S_i)}{\sigma_{\rm sim}(\rho_i, S_i)}, \tag{3.16}$$

where $p_{\rm sim}(\rho_i, S_i)$ and $\sigma_{\rm sim}(\rho_i, S_i)$ are the expectation and standard deviation of the parameter derived from simulations as a function of image size, S, and telescope impact distance, $\rho_i = |\boldsymbol{R} - \boldsymbol{r}_i|$. The implementation adopted for ChiLA uses the median and 68% containment interval to generate the tables for expectation value and standard deviation for the focal plane parameters *width*, *length*, and *disp*. The *disp* parameter is defined as the distance between the image centroid and the projected source position ($|\boldsymbol{\xi} - \mathbf{V}_i|$). The mean scaled parameter is constructed from a weighted average of the $\tilde{p_i}$ over all telescopes in the event,

$$\langle \tilde{p} \rangle = \left(\sum_i \frac{1}{\sigma_{\rm sim}(\rho_i, S_i)^\delta} \right)^{-1} \sum_i \frac{\tilde{p_i}}{\sigma_{\rm sim}(\rho_i, S_i)^\delta}. \tag{3.17}$$

In this formula, the definition of mean scaled parameter is generalized by introducing a variable weighting factor controlled by the power index δ. Increasing δ effectively suppresses the contribution of telescopes with significant fluctuations in the parameter value.

3.2.4 Event Energy Estimation

The reconstruction of the primary particle energy of each event is an essential input for spectral analysis of gamma-ray sources. The intrinsic brightness of a

Cherenkov shower scales with the number of secondary particles produced in the electromagnetic cascade and thus can be used as a proxy for the energy of the shower primary. Due to the highly nonuniform Cherenkov emission pattern on the ground, the apparent shower brightness in each telescope has a complex dependence on the impact distance and event energy. For radii larger than $\sim$125 m the image size decreases rapidly, first as a power-law and then exponentially with impact distance. The energy estimator is the function derived from simulations that is used to assign to each event a most probable energy based on the event geometry and telescope image sizes.

The methodology adopted for the gamma-ray energy estimator is similar to that used for event identification discrimination parameter described in Section 3.2.3. Using Monte Carlo simulations, a lookup table for gamma-ray energy is constructed for each telescope as a function of telescope image size, S, and one or more additional reconstructed parameters, $\mathbf{p}$. Tables with $\mathbf{p} = \{\rho\}$ and $\mathbf{p} = \{\rho, disp\}$ were explored. Two methods for creating the energy lookup table have been studied: *EnergyTable* and *InverseSizeTable*. For the *EnergyTable* method, the distribution of simulated energies is fixed to follow a power-law distribution with index Γ (e.g. a power-law with $\Gamma = 2.5$). This is achieved by assigning a weight $w(E)$ to each event. The *EnergyTable* method accumulates the distribution of simulated event energies in each bin of an N-dimensional histogram with axes $\{S, \mathbf{p}\}$. In each bin the energy estimator, $E(S, \mathbf{p})$, is set to the median energy in that bin while the dispersion, $\sigma_E(S, \mathbf{p})$, is calculated from the 68% containment interval. The resulting lookup tables, $E(S, \mathbf{p})$ and $\sigma_E(S, \mathbf{p})$, depend weakly on the choice of the input energy distribution.

The *InverseSizeTable* method performs a direct inversion of the function relating median size and true event energy and thus is independent of the energy

distribution of the Monte Carlo training sample. Distributions of image size are accumulated in each cell of an N-dimensional histogram with axes $\{E, \mathbf{p}\}$, where E is the true gamma-ray energy. Lookup tables for median size, $S(E, \mathbf{p})$, and its dispersion, $\sigma_S(E, \mathbf{p})$, derived from the 68% containment interval are then generated from the size distribution in each bin. For a given $\mathbf{p}$ the monotonically increasing function of energy $S(E; \mathbf{p})$ is fitted with the polynomial of minimal order which satisfies $\chi^2/\mathrm{ndf} \simeq 1$ with the constraint $dS(E; \mathbf{p})/dE > 0$. The polynomial is then numerically inverted to produce a corresponding function in energy, $E(S; \mathbf{p})$. Figure 3.4 illustrates distributions of size versus energy and the associated polynomial fits calculated for the size table with $\mathbf{p} = \{\rho, disp\}$. The dispersion of the energy estimator is calculated as $\sigma_E(S, \mathbf{p}) = \sigma_S(E, \mathbf{p})dE/dS$ where energy is evaluate at $E(S, \mathbf{p})$. Lookup tables for the energy estimator and dispersion calculated with the *InverseSizeTable* method and $\mathbf{p} = \{\rho\}$ are shown in Figure 3.5.

Using the energy lookup tables, an energy estimator is calculated for each telescope image passing the energy reconstruction quality cuts summarized in Table 3.1. The event energy estimate is a weighted average of the energy estimates of each telescope,

$$\langle E \rangle = \left(\sum_i \frac{1}{\sigma_{\mathrm{E}}(S_i, \mathbf{p}_i)^\alpha} \right)^{-1} \sum_i \frac{E(S_i, \mathbf{p}_i)}{\sigma_{\mathrm{E}}(S_i, \mathbf{p}_i)^\alpha}, \tag{3.18}$$

where α is a parameter controlling the weighting factor of each telescope due to uncertainty in estimation of energy.

The optimal energy estimator must have good energy resolution ($\Delta E/E$) and ideally should also have minimal bias across the range of energies where VERITAS is most sensitive (100 GeV $\lesssim E \lesssim$ 10 TeV). The performance of different estimators is compared using the bias and dispersion in logarithmic

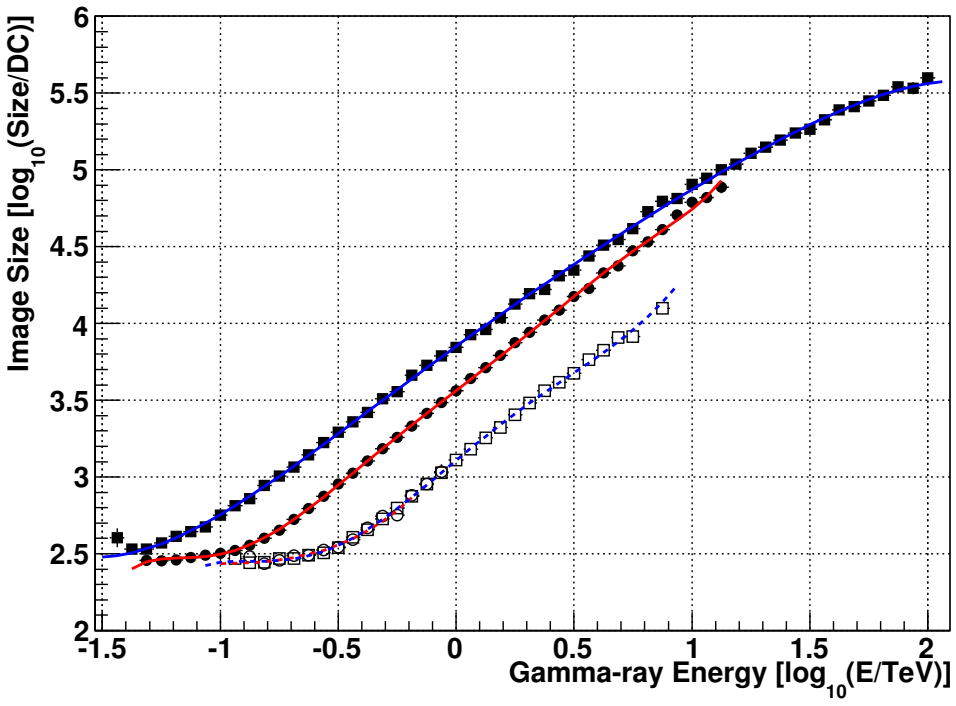

Figure 3.4 Median image size, $S(E, \mathbf{p})$, versus gamma-ray energy, E, and the associated polynomial fits from the size table with $\mathbf{p} = \{\rho, disp\}$ at four discrete points in $\{\rho, disp\}$: $\{80\text{ m}, 0.6°\}$ (solid circles, red line), $\{80\text{ m}, 1.0°\}$ (solid squares, blue line), $\{200\text{ m}, 0.8°\}$ (open circles, dashed red line), and $\{200\text{ m}, 1.2°\}$ (open squares, dashed blue line). The distributions shown were generated from a simulated gamma-ray sample with $Zn = 20°$, $Az = 0°$, and $R_{\text{NSB}} = 0.07\text{ PE ns}^{-1}$.

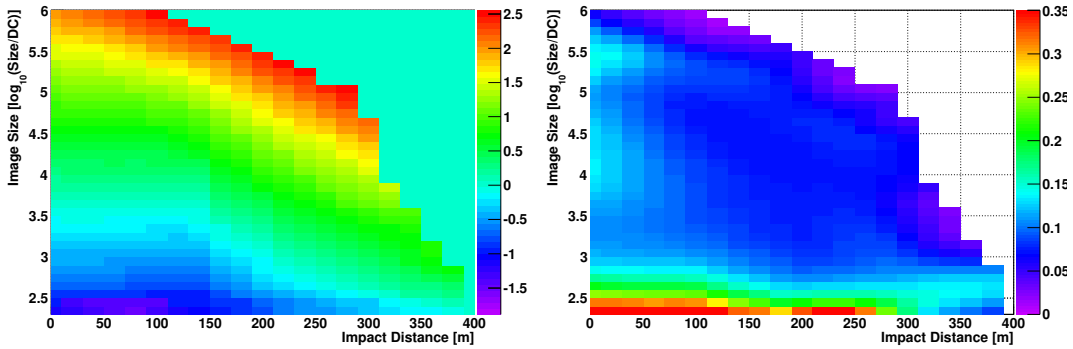

Figure 3.5 Energy estimator (**left**) and energy estimator dispersion (**right**) as a function of image size and telescope impact distance obtained with the *InverseSizeTable* method and $\mathbf{p} = \{\rho\}$.

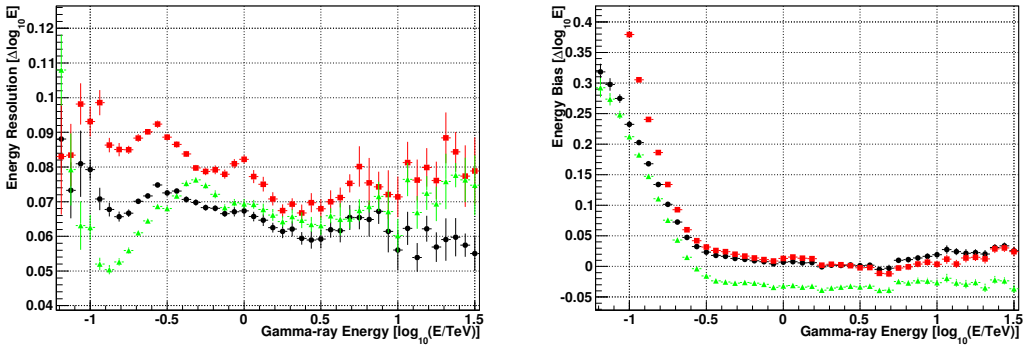

Figure 3.6 **Left:** Energy estimator resolution ($\Delta \log_{10} E$) as a function of true gamma-ray energy for tables generated with the *InverseSizeTable* method and $\mathbf{p} = \{\rho, disp\}$ (black circles), *InverseSizeTable* method and $\mathbf{p} = \{\rho\}$ (red squares), and the *EnergyTable* method and $\mathbf{p} = \{\rho, disp\}$ (green upward triangles). All three estimators were calculated with an energy estimator weighting index, $\alpha = 1$. **Right:** Energy estimator bias ($\delta \log_{10} E$) as a function of true gamma-ray energy for the three estimators shown in the left panel.

energy space defined as

$$\begin{aligned} \delta \log_{10} E &= \left\langle \log_{10} \tilde{E} \right\rangle - \log_{10} E, \\ \Delta \log_{10} E &= \sqrt{\left\langle \left(\log_{10} \tilde{E} \right)^2 \right\rangle - \left(\log_{10} E + \delta \log_{10} E \right)^2}, \end{aligned} \tag{3.19}$$

where $\tilde{E}$ denotes the estimated energy. Figure 3.6 shows a comparison of the energy resolution and bias of three different energy estimators applied to a sample of simulated gamma rays analyzed with the *Standard* cuts analysis. The addition of *disp* as an independent dimension of the energy estimator improves the energy resolution in the low- to mid-energy range by $\sim 25\%$ and significantly reduces the estimator bias for low energy events. It was found that the effect of the *disp* parameter on the energy estimator is only significant when one or more telescopes detect Cherenkov radiation inside the light pool ($\rho \lesssim 125$ m). Most of the low-energy events ($E \lesssim 150$ GeV) are detected in this regime. The *EnergyTable* and *InverseSizeTable* methods have comparable energy resolution above ~ 300 GeV but the *InverseSizeTable* methods results in a consistently smaller bias at these energies. The choice of weighting index $\alpha = 1$ was found to marginally improve the energy resolution as compared to an unweighted average of the energy estimates ($\alpha = 0$).

3.3 Gamma-ray Selection Optimization

Hadron-initiated atmospheric cascades constitute the vast majority of the events recorded by VERITAS. To reduce the background contamination in the parameterized event sample produced by *stage2*, a set of *cuts* is applied at *stage3*. The optimized cut values are chosen to maximize the signal-to-noise ratio for a weak source (detected in the background-dominated regime) with a given spectrum.

Cut optimization is performed by finding an optimal cut volume in the pa-

Table 3.2 Optimized analysis cuts. For *Size*2 the table shows the lower bound while for the other parameters the upper bound is given.

	*Size*2 [DC]	MSW	MSL	MSD	θ^2 [deg^2]
Soft Cuts ($\Gamma = 3.5$)	300	0.6	1.5	1.8	0.0182
Standard Cuts ($\Gamma = 2.5$)	550	0.8	1.4	1.7	0.0144

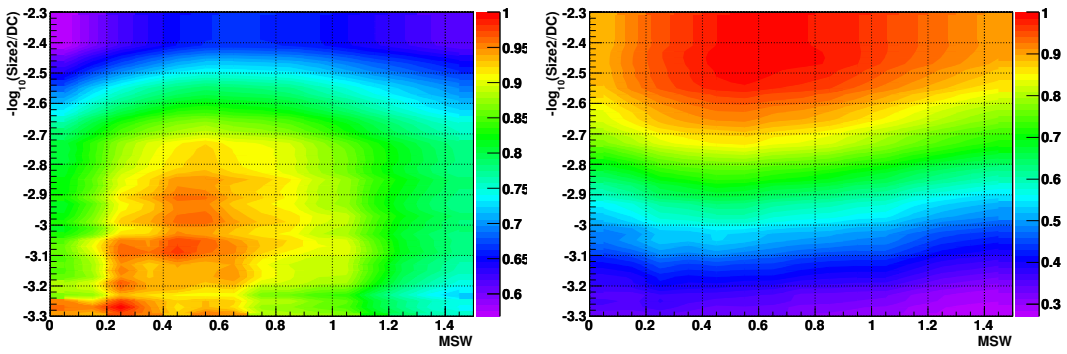

Figure 3.7 Relative signal-to-noise ratio as a function of cut values for MSW and $-\log_{10}$(Size2/DC) for a simulated source with $\Gamma = 2.5$ (**left**) and $\Gamma = 3.5$ (**right**) and a sample of background events from Crab Nebula observations taken in Fall 2009. The gamma-ray event sample was simulated with $Zn = 20°$, $Az = 0°$, and $R_{\mathrm{NSB}} = 0.07$ PE ns^{-1}.

rameter space which is a subset of event parameters calculated in *stage2*. The cut parameters adopted for the ChiLA analysis are the second largest image size in the event (*Size2*) and the three mean scaled parameters defined in Section 3.2.3: *width* (MSW), *length* (MSL), and *disp* (MSD). In principle for each parameter, a range can be found bounding the lowest and highest acceptable values. However for the given parameter set, the application of a lower bound has an insignificant effect on the cut sensitivity and therefore only upper bounds were optimized. An important consideration when defining a set of cuts is the *a priori* expectation for the source spectrum. For the majority of VHE sources detected, the spectrum can be described by a power-law energy distribution $dN/dE \propto E^{-\Gamma}$ where Γ is 2–4. To optimize the detection of weak sources with power-law spectra encompassing this range, two sets of selection cuts were derived using simulations (Table 3.2). An additional optimization condition was imposed to retain at least 20% of the detected photons of the original simulation sample. Figure 3.7 shows a plot of the relative signal-to-noise ratio as a function of cut parameters for *Standard* (optimized for $\Gamma = 2.5$) and *Soft* cuts (optimized for $\Gamma = 3.5$).

3.4 Instrument Response Model

The instrument response model (IRM) is a critical input to the *stage3* analysis as it relates detected events from the direction of the target to the physical characteristics of the source such as absolute gamma-ray flux, spectrum, and angular extent. The IRM is generated by analyzing simulated gamma-rays propagated through the same analysis chain as the data. The IRM is a function of both the hardware configuration with which the data set was taken and the settings, reconstruction algorithms, and cuts that were used for analysis. The ChiLA analysis package incorporates a dedicated tool to derive the three main components

of the IRM: the effective collecting area, point spread function, and the energy response function.

The IRM sensitively depends on the zenith angle of observations and to a lesser degree on the azimuth angle and sky brightness of the observation field. In order to fully model dependence of the IRM on these parameters, a library of response functions is constructed by analyzing a database of gamma-ray simulations generated at discrete pointings (Zn/Az) and sky brightness levels ($R_{\rm NSB}$). Each response function is parameterized as a function of true gamma-ray energy (E) and field angle (ψ) of photon arrival direction with respect to the optical axis of the telescopes. The IRM for an arbitrary pointing and sky brightness level is then interpolated from the set of discrete response functions in the library. In a typical data set, the IRM is a time-dependent quantity as the pointing of the array continuously changes while tracking a target fixed in celestial coordinates. The IRM is therefore calculated as a live-time weighted average over a set of interpolated response functions for discrete time intervals in the data set.

The effective collecting area is the detection cross-section of the instrument to a uniform gamma-ray flux. At a given energy, the gamma-ray detection efficiency is approximately flat with the distance, ρ, from the array center before rapidly falling to zero beyond a certain radius. To compute the gamma-ray effective collecting area, simulated gamma-ray showers are sampled with a random distribution in the plane orthogonal to the mean optical axis of the array out to a maximum distance $\rho_{max}(E_i)$ from the array center which is chosen to be larger than the radius at which the gamma-ray detection efficiency rapidly drops. The effective gamma-ray collecting area at energy E_i is then given by

$$A(E_i) = \pi \rho_{\rm max}(E_i)^2 \epsilon(E_i), \tag{3.20}$$

where $\epsilon(E_i) = N_{\rm sel}(E_i)/N_\gamma(E_i)$ is the gamma-ray detection efficiency, $N_\gamma(E_i)$ is

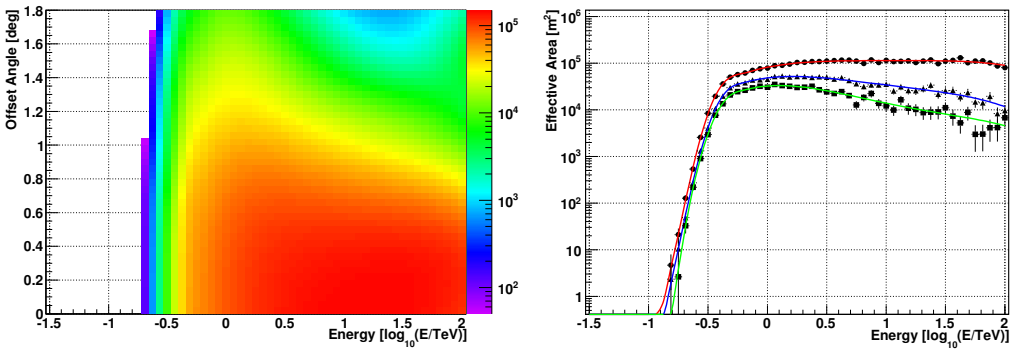

Figure 3.8 **Left:** Model for the effective collecting area as a function of gamma-ray energy and offset angle for a simulated gamma-ray data set with $Zn = 20°$, $Az = 0°$, and $R_{\mathrm{NSB}} = 0.07$ PE ns^{-1} analyzed with *Standard* cuts. **Right:** Model for the effective collecting area from the left figure shown at three discrete offset angles: 0.5° (red line), 1.0° (blue line), and 1.25° (green line). Black data points with error bars show the effective area estimates at discrete simulated energies from which the effective area model was derived.

the total number of simulated gamma rays at each energy, and $N_{\rm sel}(E_i)$ is the number of gamma rays that trigger the detector and pass all selection criteria. The error of the effective area measurement is estimated as

$$\delta A(E_i) = \pi \rho_{\rm max}(E_i)^2 \sqrt{\frac{\epsilon(E_i)\,(1-\epsilon(E_i))}{N_\gamma(E_i)}}. \tag{3.21}$$

Figure 3.8 illustrates the dependence of the collecting area as a function of energy and offset angle. The effective area in $\log A$-$\log E$ space shown in the right panel has two approximately linear regions joined at a break energy, E_0. The collecting area $A(E;\psi_i)$ for an arbitrary energy E and discrete simulated offset angle ψ_i in log-log space is approximated by a 6th order polynomial (f_1) below E_0 and a 5th order polynomial (f_2) above E_0 with the continuity requirements: $f_1(E_0) = f_2(E_0)$ and $f_1'(E_0) = f_2'(E_0)$. The break energy is defined as the minimum energy at which $d\ln A/d\ln E < 2$. After fitting the effective area, $A(E;\psi_i)$, at each discrete offset ψ_i, the model is interpolated to an arbitrary ψ with the use of a cubic spline. The left panel of Figure 3.8 shows an example of the two-dimensional effective area, $A(E;\psi)$, as a continuous function of its arguments. The effective area as a function of energy rises as a power-law with large spectral index of order 8–10 below E_0. For small offset angles ($< 0.5^\circ$) the collecting area remains nearly constant as a function of energy. As the angle ψ increases the effective area declines nearly as a power-law with spectral index 0–0.5. As a function of offset angle, the effective area is monotonically decreasing with ψ and falls more rapidly at high energies. At the camera edge ($\psi = 1.75^\circ$) the gamma-ray throughput is $\sim$0.2 relative to the camera center.

The gamma-ray PSF is used to characterize the distribution of reconstructed directions from a gamma-ray point-source. The PSF is modeled as an azimuthally

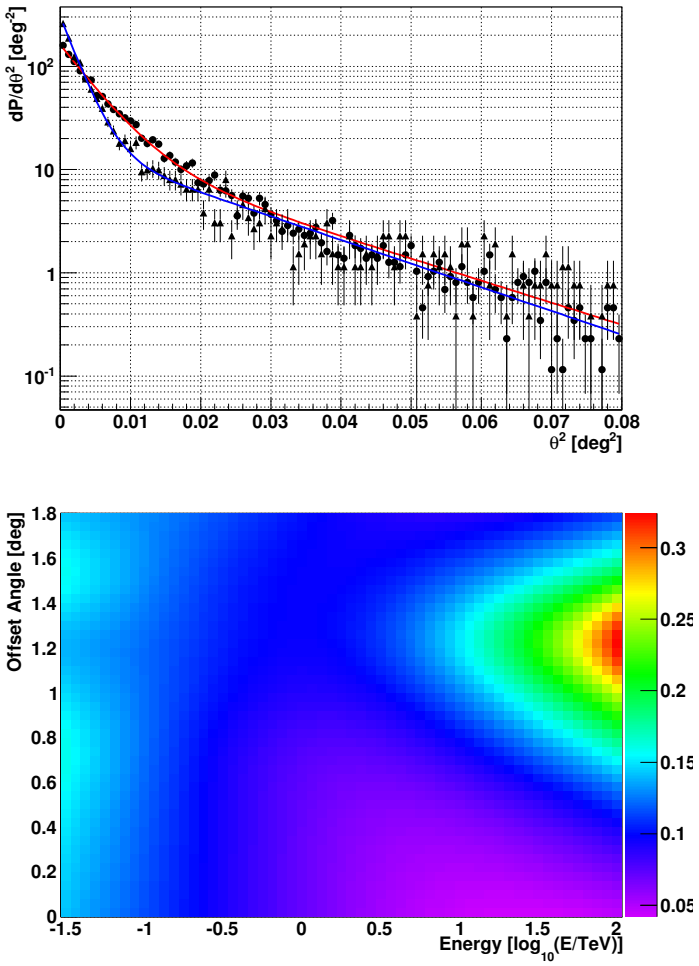

Figure 3.9 **Top:** Gamma-ray PSF as compared to the θ^2 distribution of simulated events with $\psi = 0.5°$ and gamma-ray energies of 316 GeV (black circles and red line) and 1 TeV (blue line and black triangles). The model was derived from a simulation data sample with $Zn = 20°$, $Az = 0°$, and $R_{\rm NSB} = 0.07$ PE ns^{-1} analyzed with *Standard* cuts. **Bottom:** 68% containment radius of the gamma-ray PSF as a function of gamma-ray energy and offset angle for a simulation data sample with $Zn = 20°$, $Az = 0°$, and $R_{\rm NSB} = 0.07$ PE ns^{-1} analyzed with *Standard* cuts.

symmetric two-component gaussian given by

$$\frac{dP}{d\theta^2} = \frac{\alpha}{\sigma_1^2} e^{\frac{-\theta^2}{2\sigma_1^2}} + \frac{(1-\alpha)}{\sigma_2^2} e^{\frac{-\theta^2}{2\sigma_2^2}}, \tag{3.22}$$

where θ is the angle between the true and reconstructed directions, σ_1 and σ_2 are parameters describing the width of the core and tail PSF components respectively ($\sigma_1 < \sigma_2$), and α is a parameter controlling the relative amplitude of these two components. Figure 3.9 shows a comparison of the PSF at two gamma-ray energies and the 68% containment radius of the PSF as a function of energy and offset angle. For a gamma-ray source near the center of the FoV, the angular resolution improves monotonically with energy. At larger offsets, the angular resolution degrades at the highest energies due to truncation effects at the edge of the FoV.

The energy response function (ERF) is the p.d.f. for reconstructed energy E' given a true energy E and is directly tied to the choice of estimator used for energy reconstruction (Section 3.2.4). The ERF is modeled as a sum of two gaussians in logarithmic energy,

$$\frac{dR(E';E)}{d\log_{10} E'} = \frac{\alpha}{\sqrt{2\pi\sigma_1^2}} \exp\left[-\frac{(\log_{10} E' - b_1)^2}{2\sigma_1^2}\right] + \frac{1-\alpha}{\sqrt{2\pi\sigma_2^2}} \exp\left[-\frac{(\log_{10} E' - b_2)^2}{2\sigma_2^2}\right] \tag{3.23}$$

with four free parameters $\{\sigma_1(\log_{10} E), b_1(\log_{10} E), \sigma_2(\log_{10} E), b_2(\log_{10} E)\}$ corresponding to the mean and dispersion of each gaussian which are treated as smooth functions of the gamma-ray energy, E. The introduction of two gaussian distributions was motivated by the necessity to model small asymmetries present in the simulated distributions. To remove significant degeneracies when fitting the ERF parameters, the amplitude parameter, α, is fixed to 0.8. This choice provides good ERF fits to the reconstructed energy distributions for all energies of interest. The logarithmic bias and energy resolution (Equation 3.19)

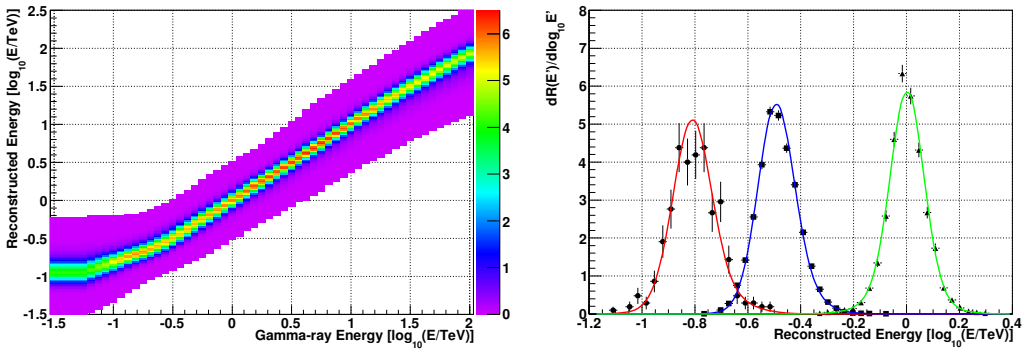

Figure 3.10 **Left:** ERF, $dR(E';E)/d\log_{10}E'$, of the energy estimator derived using the *InverseSizeTable* method and $\mathbf{p} = \{\rho, disp\}$ and a sample of simulated gamma-rays with $\psi = 0.5°$, $Zn = 20°$, $Az = 0°$, and $R_{\rm NSB} = 0.07$ PE ns^{-1}. **Right:** ERF from the left figure compared to the reconstructed energy distribution of simulated gamma-rays at three discrete gamma-ray energies: 100 GeV (black circles and red line), 316 GeV (black squares and blue line), and 1 TeV (black triangles and green line).

are related to the ERF parameters as

$$\begin{aligned} \delta \log_{10} E &= \log_{10} E - \alpha b_1 - (1-\alpha) b_2 \\ (\Delta \log_{10} E)^2 &= \alpha \sigma_1^2 + (1-\alpha)\, \sigma_2^2 + \alpha\,(1-\alpha)\,(b_1 - b_2)^2 \,. \end{aligned} \tag{3.24}$$

Figure 3.10 illustrates the general characteristics of a typical ERF. At intermediate energies (316 GeV $\lesssim E \lesssim$ 10 TeV) the energy estimator is relatively symmetric and unbiased ($b_1 = b_2 \simeq \log_{10} E$). In the lower energy domain (E $\lesssim$ 316 GeV) the reconstructed energy, E', systematically overestimates the true energy, the energy response function becomes asymmetric, and the energy resolution ($\Delta \log_{10} E$) related to σ_1 and σ_2 deteriorates.

3.5 Background Modeling

After gamma-ray selection cuts have been applied to the event sample, maps of the distribution of event directions in the celestial coordinate frame of right ascension and declination, $\{\alpha, \delta\}$, are created. In a typical data set, the event distribution is dominated by the smooth and relatively flat distribution of residual background (cosmic-ray) events surviving the gamma-ray selection. Gamma-ray sources within the field of observations are identified by searching for significant deviations in the background in these maps. Therefore detailed understanding of the cosmic-ray background has direct implications on VERITAS sensitivity, particularly for weak gamma-ray sources.

The background modeling analysis is performed in a two-dimensional cartesian coordinate system $\mathbf{r} = \{x_\alpha, x_\delta\}$ which is a projection of the celestial coordinate system onto the tangent plane at an origin point $\boldsymbol{\theta}_0 = \{\alpha_0, \delta_0\}$. A data set consists of a series of exposures taken while the VERITAS array tracks J discrete positions with coordinates $\boldsymbol{r}_j$. The standard observing strategy used for the ma-

jority of VERITAS observations is the *wobble* technique wherein observations are alternately taken at a set of four discrete positions at the same offset (typically 0.5 degrees) relative to the nominal source position. Because the main features in the distribution of the background are set by the event positions relative to the camera center, each event is identified by both a position vector and an associated pointing index.

The analysis of the distribution of projected event arrival directions is performed in two stages. First, a camera acceptance function (Section 3.5.1) is fit to the data in order to model the background distribution in the absence of gamma-ray sources. The significance and amplitude of a gamma-ray excess at an arbitrary point in the observed field is then determined using one of three methods: the *reflected-region* method (Section 3.5.2), the *ring-background* method (Section 3.5.3), and the *maximum-likelihood* method (Section 3.5.4). The first two methods are the standard VERITAS analysis techniques (Acciari et al., 2008) and have been extensively studied (Berge et al., 2007). A more detailed description of the *maximum-likelihood* method has been presented in a VERITAS collaboration memo (Wood & Vassiliev, 2009).

3.5.1 Camera Acceptance

The distribution of residual background events in celestial coordinates is approximately centered on the array pointing and approaches zero at offset angles beyond the edge of the FoV ($\psi \gtrsim 1.75^\circ$). The distribution of these events is modeled using the camera acceptance function ($\xi(\boldsymbol{r} - \boldsymbol{r}_j)$), the p.d.f. for the background distribution in the $\boldsymbol{r}$ coordinate system centered on the array tracking coordinate, $\boldsymbol{r}_j$. To first order, ξ is an azimuthally symmetric function of its argument. To higher orders, statistically significant deviations from azimuthal symmetry such as gra-

dients across the FoV may also be present. The camera acceptance is influenced by both the conditions under which a set of observations were taken (e.g. zenith angle) and the selection cuts that are applied to the data. In the implementation adopted for the ChiLA package, the acceptance function is treated as a unique distribution for each data set. It is therefore estimated only from the given data sample and does not incorporate any prior information from simulations or data taken under similar observing conditions.

An important consideration when modeling the camera acceptance is the presence of stars and known gamma-ray sources both of which can introduce small scale structures in the event distribution. Pixels in the vicinity of a bright star are automatically suppressed by the high-voltage software which results in a deficit of reconstructed events at the position of the star on the scale of $\sim 0.3^{\circ}$. The effect of stars on the reconstructed counts distribution is greatest for analyses with a low $Size2$ cut. The characteristic scale of the distribution of the cosmic-ray background is significantly larger than these small scale structures and comparable to the size of the camera FoV. Therefore when modeling the acceptance function, a 0.4° region is excluded around each known star ($M_V < 6$) and gamma-ray point-source.

A parameterization for the camera acceptance, $\xi(\boldsymbol{\rho})$, which is the square of a Bessel series expansion in polar coordinates $\{\rho, \phi\}$ was developed in Wood & Vassiliev (2009),

$$\xi(\boldsymbol{\rho}; \boldsymbol{\theta} = \{\delta c_{01}, \ldots, \delta c_{mn}\}) = \frac{1}{\pi R^2} \left| c + \sum_{m=-\infty}^{\infty} \sum_{n=1}^{\infty} \delta c_{mn} \frac{J_{|m|}\left(\frac{\lambda_{mn}\rho}{R}\right)}{J_{|m|+1}(\lambda_{mn})} e^{im\phi} \right|^2 , \quad (3.25)$$

where $\delta c_{mn} = (\delta c_{-mn})^* = |\delta c_{mn}| e^{i\phi_{mn}}$ are free parameters and the coefficient c is fixed by the condition that the function be normalized to one over the circle of radius R. The coefficients δc_{mn} are found by application of the maximum likelihood

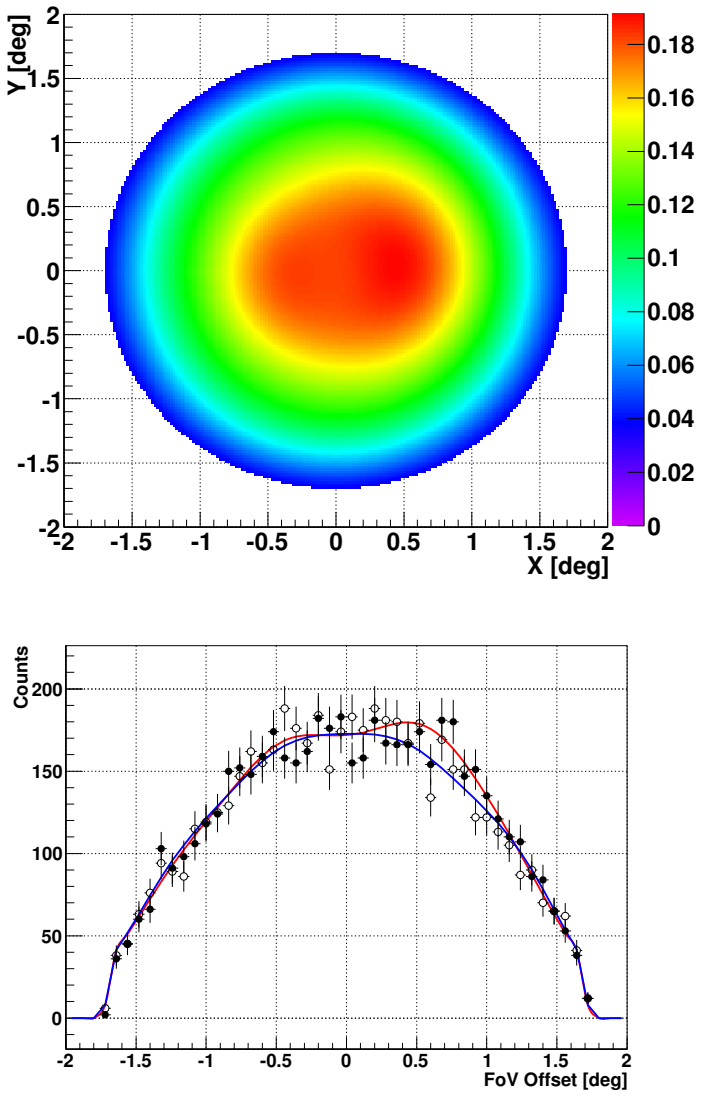

Figure 3.11 **Top:** Camera acceptance function, ξ, for the 2009-2010 RGB J1351+112 data set analyzed with *Soft* cuts. **Bottom:** Projection of the acceptance function in the top figure compared to the projected counts distribution for the regions with $-0.1^\circ < Y < 0.1^\circ$ (filled circles and red line) and $-0.1^\circ < X < 0.1^\circ$ (open circles and blue line).

method and the requirement that the coefficients have values that statistically significantly differ from zero. The introduction of 4 $m = 0$, 2 $m = 1$, and 1 $m = 2$ coefficients was found to be sufficient to fit the background distribution for the majority of VERITAS observations. For example, Figure 3.11 shows the camera acceptance function derived using the parameterization of Equation 3.25 for the RGB J1351+112 dataset taken in 2009-2010. The counts distribution for this data set is characterized by a statistically significant gradient with $|\delta c_{11}| = 0.20 \pm 0.04$ and $\phi_{11} = 18 \pm 10$.

3.5.2 Reflected Region Method

The *reflected-region* method evaluates the significance and amplitude of a gamma-ray signal by calculating the counts excess within a circular aperture (ON Region) of radius θ_0 centered at the trial position, $\mathbf{r}_i$. The background amplitude in the ON region is estimated from the number of events in a set of non-overlapping OFF regions of equal radius that are offset by the same distance ψ from the center of the FoV. The number of OFF regions is generally chosen to fill the entire ring of radius ψ outside of a source exclusion region around the test position. Events falling in any of the predefined star or gamma-ray source regions are excluded from the background estimate. The geometric arrangement of ON and OFF regions is illustrated in Figure 3.12.

The counts excess in the ON region is given by

$$n_e = \sum_j \left[n_{s,j} - \alpha_j n_{b,j} \right], \tag{3.26}$$

where $n_{s,j}$ and $n_{b,j}$ are the number of counts detected in the ON and OFF regions respectively for pointing j and α_j is the ratio of the solid angles subtended by the ON and OFF regions. In the simplest case in which the OFF regions do

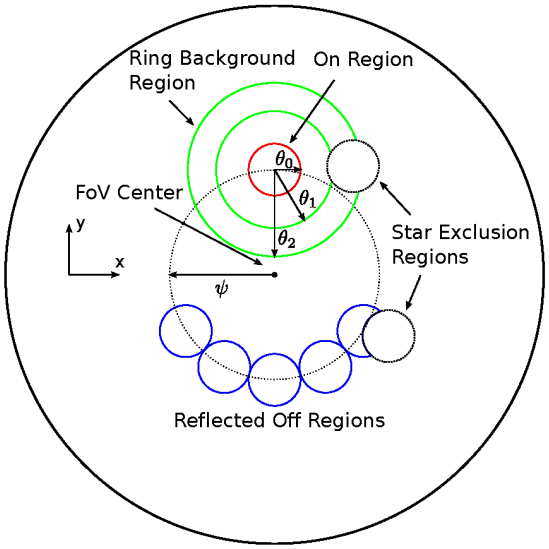

Figure 3.12 Illustration of the geometry for ON and OFF regions in the camera FoV used in the *reflected-region* and *ring-background* background methods.

not overlap any exclusion regions, $\alpha_j = 1/N_b$ where N_b is the number of OFF regions. The significance of a counts excess in the ON region is evaluated from the logarithm of the likelihood ratio. The likelihoods are calculated for two hypotheses, null and non-zero signal, using Poisson statistics. The significance is given as

$$\sigma = \sqrt{2}\left[n_s \ln \frac{n_s}{\sum_j \alpha_j \left(1+\alpha_j\right)^{-1} \left(n_{s,j}+n_{b,j}\right)} + n_b \ln \frac{n_b}{\sum_j \left(1+\alpha_j\right)^{-1} \left(n_{s,j}+n_{b,j}\right)} \right]^{1/2}, \tag{3.27}$$

where $n_s = \sum_j n_{s,j}$ and $n_b = \sum_j n_{b,j}$.

Because the *reflected-region* method relies on the assumption of azimuthal symmetry, it is highly susceptible to systematic errors in background estimation. For example in the presence of a linear gradient, the systematic error in background estimation increases as the trial position is moved away from the center

of the FoV. For a data set taken with the *wobble* technique, this systematic error approximately cancels at the source coordinate if an equal number of observations are taken in each wobble direction. Because the background is estimated from the regions significantly offset from the trial position, any non-uniformities in the background distribution in the FoV may also result in considerable systematic errors. Due to these deficiencies, the *reflected-region* method is not suitable as a general purpose tool for background estimation and is normally used for spectral analysis only (see Section 3.6).

3.5.3 Ring Background Method

The *ring-background* method is an aperture-based technique that partially corrects for departures from azimuthal symmetry in the background distribution. The excess in a circular ON region of radius θ_0 is evaluated using the background amplitude in an annular OFF region centered on the the trial position with inner and outer radii, $\{\theta_1, \theta_2\}$ (see Figure 3.12). The acceptance normalization factor, α_j, for trial position $\boldsymbol{r}_i$ and pointing j is given by the ratio of the integral of the camera acceptance, $\xi(\boldsymbol{r})$, over the ON and OFF regions,

$$\alpha_j(\boldsymbol{r}_i) = \frac{\int_0^{2\pi}\int_0^{\theta_0} \xi(\boldsymbol{r}_i - \boldsymbol{r}_j - \boldsymbol{r}')r'dr'd\phi}{\int\int_A \xi(\boldsymbol{r}_i - \boldsymbol{r}_j - \boldsymbol{r}')r'dr'd\phi}, \tag{3.28}$$

where A is the region of the background annulus that does not intersect any exclusion regions. The counts excess and its significance is calculated using Equations 3.26 and 3.27. Because the background estimate incorporates information from the camera acceptance, the ring background method can explicitly compensate for linear gradients in the FoV and partially for higher order structures in the background distribution on the scales larger than the annular ring size. Increasing the size of the annular region improves the sensitivity of the method due to better estimation of the background but diminishes the ability of the

method to compensate for local structures in the background distribution in the vicinity of the source position. For the detection in the background-dominated regime, the increase in sensitivity scales as $\sqrt{1+\alpha}$ as the ring size increases. The parameters of the ring background method adopted for the ChiLA analysis are $\{\theta_1, \theta_2\} = \{0.4^\circ, 0.5^\circ\}$. When θ_0 is chosen to be 0.12°, the approximate value of α in the central regions of the camera is 0.16.

3.5.4 Maximum Likelihood Method

The *maximum-likelihood* method fits a two-dimensional multi-parameter counts model to the binned event distribution. The bin occupation, n_{ij}, is calculated with a bin size $\Delta\Omega$ and bin coordinates $\mathbf{r}_{ij}$ for a set of J pointings where i and j indices designate the sky coordinate and pointing respectively. A counts model, $\nu(\boldsymbol{r}_{ij};\boldsymbol{\theta})$, is constructed to predict the expectation value for the bin occupations n_{ij} as a function of the free parameters, $\boldsymbol{\theta}$. The maximum likelihood estimates for the model parameters, $\hat{\boldsymbol{\theta}}$, are determined by maximizing the log likelihood function,

$$\ln L(\mathbf{n}|\boldsymbol{\theta}) = \sum_{j=1}^{J}\sum_{i=1}^{N_j}\left[n_{ij}\ln\nu(\boldsymbol{r}_{ij};\boldsymbol{\theta}) - \nu(\boldsymbol{r}_{ij};\boldsymbol{\theta}) - \ln n_{ij}!\right], \tag{3.29}$$

with respect to the free parameters $\boldsymbol{\theta}$ where the summation is carried out over N_j bins for each of J pointings. Exclusion regions are incorporated into the model by removal of bins from the summation.

The counts model is decomposed into contributions from signal (gamma-ray) and background (residual cosmic-ray) components. The signal component is calculated as a convolution integral,

$$\nu_s(\boldsymbol{r}_{ij};\boldsymbol{\theta}_s) = \Delta\Omega\tau_j \int\int d^2\boldsymbol{r}' dE' \frac{dA_j(E', \boldsymbol{r}' - \boldsymbol{r}_{ij}, \boldsymbol{r}' - \boldsymbol{r}_j)}{d\Omega} f_\gamma(\boldsymbol{r}', E';\boldsymbol{\theta}_s), \tag{3.30}$$

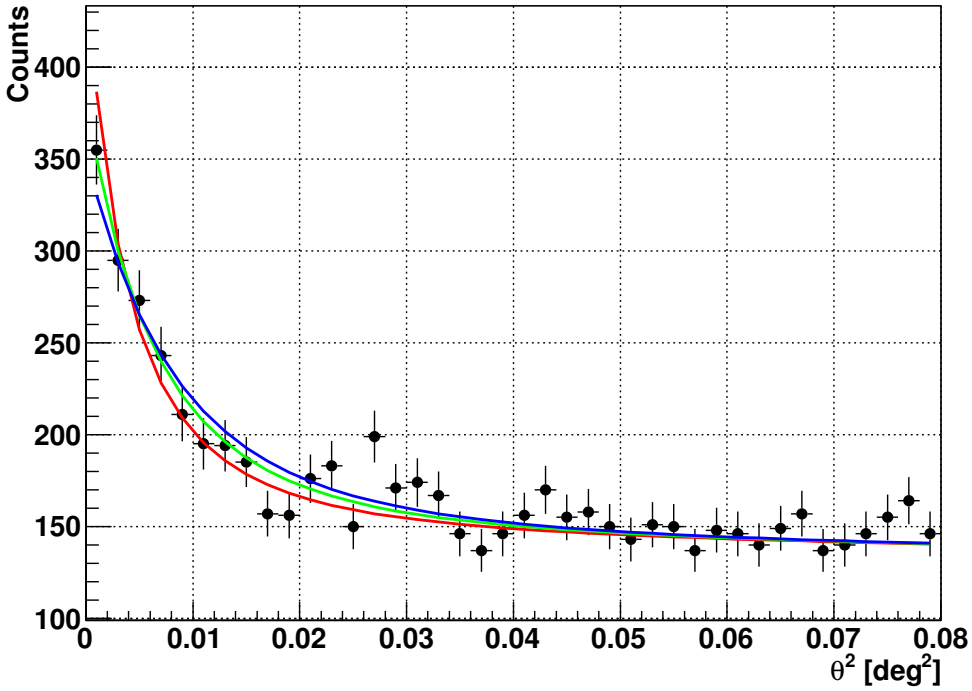

Figure 3.13 Comparison of the θ^2 distribution for the PG1553+200 data set taken in 2009-2010 and the point-source models with free parameters estimated using the *maximum-likelihood* method for three different choices of spectal index: $\Gamma = 2.5$ (red line), $\Gamma = 3.5$ (green line), $\Gamma = 4.5$ (blue line).

where τ_j is the cumulative livetime for observations taken at pointing j, $\boldsymbol{r}_j$ is the tracking coordinate, $dA_j/d\Omega$ is the livetime weighted product of the effective area and PSF response functions (Section 3.4) for pointing j, and $f_\gamma(\boldsymbol{r}, E; \boldsymbol{\theta}_s)$ is the intrinsic angular distribution and differential spectrum of the source. For example, a point source at the coordinate $\boldsymbol{r}_0$ with a power-law energy distribution is expressed as

$$f_\gamma(\boldsymbol{r}, E; \boldsymbol{\theta}_s = \{F_0, \Gamma, \boldsymbol{r}_0\}) = F_0 \left(\frac{E}{E_0}\right)^{-\Gamma} \delta(\boldsymbol{r} - \boldsymbol{r}_0). \tag{3.31}$$

Due to the dependence of the PSF and effective area on energy, the signal model is weakly dependent on the choice of the power-law index, Γ (see Figure 3.13). The background model is constructed by introducing a set of free normalization parameters, B_j, for each of the J pointings which are used to scale the camera acceptance function,

$$\nu_b(\boldsymbol{r}_{ij}; \boldsymbol{\theta}_b = \{B_1, \ldots, B_J, \boldsymbol{\theta}_\xi\}) = \Delta\Omega B_j \xi(\boldsymbol{r}_{ij} - \boldsymbol{r}_j; \boldsymbol{\theta}_\xi), \tag{3.32}$$

where $\boldsymbol{\theta}_\xi$ are the free parameters of the acceptance function defined in Section 3.5.1.

The optimization of the likelihood function is performed numerically using an iterative search technique. A suitable starting point in the space of model parameters is found analytically using the formulae presented in Wood & Vassiliev (2009). Once the optimal parameters are found, the significance of a gamma-ray source is determined by forming the log likelihood ratio for the null and non-zero excess hypotheses,

$$\ln \Lambda = \ln L(\mathbf{n}|\hat{\boldsymbol{\theta}}'_b) - \ln L(\mathbf{n}|\hat{\boldsymbol{\theta}}_b, \hat{\boldsymbol{\theta}}_s) \tag{3.33}$$

where $\hat{\boldsymbol{\theta}}'_b$ are the maximum likelihood estimates of the background model parameters under the null hypothesis and $\hat{\boldsymbol{\theta}}_b$ and $\hat{\boldsymbol{\theta}}_s$ are the maximum likelihood estimates of the background and signal model parameters under the non-zero

excess hypothesis. According to Wilks' theorem, $-2\ln\Lambda$ is asymptotically distributed as χ^2 with S degrees of freedom, where S is the difference in the number of free parameters between the two hypotheses.

3.6 Spectral Reconstruction

The spectral reconstruction of a source is the determination of its intrinsic source spectrum in true gamma-ray energy, E, from the measured spectrum of reconstructed event energies, E'. In terms of the logarithmic energy variable $x = \log_{10} E$, the reconstructed energy spectrum, dN/dx', is related to the true spectrum, $d\phi/dx$, by the integral equation,

$$\frac{dN}{dx'} = \tau \int \frac{dR(x';x)}{dx'} A(x) \frac{d\phi}{dx} dx, \tag{3.34}$$

where τ is the livetime, $A(x)$ is the gamma-ray effective area, and $dR(x';x)/dx'$ is the energy response function (Section 3.4). Equation 3.34 is discretized into a system of linear equations by integrating over logarithmic bins in true and and reconstructed energy,

$$\int_{x'_i-\Delta'/2}^{x'_i+\Delta'/2} \frac{dN}{dx'} dx' = \tau \sum_j \int_{x'_i-\Delta'/2}^{x'_i+\Delta'/2} \int_{x_j-\Delta/2}^{x_j+\Delta/2} \frac{dR(x';x)}{dx'} A(x) \frac{d\phi}{dx} dx dx', \tag{3.35}$$

where x'_i and x_j are the central logarithmic energies for reconstructed energy bin i and true energy bin j and Δ and Δ' are the logarithmic bin widths in true and reconstructed energy. Expressed as matrix equation of a vector $\boldsymbol{\phi}$,

$$\phi_j = \int_{x_j-\Delta/2}^{x_j+\Delta/2} \frac{d\phi}{dx} dx, \tag{3.36}$$

and kernel matrix $\mathbf{K}$,

$$K_{ij} = \frac{\tau}{\phi_j} \int_{x'_i-\Delta/2}^{x'_i+\Delta/2} \int_{x_j-\Delta/2}^{x_j+\Delta/2} \frac{dR(x';x)}{dx'} A(x) \frac{d\phi}{dx} dx' dx, \tag{3.37}$$

Equation 3.35 becomes

$$\nu_i = \sum_j K_{ij}\phi_j, \tag{3.38}$$

where ν_i is the expectation value for the number of events in reconstructed energy bin i and ϕ_j is the integral flux in true energy bin j. In general the kernel matrix depends on the intrinsic spectral properties of the source. The choice of bin size used to calculate the kernel matrix is motivated by the characteristic scale, σ, of the response function and the anticipated spectral properties of the source. For the astrophysical sources that can be described by a power-law spectrum within the energy range comparable to the width of the response function, σ, and with characteristic bin size of order $\sigma/2$ the matrix $\mathbf{K}$ depends weakly on the exact choice of the spectral index Γ. The kernel matrix is thus calculated assuming $d\phi/dx \propto E^{-\Gamma+1}$ with $\Gamma = 2.5$ for all subsequent analysis. In principle, the accuracy of spectral reconstruction could be iteratively refined by substituting $d\phi/dx$ with the reconstructed spectrum and including corrections to the matrix K. However such corrections are on the scale of 1–2% which is significantly smaller than typical systematic errors ($\sim 10\%$).

The distribution of reconstructed energies Υ_j obeys Poisson statistics with the expectation values,

$$\bar{\boldsymbol{\Upsilon}}_s = \mathbf{K}\boldsymbol{\phi} + \alpha\boldsymbol{\nu}_b, \tag{3.39}$$

where $\alpha\boldsymbol{\nu}_b$ is the vector of background expectation values. For each energy bin, $\nu_{b,j}$ is estimated utilizing the *reflected-region* method described in Section 3.5.2. Distributions of reconstructed energies, $\boldsymbol{\Upsilon}_s$ and $\boldsymbol{\Upsilon}_b$, are accumulated from the ON region centered on the source position and from the set of reflected OFF regions. The excess vector due to the signal in the on region is

$$\boldsymbol{\Upsilon}_e = \boldsymbol{\Upsilon}_s - \alpha\boldsymbol{\Upsilon}_b. \tag{3.40}$$

Because the energy bins are uncorrelated, the covariance matrix of $\boldsymbol{\Upsilon}_e$ is diagonal with elements given by

$$V_{ii} = \Upsilon_{s,i} + \alpha^2 \Upsilon_{i,b}. \tag{3.41}$$

While the *ring-background* and *maximum-likelihood* methods are both more robust to gradients and structures in the background distribution, the application of these methods to spectral analysis would require an energy-dependent model for the camera acceptance. The introduction of a third dimension to the acceptance function significantly reduces the available statistics in individual bins and therefore the construction of such a model would need to rely upon results of high-statistics simulations or additional physical considerations about the energy-dependence of the acceptance function. On the other hand, if the assumption of azimuthal symmetry is valid, the *reflected-region* method allows extraction of the energy dependence of the expected background without an explicit model for the camera acceptance. As discussed in Section 3.5.2, the *reflected-region* method also partially corrects for a gradient in the background distribution when the ON region is at or near the *wobble* position which is typically the case for targeted observations.

Inferring the source spectrum given an equation of the form of Equation 3.39 is an ill-defined inverse problem with the exception of trivial cases for the matrix $\mathbf{K}$. Direct inversion of the response matrix is frequently unstable due to the existence of small eigenvalues and the non-zero projection of the corresponding eigenvectors on the statistically fluctuating measurement vector. Thus small statistical fluctuations in the measurement vector are amplified into large statistical fluctuations in the solution vector. To alleviate this problem, several approaches to inferring the source spectrum have been implemented in the ChiLA package. The *forward-folding* method (Section 3.6.1) adopts an analytic model for the true spectrum

and solves for the small set of model parameters that best fit the measured distribution. The alternative family of techniques known as regularized unfolding methods make weaker, frequently integral assumptions about the underlying form of the true distribution and can be used to generate a non-parametric spectral model. A subclass of this family, the *correction-factors* method (Section 3.6.3), derives estimates for the true spectrum by multiplying the reconstructed distribution by a set of scaling factors which are then iteratively refined using successive estimates of the true spectrum. The *regularized-unfolding* method (Section 3.6.2) uses the full information of the response matrix $\mathbf{K}$ and unfolds the solution by imposing a constraint on the smoothness of the solution.

3.6.1 Forward-Folding

The *forward-folding* method assumes that the true spectrum can be accurately described by elementary functions with a small number of free parameters. For a number of VHE gamma-ray sources, the true spectrum can be well approximated with a power-law, $d\phi/dE = F_0 \left(E/E_0\right)^{-\Gamma}$, with two free parameters $\boldsymbol{\theta} = \{F_0, \Gamma\}$. The expectation value for the signal amplitude in each bin of reconstructed energy is found by folding the distribution $\boldsymbol{\phi}$ with the response matrix $\mathbf{K}$,

$$\boldsymbol{\nu}_s(\boldsymbol{\theta}_s) = \mathbf{K}\boldsymbol{\phi}(\boldsymbol{\theta}_s). \tag{3.42}$$

The log likelihood function for the energy distributions in the ON and OFF regions, $\boldsymbol{\Upsilon}_s$ and $\boldsymbol{\Upsilon}_b$, with acceptance correction α is given by,

$$\begin{aligned} \ln L(\boldsymbol{\Upsilon}_s, \boldsymbol{\Upsilon}_b | \boldsymbol{\theta}_s, \boldsymbol{\nu}_b) = & \\ \sum_i^N \Big[& \Upsilon_{s,i} \ln\left(\nu_{s,i}(\boldsymbol{\theta}_s) + \alpha\nu_{b,i}\right) - \ln \Upsilon_{s,i}! - \nu_{s,i}(\boldsymbol{\theta}_s) - \alpha\nu_{b,i} \\ & + \Upsilon_{b,i} \ln\left(\nu_{b,i}\right) - \nu_{b,i} - \ln \Upsilon_{b,i}! \Big] \end{aligned} \tag{3.43}$$

where $\boldsymbol{\nu}_b$ are the expectation values for the background amplitudes in the reconstructed energy bins. The maximum likelihood estimates for $\boldsymbol{\nu}_b$ are found by solving the sequence of equations,

$$\frac{\partial \ln L}{\partial \nu_{b,i}} = \frac{\Upsilon_{b,i}}{\nu_{b,i}} + \frac{\alpha \Upsilon_{s,i}}{\nu_{s,i} + \alpha \nu_{b,i}} - (1+\alpha) = 0, \tag{3.44}$$

which has the solution for $\nu_{b,i}$ in terms of $\nu_{s,i}$,

$$\hat{\nu}_{b,i} = \frac{\nu_{b0,i}}{2} - \frac{\nu_{s,i}}{2\alpha} + \left[\frac{\Upsilon_{b,i}\nu_{s,i}}{\alpha\,(1+\alpha)} + \left(\frac{\nu_{b0,i}}{2} - \frac{\nu_{s,i}}{2\alpha} \right)^2 \right]^{1/2}, \tag{3.45}$$

where $\nu_{b0,i} = (\Upsilon_{b,i} + \Upsilon_{s,i}) / (1+\alpha)$ is the maximum likelihood estimate when $\nu_s = 0$. After substituting the background estimates from Equation 3.45 into the log likelihood function, the only free parameters of the model are those associated with the spectrum, $\boldsymbol{\theta}_s$. The maximization of the likelihood with respect to the free parameters is performed using the Levenberg-Marquardt numerical algorithm (Press, 2002). Figure 3.14 illustrates the forward-folding technique as applied to the data set from the source 1ES0229+200 taken in 2009–2010.

3.6.2 Regularized Unfolding Method

The inversion of

$$\bar{\boldsymbol{\Upsilon}}_e = \mathbf{K}\boldsymbol{\phi} \tag{3.46}$$

is an ill-posed problem and the application of standard techniques for solving a system of linear equations results in a solution that may become sensitive to small perturbations in the data. The strategy used by the *regularized-unfolding* method is to impose an *a priori* constraint on the solution by the introduction of a penalty function. The inversion procedure is formulated as an optimization problem by constructing a modified chi-squared functional,

$$\chi^2 = (\boldsymbol{\Upsilon}_e - \mathbf{K}\boldsymbol{\phi})^T \mathbf{V}^{-1} (\boldsymbol{\Upsilon}_e - \mathbf{K}\boldsymbol{\phi}) + \lambda \boldsymbol{\phi}^T \mathbf{L}^T \mathbf{L} \boldsymbol{\phi}, \tag{3.47}$$

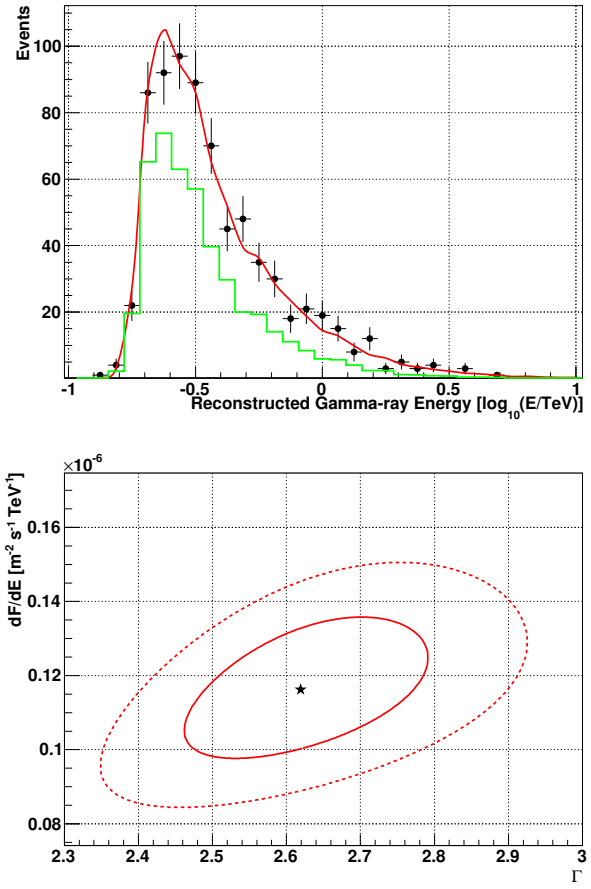

Figure 3.14 **Top:** Reconstructed energy distribution of 1ES0229+200 within the ON source aperture with $\theta_0 = 0.12°$. Black points indicate the unsubtracted counts distribution. Shown for comparison are the maximum likelihood estimates for the background in each bin, $\hat{\boldsymbol{\nu}}_b$, (green line) and background plus signal, $\hat{\boldsymbol{\nu}}_b + \boldsymbol{\nu}_s(\hat{\boldsymbol{\theta}})$ (red line). **Bottom:** Likelihood contours for 68% (solid line) and 90% (dashed line) C.L. corresponding to the spectral fit shown in the top figure. The star indicates the best fit spectral model corresponding to $F_0 = 1.16 \times 10^{-7}$ m^{-2} s^{-1} TeV^{-1} and $\Gamma = 2.62$ with $E_0 = 316$ GeV.

where $\mathbf{L}$ is the regularization matrix and λ is the regularization parameter. When applying the regularized unfolding method, the kernel matrix is chosen to be m-by-n with $m \gtrsim 2n$ which ensures that the solution vector is over-constrained by the data. The first term in Equation 3.47 prefers solutions that satisfy Equation 3.46 while the second term prefers solutions determined by the eigenvectors and eigenvalues of the $\mathbf{L}^T\mathbf{L}$ matrix. The relative importance of these two terms is controlled by the parameter λ. The solution vector that minimizes Equation 3.47 can be found by solving,

$$\frac{\partial \chi^2}{\partial \boldsymbol{\phi}} = -2\mathbf{K}^T\mathbf{V}^{-1}\left(\boldsymbol{\Upsilon}_e\right) + 2\left(\mathbf{K}^T\mathbf{V}^{-1}\mathbf{K} + \lambda\mathbf{L}^T\mathbf{L}\right)\boldsymbol{\phi} = 0, \tag{3.48}$$

which gives

$$\hat{\boldsymbol{\phi}} = \left(\mathbf{K}^T\mathbf{V}^{-1}\mathbf{K} + \lambda\mathbf{L}^T\mathbf{L}\right)^{-1}\mathbf{K}^T\mathbf{V}^{-1}\boldsymbol{\Upsilon}_e = \mathbf{B}^T\boldsymbol{\Upsilon}_e. \tag{3.49}$$

The covariance matrix of the solution vector in the gaussian regime is given by

$$\mathbf{V}_\phi = \mathbf{B}^T\mathbf{V}\mathbf{B}. \tag{3.50}$$

The sensitivity of the unregularized solution (obtained from Equation 3.49 when $\lambda = 0$) to small perturbations in the data vector arises due to the small eigenvalues of the matrix $\mathbf{K}^T\mathbf{V}^{-1}\mathbf{K}$. Using the decomposition $\mathbf{K}^T\mathbf{V}^{-1}\mathbf{K} = \mathbf{U}\boldsymbol{\Sigma}\mathbf{U}^T$ with $\boldsymbol{\Sigma} = diag(\sigma_1, \sigma_2, \ldots, \sigma_n)$ and $\sigma_1 \geq \ldots \geq \sigma_n$, the unregularized solution in the eigenvector basis of $\mathbf{K}^T\mathbf{V}^{-1}\mathbf{K}$ is

$$\boldsymbol{\phi} = \mathbf{U}\boldsymbol{\Sigma}^{-1}\mathbf{U}^T\mathbf{b} = \sum_j \frac{c_j}{\sqrt{\sigma_j}}\mathbf{u}_j, \tag{3.51}$$

where $\mathbf{b} = \mathbf{K}^T\mathbf{V}^{-1}\boldsymbol{\Upsilon}_e$, $c_j\sqrt{\sigma_j} = \left(\mathbf{U}^T\mathbf{b}\right)_j$, and $\mathbf{u}_j$ are the column vectors of $\mathbf{U}$. Thus the solution vector is a superposition of the eigenvectors $\mathbf{u}_j$ each weighted by a coefficient c_j with unit variance and the inverse of the square root of the associated eigenvalue $1/\sqrt{\sigma_j}$. Figure 3.15 illustrates the eigenvectors, eigenvalues,

and eigenvector coefficients obtained for the reconstruction of a simulated source with 10^4 photons and a power-law spectrum with $\Gamma = 2.5$. The instability of the unregularized solution is seen to arise from the terms in the eigenvector expansion with small eigenvalues for which the fluctuations in the data result in a non-zero coefficients c_j. The division by the small eigenvalues amplifies the statistical error in these high-frequency terms which leads to the large observed oscillations in the unregularized solution.

The introduction of the regularization term is motivated to damp the contribution of eigenvectors with small eigenvalues. The choice of the regularization matrix $\mathbf{L}$ is motivated by *a priori* assumptions about the properties of the spectrum. A common choice of regularization is the class of *Tikhonov* regularization functionals (Tikhonov & Arsenin, 1977) where the regularization term is equal to the integrated square of the kth derivative:

$$\int \left(\frac{d^k}{dE^k} \frac{d\phi}{dE} \right)^2 dE. \tag{3.52}$$

For the discrete solution vector $\boldsymbol{\phi}$, the derivate of order k is approximated by finite differences as $\mathbf{L}_k \boldsymbol{\phi}$ where $\mathbf{L}_k$ is the regularization matrix. When $k = 0$, the regularization matrix is equal to the identity matrix, $\mathbf{L}_0 = \mathbf{I}$, and the regularization term is equal to the norm of the solution vector. When $k = 1$, the finite difference approximation to the derivative is represented by the $(n-1)$-by-n matrix,

$$\mathbf{L}_1 = \begin{pmatrix} -1 & 1 & 0 & 0 & \dots & & \\ 0 & -1 & 1 & 0 & \dots & & \\ & & & \ddots & & & \\ & & \dots & 0 & -1 & 1 & 0 \\ & & \dots & 0 & 0 & -1 & 1 \end{pmatrix}. \tag{3.53}$$

One difficulty that arises in applying Tikhonov regularization is that the typical

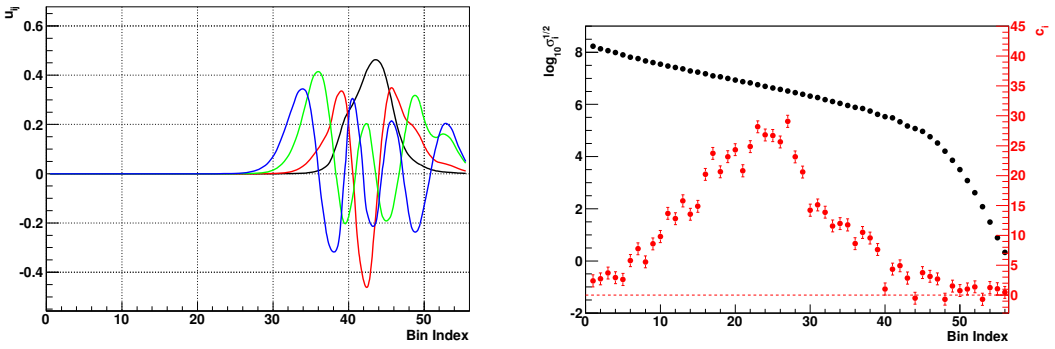

Figure 3.15 **Left:** Eigenvectors of the matrix $\mathbf{K}^T\mathbf{V}^{-1}\mathbf{K}$ corresponding to eigenvalues σ_1 (black line), σ_3 (red line), σ_5 (green line), σ_7 (blue line). A cubic spline was used to interpolate between components of each vector for visualization purposes. **Right:** Square-root of the eigenvalues (black points) and c_j coefficients (red points) of the matrix $\mathbf{K}^T\mathbf{V}^{-1}\mathbf{K}$. The example shown corresponds to a simulated power-law spectrum with 10^4 photons and $\Gamma = 2.5$.

spectra encountered are steeply falling power-laws with $\Gamma \gtrsim 2.0$. For such spectral shapes, the function given in Equation 3.52 introduces a significant bias on the unfolded solution by causing the low energy components to be oversmoothed. One method for correcting this bias is to modify the regularization term by an energy-dependent weighting for the global shape of the spectrum. It is natural to choose weighting factors in such a way that for the most probable solution the regularization term gives zero contribution. The preferred solution is estimated by the forward-folding method described in Section 3.6.1 or by simply assuming a power-law spectrum with $\Gamma = 2.5$ which is representative of an average spectrum observed.

The effect of regularization term on the regularized solution is illustrated by considering the regularization matrix $\mathbf{L}_0$. Expressed in the eigenvector basis, the

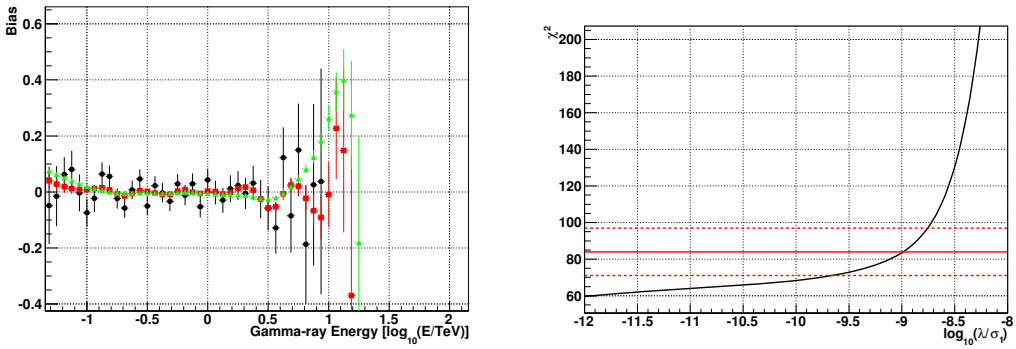

Figure 3.16 **Left:** Relative bias, $(\hat{\phi}_i - \phi_i)/\phi_i$, of the unfolded spectrum as a function of energy for three values of the regularization parameter λ/σ_1: 10^{-12} (black points), 10^{-10} (red points), 10^{-8} (green points). The example shown corresponds to a simulated exponentially cutoff power-law spectrum with 10^5 photons, $\Gamma = 2.5$, and $E_{\rm cut} = 1$ TeV. **Right:** χ^2 residual of the regularized solution as a function of regularization parameter, λ. The three red horizontal lines indicate the range of χ^2 values corresponding to $n_{ndf}, n_{ndf} \pm \sqrt{n_{ndf}}$.

regularized solution is given by

$$\hat{\boldsymbol{\phi}} = \mathbf{U}\left(\boldsymbol{\Sigma} + \lambda \mathbf{I}\right)^{-1} \mathbf{U}^T \mathbf{b} = \sum_j \frac{\sigma_j}{\sigma_j + \lambda} \frac{c_j}{\sqrt{\sigma_j}} \mathbf{u}_j, \tag{3.54}$$

where the *filter* factors, $\sigma_j/(\sigma_j + \lambda)$, are monotonically decreasing and have the effect of damping the contribution of eigenvectors with $\sigma_j < \lambda$. The regularized solution for the higher-order derivatives can be understood in a similar way when the basis vectors are chosen as eigenvectors of $\mathbf{L}^T\mathbf{L}$.

Choosing the regularization parameter, λ, is a tradeoff between the variance and bias of the solution. Setting $\lambda = 0$ results in a solution with zero bias but dominated by large variance due to the contribution of small eigenvalue terms in the eigenvector expansion. In the opposite limit, a large value of λ results in a

very smooth solution in which eigenvectors with small eigenvalues are suppressed but at the cost of significant bias. The ideal choice of regularization parameter is the one that should balance these two effects. An intuitive method for choosing the regularization parameter is based on the chi-squared-like statistical properties of the model residuals,

$$\chi^2(n_{ndf} = m - n) \simeq \left(\boldsymbol{\Upsilon}_\mathbf{e} - \mathbf{K}\hat{\boldsymbol{\phi}}\right)^T \mathbf{V}^{-1} \left(\boldsymbol{\Upsilon}_\mathbf{e} - \mathbf{K}\hat{\boldsymbol{\phi}}\right), \tag{3.55}$$

where n is assumed to be sufficient to fully describe the true spectrum and m is sufficiently small for the validity of the gaussian approximation. Figure 3.16 illustrates the unfolded spectrum for a simulated source for three values of the regularization parameter.

3.6.3 Correction Factors Method

When $\mathbf{K}$ is constructed as an n-by-n matrix and is nearly diagonal, the *correction-factors* method is an intuitive iterative technique that provides a non-parametric estimate for the true spectrum. In this method for each iteration k, a diagonal scaling matrix $\mathbf{C}_k$ is calculated,

$$C_{k,ii} = \frac{\tilde{\phi}_{k,i}}{\sum_j K_{ij}\tilde{\phi}_{k,j}}, \tag{3.56}$$

where $\tilde{\boldsymbol{\phi}}_k$ is a "smoothed" model for the true spectrum. A solution vector, $\hat{\boldsymbol{\phi}}_k$, for iteration k is evaluated as

$$\hat{\boldsymbol{\phi}}_k = \mathbf{C}_k \boldsymbol{\Upsilon}_e. \tag{3.57}$$

Since the components of $\Upsilon_{e,i}$ are not correlated, the $\hat{\phi}_k$ are statistically independent and the covariance matrix for $\hat{\boldsymbol{\phi}}_k$ is diagonal,

$$\mathbf{V}_{\phi,k} = \mathbf{C}_k \mathbf{V} \mathbf{C}_k^T. \tag{3.58}$$

To remove rapidly varying components of the solution vector $\hat{\boldsymbol{\phi}}_k$ which correspond to the eigenvectors with small eigenvalues, the solution is smoothed by fitting a parametric function (typically a power-law). The resulting smooth spectral model, $\tilde{\boldsymbol{\phi}}_{k+1}$, is then used to calculate the scaling matrix $\mathbf{C}_{k+1}$ for the next iteration. The choice of fitting function can be partially guided by the results of the *forward-folding* method. As long as $\tilde{\boldsymbol{\phi}}_0$ is a sufficiently smooth function, the procedure converges to a solution which is insensitive to the first iteration choice. Therefore a power-law function with $\Gamma = 2.5$ is adopted for $\tilde{\boldsymbol{\phi}}_0$. The refinement of the solution is continued until the chi-squared-like statistic calculated from the residual between the measurement vector and the folded flux distribution,

$$\chi^2_k = \left(\boldsymbol{\Upsilon}_e - \mathbf{K}\hat{\boldsymbol{\phi}}_k\right)^T \mathbf{V}^{-1} \left(\boldsymbol{\Upsilon}_e - \mathbf{K}\hat{\boldsymbol{\phi}}_k\right), \tag{3.59}$$

converges to a constant value, which typically occurs after 2–3 iterations.

The *correction-factors* method is not fully model-independent as the choice of smoothing algorithm can significantly influence the solution. The choice of smoothing function acts as a form of regularization by restricting the space of allowed solutions. Based on practical application of this method to spectra that can be described by a power-law with curvature, it has been found that when the smoothing function matches the true distribution, the method has minimal bias and converges rapidly to the correct solution. Even though there is no rigorous mathematical foundation for this method, its simplicity has made it a frequently favored technique for spectral reconstruction of VHE gamma-ray sources. Figure 3.17 illustrates the application of the *correction-factors* method to the reconstruction of a simulated source with a power-law spectrum with $\Gamma = 3.0$. The spectral solution is found to converge after two iterations and has a relative bias $\lesssim 1$ % across all energies. In general when the smoothing function differs from the true spectrum, the solution will tend to be biased toward the chosen

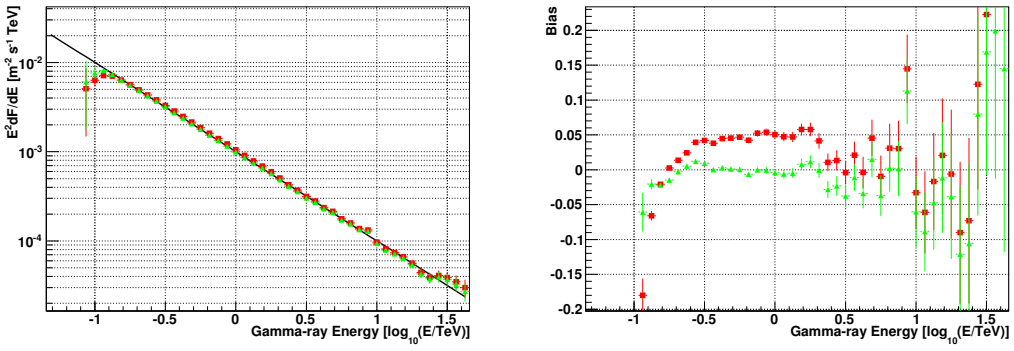

Figure 3.17 **Left:** The reconstruction of the spectrum of the simulated source with $\Gamma = 3.0$ and $F_0 = 3 \times 10^{-3}$ m^{-2} s^{-1} TeV^{-1} at $E_0 = 1$ TeV (shown as black line) with the *correction-factors* method. Starting from an initial spectral solution with $\Gamma_0 = 2.5$, the spectral solution after one (red squares) and two (green triangles) iterations is shown. **Right:** Relative bias of the flux estimates shown in the left figure.

smoothing function.

CHAPTER 4

Gamma-ray Signatures of Self-annihilating Dark Matter

WIMPs are a well-motivated generic class of particles for astrophysical DM. The self-annihilation of WIMPs in the regions of high DM density is expected to produce a gamma-ray signature with several distinctive features that carry information about both the nature of the DM particle and the DM spatial distribution. The detection of one or more of these features in a gamma-ray source would significantly aid the discrimination of the DM signal from astrophysical backgrounds and potentially allow an unambiguous identification of the WIMP. This chapter discusses the general characteristics of the gamma-ray annihilation signal in different astrophysical environments and presents the estimation of the gamma-ray flux originating from self-annihilation of WIMPs. In these calculations the greatest uncertainty in the flux prediction arises from the poorly determined DM density distribution. This distribution is not directly observable and can only be constrained by CDM simulations and stellar and gas kinematics. This chapter summarizes available data and various theoretical motivations for DM dynamics to predict the gamma-ray flux for a given source. These predictions will be confronted with observational results in Chapter 5 to constrain the viable regions of the WIMP parameter space.

4.1 DM Annihilation Signal

The differential flux of gamma-rays from WIMP self-annihilation per unit solid angle from a DM halo with a radial density profile, $\rho(r)$, is given by

$$\frac{d\phi(\boldsymbol{\psi}, E)}{dEd\Omega} = \left[\frac{\langle\sigma v\rangle}{2}\frac{dN(E, m_\chi)}{dE}\frac{1}{m_\chi^2}\right] \times \frac{1}{4\pi}\int \rho^2(s, \boldsymbol{\psi})\, ds, \tag{4.1}$$

where $\boldsymbol{\psi}$ is the line-of-sight direction, $\langle\sigma v\rangle$ is the thermally averaged product of the total self-annihilation cross section and the velocity of the WIMPs, m_χ is the WIMP mass, $dN(E, m_\chi)/dE$ is the differential gamma-ray yield per WIMP annihilation, and s is the line-of-sight distance along the direction $\boldsymbol{\psi}$. The term in square brackets depends exclusively on the WIMP physics model. The second term depends on the spatial distribution of DM along the line of sight. The density profile may depend on the WIMP physics model but is observationally constrained by astrophysical measurements.

It is customary to isolate the astrophysical factor of Equation 4.1 as,

$$\frac{dJ(\boldsymbol{\psi})}{d\Omega} = \frac{1}{4\pi}\int_0^\infty \rho^2(s, \boldsymbol{\psi})ds. \tag{4.2}$$

The finite angular resolution of IACTs is accounted for by integrating over a circular region of radius θ with solid angle $\Delta\Omega = 2\pi\,(1 - \cos\theta)$,

$$J(\boldsymbol{\psi}, \Delta\Omega) = \frac{1}{4\pi}\int_{\Delta\Omega} d\Omega \int \frac{dP(\boldsymbol{\psi}' - \boldsymbol{\psi})}{d\Omega'}d\Omega' \int_0^\infty \rho^2(s, \boldsymbol{\psi}')ds, \tag{4.3}$$

where $dP(\boldsymbol{\psi}' - \boldsymbol{\psi})/d\Omega'$ is the gamma-ray PSF of the instrument (see Section 3.4). Because the self-annihilation flux scales as the square of the dark matter density, the contribution to the observed flux is dominated by the core of the DM halo where the DM density is greatest. In the limit when the characteristic size of the source, R, is much smaller than the PSF of the instrument ($R/D \ll \theta$), the source is point-like and the value of J is given by

$$J(\boldsymbol{\psi} = \boldsymbol{\psi}_0) \simeq \frac{1}{D^2}\int_0^R \rho^2(r)r^2dr, \tag{4.4}$$

where $\boldsymbol{\psi}_0$ and D are the direction and distance to the halo center. We adopt the convention of characterizing J through a dimensionless quantity $\tilde{J} = J/(\rho_c^2 R_H)$ in which J is normalized to the product of the square of the critical density and the Hubble radius, $\rho_c^2 R_H = 3.832 \times 10^{17}$ GeV^2 cm^{-5}.

4.2 WIMP Models

The particle physics component of the WIMP annihilation flux given in Equation 4.1 is

$$\mathcal{P}(E) = \frac{\langle \sigma v \rangle}{2m_\chi^2} \frac{dN(E, m_\chi)}{dE}. \tag{4.5}$$

The natural value of $\langle \sigma v \rangle \simeq 3 \times 10^{-26}$ cm^3 s^{-1} is determined by the requirement to produce the observed DM relic abundance during the DM freeze-out process in the early universe (Kolb & Turner, 1990). For WIMPs that annihilate at the present time ($z = 0$) predominantly through s-wave processes, the thermally averaged annihilation cross section is velocity independent and therefore has this natural value. At the time of decoupling the WIMP particle was non-relativistic with $v/c \simeq 0.1$. Self-annihilation of the WIMP particle in the present universe occurs in gravitationally bound systems in which the kinetic energy is of the order of the potential energy which requires $v/c \simeq 10^{-3}$, a factor of hundred lower than during freeze-out. Coannihilations of the WIMP with the other particle species of similar mass as well as velocity-dependent terms in the annihilation cross section can modify the annihilation cross section at $z = 0$ from its natural value. The existence of coannihilation in the early universe will reduce $\langle \sigma v \rangle$ at the present day (Edsjö & Gondolo, 1997). The dependence of $\langle \sigma v \rangle$ on velocity of the WIMP, the Sommerfeld effect (Hisano et al., 2004), could potentially increase its value by $\sim$ 10–100.

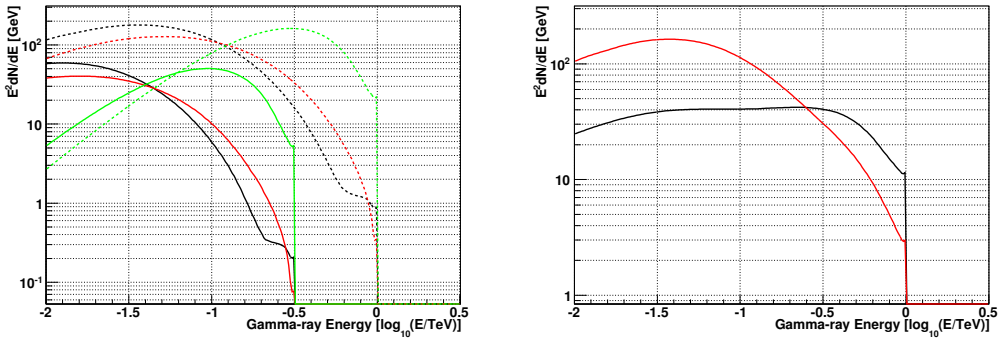

Figure 4.1 **Left:** Gamma-ray yield for a WIMP with $m_\chi = 316$ GeV (solid lines) and $m_\chi = 1$ TeV (dashed lines) annihilating through the channels $b\bar{b}$ (black lines), W^+W^- (red lines), $\tau^+\tau^-$ (green lines). Annihilation yields were calculated with the DarkSUSY package (Gondolo et al., 2004). **Right:** Comparison of the gamma-ray annihilation yield for KK (black line) and neutralino (red line) WIMPs with a mass $m_\chi = 1$ TeV. The neutralino spectrum was generated with branching ratios to $b\bar{b}$ and $\tau^+\tau^-$ of 0.9 and 0.1 respectively. Branching ratios of the KK WIMP were taken from Hooper & Profumo (2007).

The mass of the WIMP is currently constrained by accelerator measurements (Bottino et al., 2003; Feng, 2010) which will be improved during ongoing operation of LHC. In general, the low bound on the neutralino mass is particle model dependent and varies from 8–30 GeV. The upper bound on mass of the WIMP comes from unitarity limit and for a thermal relic it requires $m_\chi \lesssim 124$ TeV (Griest & Kamionkowski, 1990). The energy range over which IACT instruments are sensitive is well matched to the anticipated WIMP mass range.

The differential yield of gamma-ray photons per WIMP self-annihilation is a

sum over final-state contributions,

$$\begin{aligned}\frac{dN(E,m_\chi)}{dE} &= 2b_{\gamma\gamma}\delta\left(E-m_\chi\right) \\ &+ \sum_i b_{\gamma i}\delta\left(E-m_\chi+\frac{m_i^2}{4m_\chi}\right)+\sum_i b_i\frac{dN_i(E,m_\chi)}{dE},\end{aligned} \tag{4.6}$$

where $b_{\gamma\gamma}, b_{\gamma i}$, and b_i indicate the branching fraction into specific final-state channels. The first two terms represent annihilations into mono-energetic photons through either two or one photon channels. The last term is a sum over all channels that contribute to the continuum flux, which arises primarily from the decay of π^0 mesons produced in the hadronization of the fermion and boson final states. The differential spectrum of the π^0 decay component is relatively featureless and similar for all channels. It falls exponentially at high energies terminating at m_χ where it is enhanced by internal bremsstrahlung from charged virtual and final-state particles (Birkedal et al., 2005), resulting in an edge-like feature at $E_\gamma = m_\chi$ (see Figure 4.1). Decays into all quark and bosonic states differ only slightly in the amplitudes of the π^0 and internal bremsstrahlung components. However, decay into τ leptons generates a significantly harder spectrum, due to direct production of π^0 mesons in processes such as $\tau^\pm \to \pi^\pm\pi^0\nu$. Branching ratios to the various final states depend on the choice of a specific particle physics model for the WIMP.

In this work two specific WIMP models are considered: the lightest neutralino of SUSY (discussed in Section 1.3.3) and the Kaluza-Klein particle of UED (discussed in Section 1.3.4). The leading annihilations channels for neutralino DM (for a review see Jungman et al. (1996)) are the two-body annihilation modes to heavy fermion and boson final states: $b\bar{b}$, $t\bar{t}$, $\tau^+\tau^-$, W^+W^-, ZZ. Annihilation to light fermions is helicity suppressed by a factor $(m_f/m_\chi)^2$. The annihilation modes into mono-energetic photons, $\gamma\gamma$ and $Z\gamma$, are 1-loop processes and thus significantly suppressed (branching ratios $\sim 10^{-2}$–10^{-3}) as compared

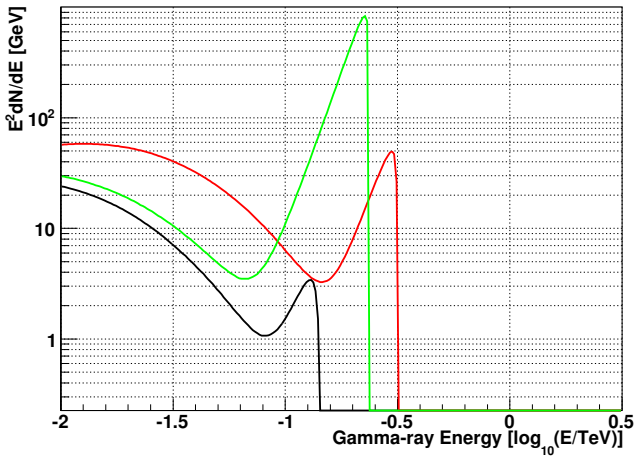

Figure 4.2 Gamma-ray spectrum of mSUGRA neutralino benchmark models I', J', J* as defined in Bringmann et al. (2009) with a significant VIB component.

to the tree-level annihilation channels contributing to the continuum component (Bergström & Ullio, 1997; Ullio & Bergström, 1998). At energies comparable to the mass of the neutralino, an additional contribution to the neutralino spectrum arises from virtual internal bremsstrahlung (VIB) (Bringmann et al., 2008). VIB together with IB processes originate from scattering of virtual and final state charged particles and results in 3-body annihilation modes. Although the phase space for 3-body annihilation modes is reduced, the helicity suppression factor is lifted for these processes. The contribution of VIB may lead to a significant enhancement in the annihilation spectrum at energies close to m_χ for specific neutralino models (see Figure 4.2). Although the strength of the VIB signal is highly model-dependent, the detection of this unique spectral feature would unambiguously distinguish the neutralino self-annihilation signal from astrophysical backgrounds.

One of the most theoretically favored candidates for the lightest Kaluza-Klein

particle (LKP) is the first KK mode of the hypercharge gauge boson $B^{(1)}$ (Cheng et al., 2002). Because the $B^{(1)}$ is a vector boson, annihilation to light fermions is not helicity suppressed and the dominant annihilation channels of the LKP are to charged lepton pairs (20% per generation). Due to the contribution of IB associated with charged lepton production, the LKP spectrum is significantly enhanced at high energies (Bergström et al., 2005). As illustrated in Figure 4.1, the LKP annihilation spectrum is considerably increased near the endpoint as compared to the neutralino of the same mass. The total annihilation cross section is related to the mass by $\langle \sigma v \rangle \simeq 3 \times 10^{-26} \left(0.8 \text{ TeV}/m_{B^{(1)}}\right)^2 \text{ cm}^3 \text{ s}^{-1}$ (Servant & Tait, 2003) which constrains the mass to the range 500–800 GeV.

4.3 Spherically Averaged DM Density Profile

The density profile of a DM halo is determined by a number of astrophysical processes such as the initial gravitational relaxation of DM, interaction of DM with baryonic matter, and potentially the weak interactions of WIMPs with themselves and other particles. High resolution N-body simulations that model the hierarchical formation of CDM halos through gravitational interactions have been a highly successful method for studying the properties of DM halos. These simulations have shown that the spherically-averaged (smoothed) DM distribution in DM halos is well described by a universal halo profile that is independent of halo virial mass, the mass within the virial radius defined by

$$m_{vir} = 4\pi \int_0^{r_{vir}} \rho(r) r^2 dr = 200 \rho_c \frac{4\pi}{3} r_{vir}^3. \tag{4.7}$$

A widely adopted parameterization for the DM halo density is the Navarro, Frenk, & White (NFW) profile (Navarro et al., 1997),

$$\rho(r) = \rho_s \left(\frac{r}{r_s}\right)^{-1} \left(1 + \frac{r}{r_s}\right)^{-2}, \tag{4.8}$$

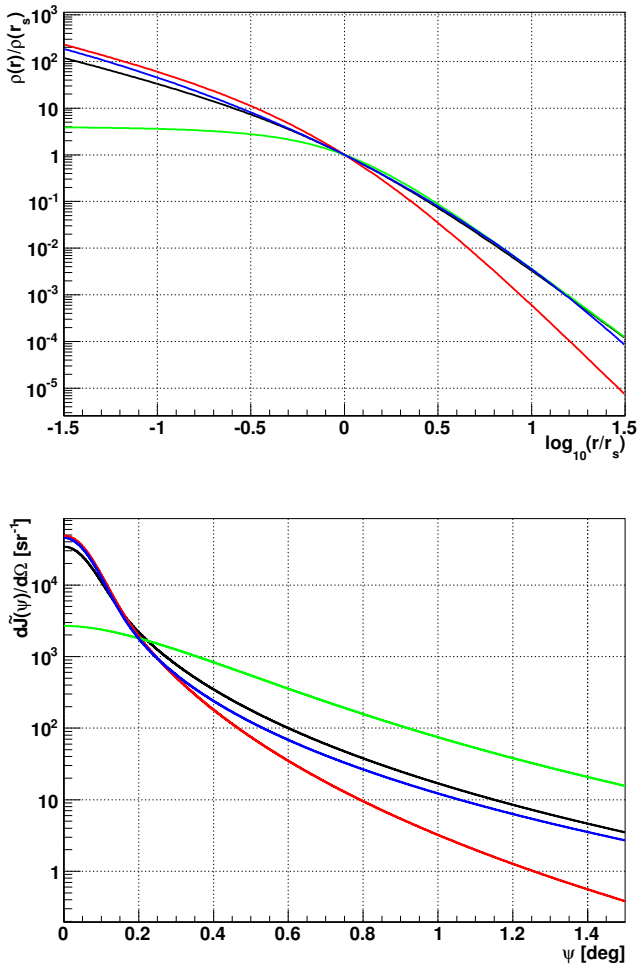

Figure 4.3 **Top:** Comparison of the radial density normalized to the density at the scale radius of the NFW (black), Hernquist (red), Burkert (green), and Einasto (blue) profiles. **Bottom:** Line-of-sight integral (J) normalized to the total gamma-ray luminosity as a function of the angle ψ from the center of the halo shown for the four density profiles in the top figure. The calculation assumes that a halo is placed at a distance $D = 100r_s$ from the observer and the PSF is gaussian with an RMS of 0.05 deg.

where r_s is the scale radius and ρ_s is the characteristic density. For $r \ll r_s$, the NFW profile has a central power-law *cusp* with $\rho(r) \propto r^{-1}$, and at large radii ($r \gg r_s$) it declines as $\rho(r) \propto r^{-3}$. The line-of-sight integral J is primarily sensitive to the behavior of the density profile in the cusp region ($r < r_s$). However CDM simulations currently have a limited capability to model the distribution of DM on these scales due to numerical resolution effects. More recent computations have found that DM halos can be better fit with the Einasto profile (Navarro et al., 2004; Graham et al., 2006; Navarro et al., 2010),

$$\rho(r) = \rho_s \exp\left[-\frac{2}{\alpha}\left(\left(\frac{r}{r_s}\right)^{\alpha} - 1\right)\right] \tag{4.9}$$

with $\alpha \simeq 0.17$. This profile is characterized by an inner slope ($\gamma(r) = -d\ln\rho(r)/d\ln r$) that asymptotically approaches zero toward the center producing a finite central density at $r = 0$. Figure 4.3 illustrates that over intermediate scales ($r \sim r_s$) the NFW and Einasto profiles are similar and therefore for a distant DM halo ($D/r_s \gtrsim 100$) they produce nearly identical gamma-ray luminosity profiles. Because all of the sources considered in this work are distant, the NFW profile is adopted for all subsequent calculations of the gamma-ray luminosity. For the purpose of modeling the gravitational potential (Section 4.6.1), the Hernquist profile (Hernquist, 1990),

$$\rho(r) = \rho_s \left(\frac{r}{r_s}\right)^{-1} \left(1 + \frac{r}{r_s}\right)^{-3}, \tag{4.10}$$

is also considered which has the same asymptotic behavior at small radii ($r \ll r_s$) as the NFW profile and therefore results in a similar gamma-ray luminosity profile when observed at large distances. These two profiles differ significantly, however, for computations of DM halo masses.

Observations of low surface brightness (LSB) galaxies indicate inner slopes that are significantly shallower than one (de Blok et al., 2001; de Blok, 2005),

which motivated the empirical cored Burkert density profile (Burkert, 1995)

$$\rho(r) = \rho_s \left(1 + \frac{r}{r_s}\right)^{-1} \left(1 + \left(\frac{r}{r_s}\right)^2\right)^{-1} . \tag{4.11}$$

The Burkert profile generally provides poor fits to the profiles of simulated halos (Merritt et al., 2006). The observed discrepancy between simulations and observations may be indicative of processes that have modified the distribution of DM in the central regions of LSB galaxies such as gravitational interactions between baryons and DM or DM self-interactions. Figure 4.3 shows that the Burkert DM density profile results in a gamma-ray emission profile that is significantly more extended than that predicted for the NFW halo. The applicability of the theoretically predicted CDM density profiles which assume only gravitational interactions of DM is perhaps best satisfied in the dSph systems. The baryonic mass in these galaxies is a negligible perturbation to the DM potential even in the central regions ($r \ll r_s$) and the pair interaction of stars indicate collisional relaxation times significantly larger than the Hubble time.

The density profiles of simulated DM halos are commonly characterized by their virial mass m_{vir} and concentration $c = r_{vir}/r_s$ which are related to ρ_s and r_s (Equation 4.7). Using a sample of simulated DM halos with masses 10^{11}–10^{14} h^{-1} $M_\odot$, Bullock et al. (2001) found that the median halo concentration at $z = 0$ is correlated with virial mass and can be well approximated by the expression,

$$c = 9 \left(\frac{m_{vir}}{1.5 \times 10^{13} h^{-1} M_\odot}\right)^{-0.13} , \tag{4.12}$$

with a scatter of $\Delta \log c \simeq 0.14$.

4.4 DM Density Fluctuations Boost

A generic prediction of CDM simulations is that the DM density profile is not smooth but enriched with density fluctuations, substructures, with characteristic spatial scales smaller than r_s. These substructures may significantly enhance the DM annihilation flux as compared to that predicted for a smooth halo. Numerical simulations find that these substructures are gravitationally isolated and can be well described by a power-law mass function $\mathrm{dN/dM} \propto \mathrm{M}^{-\alpha}$ with $\alpha \simeq 1.9$–2.0 (Diemand et al., 2006; Springel et al., 2008a) at $z = 0$. The substructure mass spectrum extends to a minimum halo mass, m_0, which is set by the free streaming and collisional damping length scales of the WIMP in the early universe. For example, a neutralino WIMP with mass $m_\chi = 100$ GeV is predicted to have $m_0 \simeq 10^{-6}\ \mathrm{M}_\odot$ (Green et al., 2005). The abundance of these substructures at $z = 0$ depends on the fraction that survives tidal disruption during the hierarchical merger and accretion processes.

The contribution of DM substructures to the gamma-ray flux is quantified by scaling the line-of-sight integral over the smooth halo distribution, J_s, by a boost factor B such that $J = J_s\,(1 + B)$. CDM simulations can set a lower limit on the boost factor by summing the annihilation luminosity from numerically resolved substructures. High resolution simulations of Milky Way-mass halos ($M \simeq 10^{12} M_\odot$) have shown a factor of two enhancement ($B \simeq 1$) to the annihilation luminosity within the virial radius from resolved substructures ($M_{sub} \gtrsim 10^6\ M_\odot$) (Diemand et al., 2007, 2008; Springel et al., 2008b). The contribution of unresolved substructures could significantly increase the boost factor. However, numerical and analytical studies have shown that the boost factor is sensitive to the extrapolation of the mass function to the cutoff mass scale, m_0, as well as the assumed concentration-mass relation for small halo masses. For

example a substructure mass function with $\alpha = 2.0$ and a mass-concentration relationship of the form of Equation 4.12 results in a gamma-ray luminosity per decade of substructure mass that rises with decreasing mass thus making the exact value of m_0 critical to the determination of the boost factor. Strigari et al. (2007) obtain an upper bound on the boost factor of $B \simeq 100$ by using the mass-concentration relationship for field halos from Equation 4.12 and extrapolating the substructure mass function to $m_0 \simeq 10^{-5}$ $M_\odot$ with $\alpha = 1.9$. A more detailed calculation by Martinez et al. (2009) that considered different parameterizations for the substructure mass-concentration relation as well as the tendency of tidal effects to diminish the gamma-ray luminosity of substructures found boost factors in the range $1 \lesssim B \lesssim 10$.

4.5 Baryonic Effects

The gravitational influence of baryonic matter during the hierarchical formation of a DM halo is expected to significantly affect the DM distribution in the regions where mass density of baryons is comparable or larger than the DM density, for example the centers of galactic nuclei or globular clusters. Unlike DM, baryons can effectively dissipate their energy through radiative processes and baryon-baryon interactions and thus concentrate in the core of the DM halo. During this contraction process and subsequent star formation, the baryons will tend to modify the smooth density profiles predicted by CDM-only simulations as well as the abundance and structural properties of DM substructures. The importance of these effects is highly dependent on the evolutionary history of a DM halo and could alternatively enhance or diminish the annihilation signal.

The condensation of baryons in the halo center gravitationally compresses the DM distribution on large scales (comparable to r_s) leading to an enhancement

of the central DM density. The adiabatic compression effect was first modeled analytically using adiabatic invariants by Blumenthal et al. (1986). In addition to compressing the distribution of DM, baryons can also have the effect of heating the central DM distribution through gas outflows driven by supernova feedback (Mashchenko et al., 2006a) and dynamical friction from infalling gas clumps (El-Zant et al., 2001, 2004). These processes have the ultimate effect of diminishing the central DM density. The role of baryons in the evolution of DM halos has been recently studied with simulations combining dissipationless DM particles with a baryonic component composed of gas and stars (Gnedin et al., 2004; Gustafsson et al., 2006; Scannapieco et al., 2009). A consistent finding in these simulations is that the contraction of baryons significantly increases the central concentration of the DM halo and produces an approximately isothermal DM cusp with $\gamma \simeq 2.0$ with some evidence for flattening on small scales (much smaller than r_s) (Romano-Díaz et al., 2008, 2009; Tissera et al., 2010). The presence of a baryonic component has also been found to significantly reduce the survival probability of DM substructures (Romano-Díaz et al., 2010).

In the centers of galactic nuclei where collisional effects occurring on the two-body relaxation timescale are important, the DM halo could be further altered by the presence of a central black hole or high stellar densities. The adiabatic compression of DM in the core of a halo through the slow growth of a central black hole has been suggested as a mechanism for increasing the flux from DM self-annihilation (Gondolo & Silk, 1999). However, the magnitude of this effect depends strongly on the ratio of the initial and final masses of the black hole, its initial alignment with the center of the DM halo, and the merging history of the galactic nucleus (Ullio et al., 2001). Merritt & Cruz (2001) have shown that a typical merger event between black holes of comparable mass destroys cuspy density profiles. The effect of gravitational scattering of DM particles by

infalling baryons, stars and gas, in the central regions of galactic nuclei may also be significant. The transfer of momentum to the dark matter component in these interactions should lead to the partial evaporation of DM from the center of the galaxy. The ejection of DM particles through the gravitational slingshot process in the vicinity of binaries will further enhance the DM outflow from the centers of galactic nuclei. In general the prediction of the gamma-ray flux from DM self-annihilation in the astrophysical environments where the interaction of DM with baryons is important is not well determined due to strong dependence on initial conditions and the history of the sources.

4.6 DM Density Profile Modeling

Studying the the distribution of stellar positions and velocities in an astrophysical system is a well-established method for inferring the properties of the underlying gravitational potential and the mass distribution from which it originates. In the case of the dSphs, the gravitational potential is dominated by DM and such an analysis can therefore provide strong constraints on the distribution of DM in these systems. These constraints can be used to derive bounds on the line-of-sight integral, J, and thus the expected DM gamma-ray annihilation flux from these objects. It is customary to describe the dynamics of a stellar system by its distribution function (DF), $f(\mathbf{x}, \mathbf{v}, t)$, which is the probability to find a star in the infinitesimal phase space element centered at $(\mathbf{x}, \mathbf{v})$ at the time t. In the regime where stellar collisions are negligible, which is applicable to the dSphs, the time-evolution of the DF is governed by the collisionless boltzmann equation,

$$\frac{\partial f}{\partial t} + \mathbf{v}\frac{\partial f}{\partial \mathbf{x}} + \frac{\partial \psi}{\partial \mathbf{x}}\frac{\partial f}{\partial \mathbf{v}} = 0, \tag{4.13}$$

where ψ is the negative gravitational potential ($\psi(r) \geq 0$) satisfying Poisson's equation, $\nabla^2\psi = -4\pi G\rho$. According to Jeans' theorem (Binney & Tremaine, 1987), a steady-state solution of the collisionless boltzmann equation ($\partial f/\partial t = 0$) can only depend on the phase-space coordinates through integrals of motion of individual stars. In a spherically symmetric system, the integrals of motion are the binding energy per unit mass, $E = \psi(r) - v^2/2$, and the length of the angular momentum vector per unit mass, $L = |\mathbf{L}|$, and therefore an arbitrary $f(E, L)$ represents a general solution of Equation 4.13.

Observational constraints on the dSph systems allow only a subset of the phase space coordinates to be measured for each star: the projected distance, R, from the dSph center and line-of-sight velocity, v_z. The observed distribution of positions and velocities can be used to construct a dynamical model for the dSph which is a function of a set of free parameters, $\boldsymbol{\theta}_\psi$, of the gravitational potential. Two parameterizations for the DM potential for which the corresponding density profiles were given in Section 4.3 are the Hernquist potential,

$$\psi(r) = \psi_0 \frac{1}{1 + r/r_s}, \tag{4.14}$$

where $\psi_0 = 2\pi G\rho_s r_s^2$ and the NFW potential,

$$\psi(r) = \psi_0 \frac{\ln(1 + r/r_s)}{r/r_s}, \tag{4.15}$$

where $\psi_0 = 4\pi G\rho_s r_s^2$. Because these parameterizations for the potential have only two free parameters, it is convenient to define a dimensionless unit system in which the potential scale radius, r_s, and potential amplitude at the origin, ψ_0, are set to one.

A technique for modeling the gravitational potential that has been extensively studied in the context of dSphs (Łokas, 2002; Łokas et al., 2005; Mashchenko et al., 2006b; Strigari et al., 2007, 2008b) is to compare the moments of the velocity

distribution in bins of projected radius with the solutions of the two lowest order Jean's equations for a spherically symmetric system (Binney & Tremaine, 1987). This system of equations is not closed and requires as an input a model for the stellar velocity anisotropy parameter, $\beta(r) = 1 - \sigma_{||}^2(r)/\sigma_{\perp}^2(r)$, that characterizes the relative velocity dispersions along the radial and tangential directions. A significant disadvantage of this method is that the data must be binned (assuming large statistics) and information about the velocity distribution is necessarily reduced in this process. This approach can also result in unphysical DF solutions in some regions of phase space.

An alternative approach for modeling the gravitational potential is to derive the line-of-sight velocity distribution (LOSVD), $f(R, v_z; \boldsymbol{\theta}_\psi)$, which is the p.d.f. to detect a star at a projected distance R with line-of-sight velocity v_z. The LOSVD is obtained by a marginalization of the six-dimensional DF into the two-dimensional space of the observables in the presence of the spherical symmetry. A significant advantage of this method is that it operates on unbinned data and is therefore well-suited for small data samples. The method does not escape from the inherent uncertainties associated with the unknown distribution of individual stars in the (E, L) parameter space. However, it allows systematic exploration of the effects of these distributions on the parameters of the gravitational potential. Section 4.6.1 outlines a method for calculating $f(R, v_z; \boldsymbol{\theta}_\psi)$ through integration of orbits and ergodization. A method for solving for the parameters of the DM potential from the stellar velocity data set using standard likelihood statistics is then presented in Section 4.6.2. The application of these methods to the stellar velocity data sets for five dSphs observed by VERITAS is presented in Chapter 5.

4.6.1 Orbit Modeling

A model for the LOSVD of a stellar system can be constructed from a superposition of single-orbit distributions with fixed E and L. Using the unit system defined in terms of the two free parameters of the gravitational potential (r_s and ψ_0), all physical quantities are unitless, and the binding energy and angular momentum are measured in units of ψ_0 and $\psi_0^{1/2} r_s$ respectively and are restricted to the ranges $[0, 1]$ and $[0, \infty]$. The orbit of a star in a spherically symmetric potential is determined by four integrals of motion: the binding energy E and the three components of the angular momentum vector, $\mathbf{L}$. The vector $\mathbf{n} = \mathbf{L}/|\mathbf{L}|$ defines the orbital plane in which the star travels. The trajectory of motion in polar coordinates ρ and ϕ is given by

$$\begin{aligned} \dot{\phi} &= \frac{L}{\rho^2}, \\ \dot{\rho} &= \pm\sqrt{2\left(\psi(\rho) - E\right) - \frac{L^2}{\rho^2}} = \pm v_\rho(\rho, E, L). \end{aligned} \tag{4.16}$$

For a gravitationally bound star, the motion of the star occurs between an inner radius $\rho_{\min}$ (pericenter) and an outer radius $\rho_{\max}$ (apocenter) which are the points along the orbit at which $\dot{\rho} = 0$. The travel time between the inner and outer radii is

$$\Upsilon\left(E, L\right) = \int_{\rho_{\min}}^{\rho_{\max}} \frac{d\rho}{v_\rho(\rho, E, L)}. \tag{4.17}$$

Figure 4.4 illustrates the value of the radial travel time for bound orbits in the (E, L) plane. At each binding energy, the angular momentum of bound orbits is constrained to be less than $L_{max}(E)$, the angular momentum of a circular orbit ($\rho_{min} = \rho_{max}$). Contours of constant orbital apocenter (pericenter) distance correspond to approximately vertical (horizontal) lines in the (E, L) plane.

The six-dimensional phase space distribution of a single star traveling in the

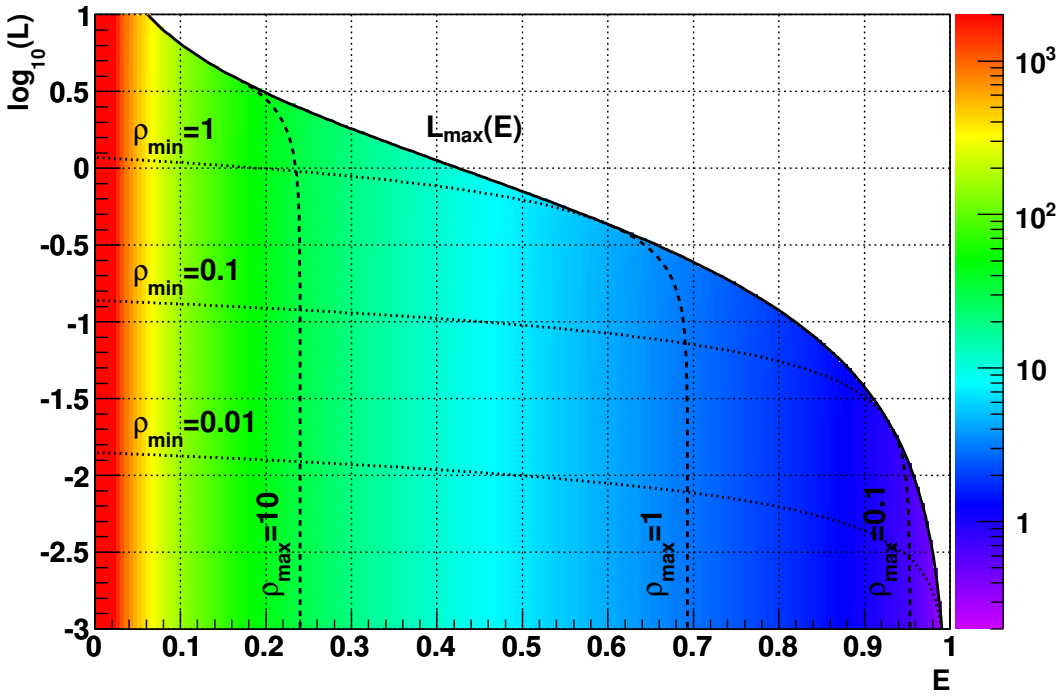

Figure 4.4 Radial travel time of orbits in the NFW potential as a function of binding energy and angular momentum. Dashed (dotted) lines indicate isocontours of apocenter (pericenter) distance. Shown as a solid curve is the function $L_{max}(E)$, which is the angular momentum of a circular orbit with binding energy E.

spherical potential is

$$f(\mathbf{x}, \mathbf{v}, t; E, L) = \delta(\mathbf{x} - \mathbf{x}(t; E, L))\delta(\mathbf{v} - \mathbf{v}(t; E, L)) \tag{4.18}$$

where the position and velocity of the star as a function of time, $\mathbf{x}(t; E, L)$ and $\mathbf{v}(t; E, L)$, are determined by integrating the equations of motion (Equation 4.16). The p.d.f. as a function of time for R and v_z is obtained by marginalizing Equation 4.18 over the unknown orbital parameters: the orientation of the orbital plane $\mathbf{n}$ and the initial orbital phase ϕ_0. To obtain the time-independent p.d.f for R and v_z, an ergodization is performed in which the probability to find a star at a given point along the trajectory is weighted by the relative time dt/Υ the star spends in a given region of the parameter phase space. The p.d.f. of the star in the observables R and v_z as derived in Vassiliev & Wood (2010) is

$$\begin{aligned} &f_{R^2,v_z}(R, v_z; E, L) = \frac{1}{4\pi\Upsilon(E, L)} \\ &\left[\int_{D(R,v_z,E,L)} d\rho F(\rho, R, v_z, E, L) + \int_{D(R,-v_z,E,L)} d\rho F(\rho, R, -v_z, E, L)\right], \end{aligned} \tag{4.19}$$

where the subscript on f denotes that the model is a p.d.f. in R^2 and v_z and the function F is defined as

$$\begin{aligned} &F(\rho, R, v_z, E, L) = \\ &\frac{1}{\rho\sqrt{\rho^2 - R^2}} v_\rho(\rho, E, L)^{-1} \left[\frac{R^2L^2}{\rho^4} - \left(v_z - \frac{\sqrt{\rho^2 - R^2}}{\rho} v_\rho(\rho, E, L)\right)^2\right]^{-1/2} \end{aligned} \tag{4.20}$$

and the integration domain $D(R, v_z, E, L)$ satisfies the following set of inequalities,

$$D(R, v_z, E, L) = \begin{cases} \left|v_z - \dfrac{\sqrt{\rho^2 - R^2}}{\rho} v_\rho(\rho, E, L)\right| \leq \dfrac{RL}{\rho^2} & \\ R \leq \rho \leq \rho_{max}(E, L) & \text{if } R > \rho_{min}(E, L) \\ \rho_{min}(E, L) \leq \rho \leq \rho_{max}(E, L) & \text{if } R < \rho_{min}(E, L) \end{cases}. \tag{4.21}$$

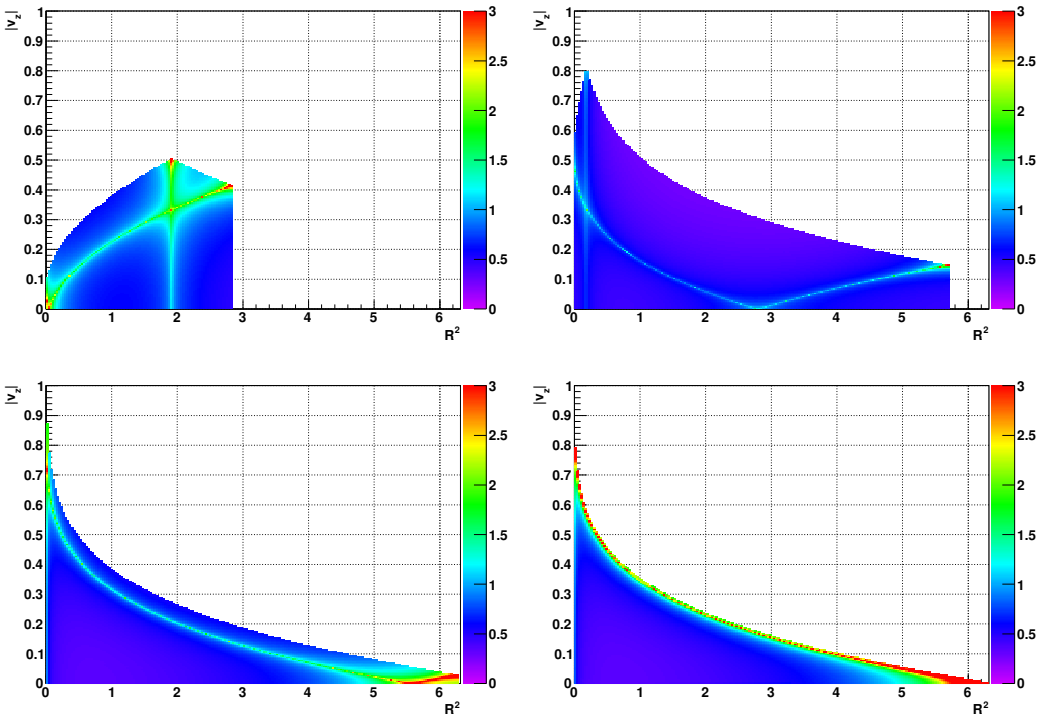

Figure 4.5 LOSVD, $f_{R^2,v_z}(R, v_z)$, for orbits in the NFW potential with $E = 0.5$ and $L/L_{max}(E)$ equal to 0.99 (**upper left**), 0.50 (**upper right**), 0.10 (**lower left**), and 0.01 (**lower right**).

Figure 4.5 illustrates the LOSVD for different orbits with fixed binding energy and different values of angular momentum encompassing orbits from nearly circular to nearly radial. These distributions are characterized by two caustic structures with one over square-root singularities.

The LOSVD for the ensemble of stars in a dSph is determined by a final marginalization of the single-star LOSVD given in Equation 4.19 over the density of stars in (E, L) space, $N(E, L)$. The $N(E, L)$ of a stellar system is determined by a number factors including the initial conditions of its formation, its assembly history, and in the case of the dSphs their interaction with the tidal field of the

Milky Way. For collisionless systems such as the dSphs, $N(E, L)$ remains constant in the absence of significant merger events or ongoing star formation. However, interactions with the external gravitational potential of the Milky Way can slowly affect $N(E, L)$ through the stripping of stars with small binding energies and tidal heating effects. Although in principle any arbitrary distribution in (E, L) space is possible, the distribution of the gas from which the stars originally formed is expected to produce a relatively flat $N(E, L)$ distribution with no characteristic scales other than characteristic scales of the potential itself. A simple model for the $N(E, L)$ is one in which all orbital energies with apocenter distances less than a tidal radius r_t are equally probable,

$$N(E,L) = N_0 \begin{cases} L_{max}(E)^{-1} & \rho_{max}(E,L) < r_t \\ 0 & \rho_{max}(E,L) > r_t \end{cases}, \tag{4.22}$$

and N_0 is a normalization coefficient defined so that $N(E, L)$ satisfies

$$\int_0^1 \int_0^{L_{max}(E)} N(E,L) dE dL = 1. \tag{4.23}$$

It is the goal of this study to show that small variations in $N(E, L)$ do not lead to large variations in the parameters of the gravitational potential. Once $N(E, L)$ is chosen the p.d.f. in (R, v_z) space is determined by

$$f_{R^2,v_z}(R, v_z) = \int_0^1 \int_0^{L_{max}(E)} N(E,L) f_{R^2,v_z}(R, v_z; E, L) dL dE, \tag{4.24}$$

and expressed in a scale invariant form it is

$$\mathcal{F}(R, v_z) = 2R^2 |v_z| f_{R^2,v_z}(R, v_z). \tag{4.25}$$

Figure 4.6 illustrates the scale-invariant LOSVD calculated for the NFW and Hernquist potentials with the energy distribution given in Equation 4.22. The figure shows distributions for the systems with $r_t \gg r_s$ in which case the LOSVD is universal and independent of parameters of the gravitational potential ψ_0 and

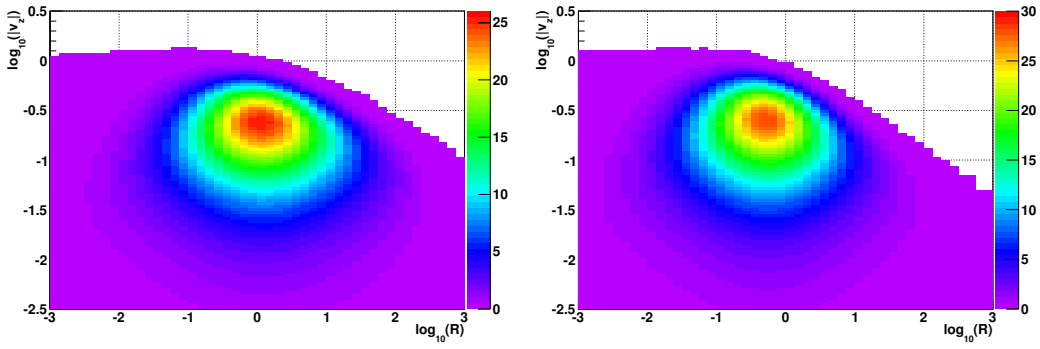

Figure 4.6 Scale invariant LOSVD, $\mathcal{F}(R, |v_z|)$, of the NFW (**left**) and Hernquist (**right**) potentials.

r_s. In more realistic scenarios when r_t is of order r_s this universality will be broken.

4.6.2 Likelihood Computation

The goal of the DM density profile modeling is to calculate constraints on the parameters of the gravitational potential $\boldsymbol{\theta}_\psi = \{\psi_0, r_s\}$ from the spatial distribution and velocities of stars. A stellar velocity data set consists of N stars each with a set of measurements $D_i = \{R_i, v_{z,i}, \sigma_{z,i}\}$ corresponding to the projected distance R and a line-of-sight velocity v_z with associated velocity measurement error σ_z. The velocity measurement error modifies the intrinsic LOSVD as

$$\tilde{\mathcal{F}}(R, v_z, \sigma_z; \boldsymbol{\theta}_\mathcal{F}) = |v_z| \int \frac{dv'_z}{v'_z} \mathcal{F}(R, v'_z; \boldsymbol{\theta}_\mathcal{F}) \frac{1}{\sqrt{2\pi}\sigma_z} \exp\left[\frac{-(v_z - v'_z)^2}{2\sigma_z^2}\right], \quad (4.26)$$

where $\boldsymbol{\theta}_\mathcal{F}$ indicates free parameters of the LOSVD not associated with the gravitational potential (e.g. the tidal radius r_t). The function $\tilde{\mathcal{F}}(R, v_z, \sigma_z; \boldsymbol{\theta}_\mathcal{F})$ is universal and once computed can be used to analyze any data set by scaling its arguments by the parameters of the potential, r_s and $\sqrt{\psi_0}$.

The log likelihood function for the data as a function of the parameters $\boldsymbol{\theta}_\psi$ is represented in terms of the scale-invariant modified LOSVD as

$$\ln L(D_1, \ldots, D_N | \boldsymbol{\theta}_\psi = \{r_s, \psi_0\}, \boldsymbol{\theta}_\mathcal{F}) = \sum_{i=1}^{N} \tilde{\mathcal{F}} \left(\frac{R_i}{r_s}, \frac{v_{z,i}}{\sqrt{\psi_0}}, \frac{\sigma_{z,i}}{\sqrt{\psi_0}}; \boldsymbol{\theta}_\mathcal{F} \right), \qquad (4.27)$$

where the physical parameters $\boldsymbol{\theta}_\mathcal{F}$ are also scaled by the parameters of the gravitational potential. In general maximizing the log likelihood function is a non-linear optimization problem which is computed in the following discussions using numerical techniques.

4.7 Review of Observational Targets

Because the gamma-ray signature of the WIMP is proportional to the square of the local density, the spatial scales that contribute to the total gamma-ray flux from a DM halo are much smaller than the spatial scales contributing to the halo mass. In some astrophysical objects such as dSphs, the density of DM on these small spatial scales is determined by the formation and evolution history of the DM halos and to a significantly lesser degree by the dynamics of the interaction of DM with baryonic matter. In other systems such as galactic nuclei and globular clusters, the evolution of DM on these small spatial scales is typically driven by its interaction with baryonic matter which dominates the gravitational potential. The influence of baryons in these systems in the form of dense stellar populations, molecular clouds, and central black holes could potentially lead to a much higher central DM concentration than that inferred from the large-scale DM distribution and thus substantially enhance the annihilation signal. Therefore, it is attractive to consider sources for observation that represent a diverse set of astrophysical environments that could boost the gamma-ray luminosity.

Table 4.1. Summary of the observational properties of the five observed dSphs.

Name	α [J2000.0]	δ [J2000.0]	$L_V[\mathrm{L}_\odot]$	r_h [pc]	Distance [kpc]	Ref.
Draco	$17^h20^m14.4^s$	$57°54'54''$	$2.7 \pm 0.4 \times 10^5$	221 ± 16	76 ± 5	1,2
Ursa Minor	$15^h08^m41.1^s$	$67°12'36''$	$2.0 \pm 0.9 \times 10^5$	150 ± 18	66 ± 3	3
Bootes I	$14^h00^m03.6^s$	$14°30'42''$	$3.0 \pm 0.6 \times 10^4$	242^{+22}_{-20}	62 ± 3	2,4
Willman 1	$10^h49^m22.3^s$	$51°03'04''$	1000^{+660}_{-670}	25^{+5}_{-6}	38 ± 7	1,5
Segue 1	$10^h07^m03.2^s$	$16°04'25''$	335^{+235}_{-185}	29^{+8}_{-5}	23 ± 2	1,6

References. — (1) Martin et al. (2008); (2) Bonanos et al. (2004); (3) Walker et al. (2009); (4) Dall'Ora et al. (2006); (5) Willman et al. (2005); (6) Belokurov et al. (2007)

4.7.1 Dwarf Spheroidal Galaxies

The dSph galaxies of the Milky Way represent one of the most attractive target classes for indirect DM searches due to their proximity and high DM content. Because the gravitational potential of these systems is dominated by DM rather than baryons, studies of their stellar kinematics can be used to set relatively robust constraints on the value of the line-of-sight integral (J) over DM distribution (see Section 4.6). Furthermore the absence of any gas or ongoing star formation in the majority of these systems reduces the likelihood for confusion with gamma-ray emission from standard astrophysical processes. With the addition of systems discovered by the Sloan Digital Sky Survey (SDSS), the number of known dSph has recently grown to more than 20 (Tolstoy et al., 2009). The majority of these newly discovered systems fall in the class of ultra-faint dSphs with extremely low luminosities. Five dwarf galaxy systems were selected for observa-

tion by VERITAS. The observational properties of these systems are summarized in Table 4.1.

The Draco dSph is one of the most frequently studied objects for indirect DM detection (Baltz et al., 2000; Tyler, 2002; Evans et al., 2004; Sánchez-Conde et al., 2007; Strigari et al., 2007, 2008b; Bringmann et al., 2009). It has an approximately spherically symmetric stellar distribution (Irwin & Hatzidimitriou, 1995) with total luminosity of the order of 10^5 $L_\odot$ (Piatek et al., 2002). The large spectroscopic data set available for this object (Wilkinson et al., 2004; Muñoz et al., 2005; Walker et al., 2007) provides the best constraints on its DM distribution profile relative to the other dSphs. Draco is consistent with an old low-metallicity ([Fe/H] $= -1.8 \pm 0.2$) stellar population with no significant star formation over the last 2 Gyrs (Aparicio et al., 2001). Draco previously has been observed at VHE energies by the STACEE observatory (Driscoll et al., 2008), the Whipple 10m telescope (Wood et al., 2008), and the MAGIC telescope (Albert et al., 2008).

The Ursa Minor dSph has a distance and inferred DM content similar to those of Draco. There is no evidence of young or intermediate age stellar populations in Ursa Minor (Shetrone et al., 2001). Photometric studies of this object have found evidence for significant structures in the stellar distribution in the central 10' (Bellazzini et al., 2002; Kleyna et al., 2003) and an extratidal stellar population (Palma et al., 2003). These unusual morphological characteristics could be evidence of possible tidal interaction with the Milky Way, velocity projection effects along the line-of-sight, or the presence of fluctuations in the DM induced gravitational potential (Kleyna et al., 2003). Ursa Minor was previously studied at VHE energies by the Whipple 10m telescope (Wood et al., 2008).

The recently discovered dSph Bootes I (Belokurov et al., 2006) shows evidence

for elongation of the stellar profile. N-Body simulations can not reproduce the observed velocity dispersion without a dominant contribution from DM. In addition, modeling of the tidal interaction effects between Bootes I and the Milky Way do not provide an adequate explanation for the elongation of this system suggesting a non-spherically symmetric distribution of DM in the Bootes progenitor (Fellhauer et al., 2008). The estimates of the age of the stellar population and metallicity suggest similarity with the old and metal-poor ([Fe/H] ~ -2.3) stellar distribution of M92 (Belokurov et al., 2006; Muñoz et al., 2006; Martin et al., 2007). VHE observations for this object are reported in this dissertaion for the first time and published in Acciari et al. (2010).

Willman 1 and Segue 1 are two of the faintest and least luminous dSph systems known and belong to the new class of ultra-faint dSphs recently discovered by the SDSS (Willman et al., 2005; Belokurov et al., 2007). The half-light radii ($r_h \sim 25$ pc) and total luminosities ($L_V \lesssim 10^3$ $L_\odot$) of these two galaxies place them in a region of parameter space overlapping with globular clusters (Belokurov et al., 2007). Classification of these objects as dark-matter dominated galaxies is primarily based on their large observed velocity dispersions ($\sigma \simeq 4$ km s^{-1}), low metallicities ([Fe/H] < -2), and significant metallicity spread (~ 0.5 dex).

Due to its small mean velocity ($v \simeq -14$ km s^{-1}), kinematic analysis of Willman 1 is complicated by contamination with foreground Milky Way stars. An unusual velocity distribution as well as an apparent extended morphology indicate that Willman 1 may be tidally disrupted (Willman et al., 2010). However the possibility of foreground contamination and small size of the stellar velocity data set prevent a definitive conclusion regarding tidal effects. The low metallicity of this system ([Fe/H] ~ -2.1) is consistent with the observed trend of decreasing metallicity for fainter dSphs (Siegel et al., 2008). VHE observations of Willman

1 were previously reported by the MAGIC collaboration (Aliu et al., 2009).

As compared to Willman 1, the identification of Segue 1 as a DM-dominated dSph and the measurement of its kinematic and morphological properties is more certain due to a larger mean velocity ($v \simeq 206$ km s^{-1}) relative to the foreground Milky Way stars. Because it spatially overlaps with the Sagittarius stream, Belokurov et al. (2007) initially argued that Segue 1 was an extended globular cluster that had been formerly associated with the Sagittarius dSph. More recent analyses of stellar kinematics and metallicities have indicated stronger support for the hypothesis that Segue 1 is a DM-dominated dSph (Geha et al., 2009; Simon et al., 2010). Niederste-Ostholt et al. (2009) found evidence for the existence of an extended morphological structure, potentially tidal debris, within one degree by applying an optimal filter analysis to the SDSS photometric data. Simon et al. (2010) argue that these structures are not associated with Segue 1 but with the Sagittarius stream.

4.7.2 Local Group Galaxies

M32 is the closest compact elliptical galaxy and may have formed in a merging event between M31 and a low-luminosity spiral galaxy (Bekki et al., 2001) in which the disk component of M32 was tidally stripped. Stellar kinematic data strongly support the presence of a single supermassive compact object in the center of the galaxy with a mass of 2–4 $\times 10^6$ M$_\odot$ (Joseph et al., 2001). The core of M32 has a relatively homogeneous stellar population with an intermediate age of approximately 4 Gyr (Corbin et al., 2001; del Burgo et al., 2001). Lauer et al. (1998) estimate M32's core relaxation time scale to be 2–3 Gyr. Collisional two-body relaxation of a stellar population around a black hole is analytically predicted to result in a steady-state power-law stellar density profile with power-

law index between 3/2 and 7/4 (Bahcall & Wolf, 1976). Optical and infrared data indicate a stellar density profile compatible with a power-law index in the range 1.4–1.9 at the resolution limit of 0.07 pc (Corbin et al., 2001; Lauer et al., 1998). The condensation of baryons in galactic nuclei gravitationally compresses DM halos. It is generically known that in a merger between two galaxies a massive black hole binary could be formed. The coalesence of the comparable mass black holes is predicted to deplete the central density by evacuating stars and destroying any potential DM cusp in the galaxy core (Milosavljević et al., 2002). Even if such an event occurred in M32, its short core relaxation time is sufficient for the reformation of a dense stellar core in the nucleus of this galaxy. Therefore the stellar density in the core of M32, in excess of 10^7 $M_\odot$ pc^{-3} and the highest known among nearby systems (Lauer et al., 1998), makes it a promising candidate for the detection of DM annihilation.

By observing astrophysical systems capable of rapid evolution, one may be able to overcome dynamical limitations on the WIMP annihilation rate, if it is limited by the scattering of WIMPs into a very small annihilation region in the galactic nucleus. M33 is remarkable for the small relaxation time, ∼3 Myr, in its stellar nucleus of approximately 0.2 pc, which results from the high stellar density, 5×10^6 $M_\odot$ pc^{-3}, and extremely low velocity dispersion, 21 km s^{-1}, in this region (Lauer et al., 1998). M33 is a low-luminosity, DM-dominated, bulgeless spiral galaxy with a dark halo mass of approximately 5.1×10^{11} $M_\odot$ (Corbelli & Salucci, 2000). The mass of the black hole in its center is less than 1.5×10^3 $M_\odot$ (Gebhardt et al., 2001; Merritt et al., 2001). The stellar population in the nucleus of M33 can be modeled by two bursts of star formation 2 and 0.5 Gyr ago suggesting the possibility of a merger in the last ∼Gyr. However, due to its rapid collisional relaxation time, M33 could have developed a core-collapsed nucleus in the period since the last merging event. Though the effect of a merger

Table 4.2. Summary of the observational properties of the three observed globular clusters. The columns labeled r_c and r_h denote the core and half-mass radii respectively.

Name	α [J2000.0]	δ [J2000.0]	L_V [$L_\odot$]	r_c [pc]	r_h [pc]	Distance [kpc]	Ref.
M15	$21^h29^m58.4^s$	$12°10'01''$	4.0×10^5	0.2	3.2	10.3 ± 0.4	1,2,3
M13	$16^h41^m41.5^s$	$36°27'37''$	2.6×10^5	1.7	3.3	7.7	3
M5	$15^h18^m33.8^s$	$02°04'58''$	2.9×10^5	0.9	4.6	7.5	3

References. — (1) van den Bosch et al. (2006); (2) Dull et al. (1997); (3) Harris (1996)

on the DM distribution in a galactic nucleus may depend on the ratio of the masses of stellar populations in the cores of the merging galaxies and on the ratio of the initial and final masses of the stars in the nucleus, the uniquely fast relaxation time of this galaxy make it a favorable object for observations.

4.7.3 Globular Clusters

Although there is no observational evidence for the presence of significant DM in globular clusters, the association of globular clusters and DM halos fits naturally into the standard paradigm of hierarchical structure formation. In the primordial formation scenario proposed by Peebles (1984), globular clusters are formed in DM overdensities in the early universe and may therefore retain a significant fraction of this primordial halo in the current epoch. Given that the extremely dense stellar cores of globular clusters dominate the gravitational potential of these systems, the observable effects of an extended DM halo may be minimal. Moore (1996) argued that the presence of tidal tails in some globular clusters

suggests that globular clusters are not embedded in DM halos. Recent simulations (Mashchenko & Sills, 2005a,b; Saitoh et al., 2006) have challenged this picture, showing that an extended halo may be compatible with the observable properties of globular clusters, although much of the original halo mass could be stripped by tidal interactions with the host galaxy. If a DM halo is present in globular clusters, its central density could have been increased by several orders of magnitude through the gravitational compression caused by the core collapse of the stellar population. The observational properties of the three core-collapsed globular clusters with high central stellar densities that were selected for observation by VERITAS are summarized in Table 4.2.

The proximity and potentially high central DM density of M15 makes this source particularly favorable for indirect DM searches. With a core radius of $\sim$0.2 pc and extreme central density in excess of 10^7 $M_\odot$ pc^{-3} (Dull et al., 1997), M15 is the prototype for the core-collapsed globular cluster. During core collapse, the globular cluster is predicted to relax through stellar two-body collisions to a power-law density profile that extends down to the smallest observable scales (Binney & Tremaine, 1987). If M15 was originally embedded in a DM halo, this evolutionary process must significantly compress the central DM distribution and dramatically enhance the gamma-ray flux. However, the poorly understood process of kinetic heating of DM in the core of the cluster by stars and hard binaries could lead to a depletion of DM from this region. Quantitative evaluation of these effects allows for large variations in the predicted gamma-ray flux. In addition, astrophysical gamma-ray background fluxes may exist in the the central regions of globular clusters due to the presence of the dense populations of the milli-second pulsars (Bednarek & Sitarek, 2007). The Tucanae 47 globular cluster which was detected recently by the Fermi satellite in the high-energy gamma-ray regime (Abdo et al., 2009b) is the source compatible with this model.

CHAPTER 5

Results

This chapter presents the data analysis of ten targets observed by VERITAS to search for the annihilation signature of WIMPs. Section 5.1 describes the data sets and data-quality selection criteria for the chosen targets (Section 4.7). Data analysis was performed using several Monte Carlo data sets that were generated to model the VERITAS observatory performance characteristics (Section 5.2) during the different periods in which the observations were taken. Section 5.3 presents the analysis of the data for each target under the hypothesis of a gamma-ray point source with a power-law energy distribution. This analysis is used to derive both integral and differential (energy-dependent) constraints on the gamma-ray fluxes.

The data analysis is further specialized to determine gamma-ray upper limits using a model for the spectral and morphological features of the WIMP annihilation signature discussed in Chapter 4. Section 5.4 describes the constraints on the line-of-sight integral over the DM distribution for the five observed dSph systems as derived from the published stellar kinematics data with the use of the orbit modeling methodology (Section 4.6.1). Upper limits on the gamma-ray flux from WIMP annihilations in each target are then presented in Section 5.5. The constraints on the allowed parameter space of WIMP models are obtained from the analysis of the data sets of the dSphs are presented in Section 5.6.

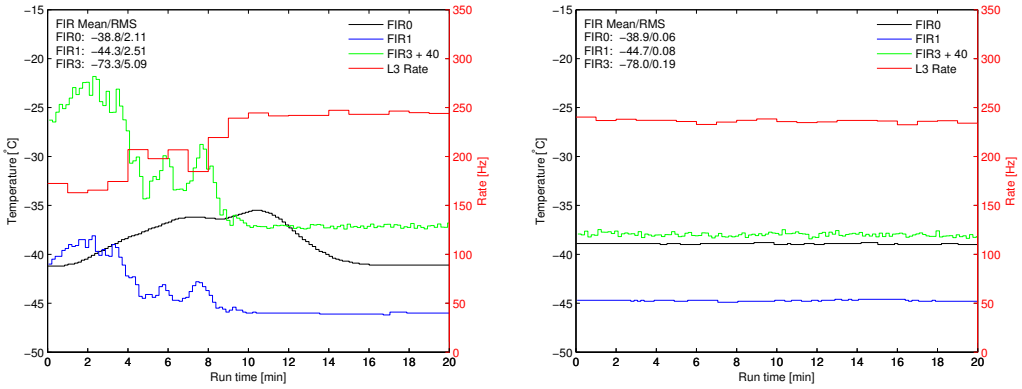

Figure 5.1 Sky temperature measured by FIR0 (black), FIR1 (blue) and FIR3 (green) and L3 trigger rate (red) as a function of time for two runs from the Segue 1 data set: 49739 (**left**) and 49923 (**right**). The run in the left panel is representative of a run excluded on the basis of poor weather conditions.

5.1 Data

The data presented in this thesis were taken from 2007 to 2010. Table 5.1 summarizes the observation epoch and total exposure time for each data set. During the period of observations, the VERITAS instrument underwent two significant modifications: a transition from 3- to 4-telescope operations in April 2007 and change of the observatory configuration due to the relocation of telescope T1 in Summer 2009. All observations were taken on clear moonless nights with the full telescope array (three telescope prior to Apr 2007 and four afterwards). Each data set is comprised of a set of discrete exposures, *runs*, that are generally 20 minutes long and taken while the array tracks a fixed position in right ascension and declination. The observing strategy used for all observations is the *wobble* technique with an offset of 0.5° (Section 3.5).

A set of data-quality selection criteria was applied to each data set to remove

Table 5.1. Summary of the observation period, total observation time, and quality-selected observation time for each source.

Name	Observation Period	Exposure [hr]	Quality-Selected Exposure [hr]	Array Configuration
Draco	2007 Apr-Mar	23.8	18.1	a,b
Ursa Minor	2007 Feb-May	24.6	18.2	a,b
Bootes I	2009 Apr-May	15.7	14.4	b
Willman 1	2007 Dec-2008 Feb	15.5	13.1	b
Segue 1	2009 Dec-2010 Mar	36.0	24.6	c
M5	2009 Feb-Mar	15.7	10.0	b
M13	2007 May-Jul	8.2	6.7	a
	2010 May-Jul	11.2	9.4	c
M15	2010 Jun	6.9	6.9	c
M32	2008 Oct-2009 Nov	13.3	11.9	b
M33	2007 Nov-2008 Feb	14.8	12.4	b

Note. — (a) Three telescope (T1/T2/T3) array in pre-Summer 2009 geometrical layout. (b) Four telescope array in pre-Summer 2009 geometrical layout. (c) Four telescope array in post-Summer 2009 geometrical layout.

observations affected by poor weather conditions and hardware-related problems. The total exposure after data-quality selection is given in Table 5.1. The two primary criteria for the data-quality selection were the RMS temperature variations measured by the far-infrared radiometers (FIRs) and the stability of the L3 trigger rate.

The FIR system consists of a set of three far-infrared radiometers: a telescope-mounted radiometer sensitive to 8–14 μm (FIR1), a static radiometer sensitive to 8–14 μm (FIR0; installed Sep 2008), and a telescope-mounted radiometer sensitive to 9.6–11.5 μm (FIR3; installed Sep 2008). The two telescope-mounted radiometers are both aligned with the optical axis of the array while the static radiometer points to a fixed position near zenith. The FIRs continuously record the mean sky temperature averaged in their respective FoV (2.7 deg for FIR1 and FIR3 and 6 deg for FIR0) every 10 seconds. Variations in the FIR temperature are sensitive to changes in atmospheric conditions such as the passage of clouds through the VERITAS FoV. The RMS temperature measured by FIR0/FIR1 and FIR3 were required to be less than 0.3° C and 0.7° C respectively. Figure 5.1 shows an example comparison of the measured FIR temperature as a function of time for runs passing and failing the data-quality selection criteria.

The L3 trigger rate provides a complementary data-quality diagnostic. With the trigger settings in effect since Jan 2007, the L3 trigger rates under normal observing conditions are 200–250 Hz (150–180 Hz) for four (three) telescope operation. An abnormally low or variable trigger rate can indicate poor weather as well as problems with the trigger or data-acquisition hardware. To derive the data selection criteria for each run, events were binned in 1 minute intervals and fit with a constant data rate. The reduced chi-squared of this fit is required to be less than two to pass data selection. Generally changes in the FIR temperature

are found to correlate well with changes in the L3 trigger rate (see Figure 5.1). For data to be selected for further data analysis both stability of FIR temperature and L3 rate were required over the duration of the run.

5.2 Detector Simulation

Simulations of gamma-ray showers provide a critical input to the *ChiLA* analysis chain and are used to discriminate between gamma-ray and cosmic-ray events (Section 3.2.3), estimate gamma-ray energy (Section 3.2.4), and generate an instrument response model (IRM; Section 3.4). The gamma-ray simulations used for the analysis presented in this thesis were computed with the *ChiLA* simulation chain which consists of three main components: the CORSIKA cosmic-ray air shower package (Heck et al., 1998), an optical ray-tracing package (VSOptics) (Fegan & Vassiliev, 2005), and a detector electronics simulation (VSElectronics). CORSIKA is a publicly available Monte Carlo code[1] that simulates extensive air showers initiated by high-energy cosmic-rays and gamma-rays. A CORSIKA extension module (Bernlohr, 2000) computes the Cherenkov light emitted by charged shower secondaries. The latter two components of the simulation chain are specific to VERITAS and were developed in conjunction with the *ChiLA* analysis package.

Simulation data sets were derived from a single library of gamma-ray air showers generated with CORSIKA version 6.502 and the atmospheric profile corresponding to the US Standard Atmosphere 1976 (US76). Gamma-ray energies were sampled at a set of discrete values spaced equidistantly in logarithmic energy between 31.6 GeV and 100 TeV with 16 energy bins per decade. Shower directions were sampled at eight zenith angles ($0°, 12°, 19°, 26°, 34°, 41°, 49°, 56°$) and

[1] http://www-ik.fzk.de/corsika/

four azimuth angles ($0°, 90°, 180°, 270°$). All atmospheric cascades were computed with the use of the geomagnetic field at the location of the VERITAS observatory in Tucson, AZ, USA. Raytracing at each pointing was performed for eight offset angles (ψ) between the primary photon direction and the optical axis of the array ($0° - 1.75°$ in steps of $0.25°$). A model of the VERITAS optical system (OS) was created by starting from an ideal OS and adding random dispersions to the focal length, position, spotsize, and misalignment angle of individual mirrors (see Table 5.2 for the list of parameters used). The dispersions in the first three parameters were measured during the characterization of the VERITAS mirrors and telescopes. The last parameter, distribution of misalignment angles, was tuned so that the simulated PSF matched the average measured PSF of the VERITAS telescopes after the introduction of the new mirror alignment technique (McCann et al., 2010) which was applied to all telescopes prior to the 2009–2010 observing season.

Three simulation data sets (A,B, and C) were generated to characterize the configuration of VERITAS during three time periods spanned by the observations: Jan 2007 – Jul 2008 (A), Sep 2008 – Jul 2009 (B), and Sep 2009 – Jul 2010 (C). The first two data sets (A and B) were simulated with the configuration of array of VERITAS telescopes prior to Summer 2009. The third data set (C) was simulated with the the array layout after T1 was moved to a new position in Summer 2009. Each data set was simulated with a different average PMT gain (which determines DC/PE conversion factor) and set of telescope throughput scaling factors. The parameters chosen for each data set are summarized in Table 5.3. The absolute PMT gain was estimated from the photostatistics analysis of laser flashes (Section 3.1.2). A single value of DC/PE was chosen for each time period that matched the measured average of all telescopes (see Figure 5.2). As evident from Figure 5.2 significant variations of $\sim$20% in the absolute gain

occurred during the period of the observations due to both the aging of the PMTs as well as changes to the high-voltage settings. The telescope throughput factor was used to correct for differences in the light collection yield of each telescope. A throughput factor of one is assigned to a telescope that has a PMT quantum efficiency, mirror reflectivity, and lightcone efficiency corresponding to a set of canonical values that were established by direct measurement. The images produced by the individual muons in the atmosphere can be used as a calibrated source of Cherenkov light. A set of relative throughput scaling factors was estimated from the analysis of muon images using the methodology described in Fegan & Vassiliev (2007). Figure 5.2 shows the throughput scaling factor as a function of time derived with this technique for each telescope relative to T3.

5.3 Point-Source Analysis

Each data set was analyzed under the hypothesis of a gamma-ray point source with a power-law energy spectrum. For the detection of a weak source, VERITAS sensitivity comes mostly from the relatively small range of energies within which a VHE gamma-ray source can be well modeled with these spectral characteristics. Two sets of gamma-ray selection analysis cuts, *Standard* and *Soft*, optimized for the detection of a source with spectral index $\Gamma = 2.5$ and $\Gamma = 3.5$ respectively (see Section 3.3) were applied to the data. The maximum likelihood method (Section 3.5.4) was used to analyze the residual counts distribution and evaluate the significance of a gamma-ray source at the nominal position of each target. The spatial counts model for each data set was constructed using the IRM and the gamma-ray spectrum for which the analysis cuts were optimized. Gamma-ray rates, gamma-ray rate upper limits, and significances obtained with the maximum likelihood analysis are summarized in Table 5.4. No significant

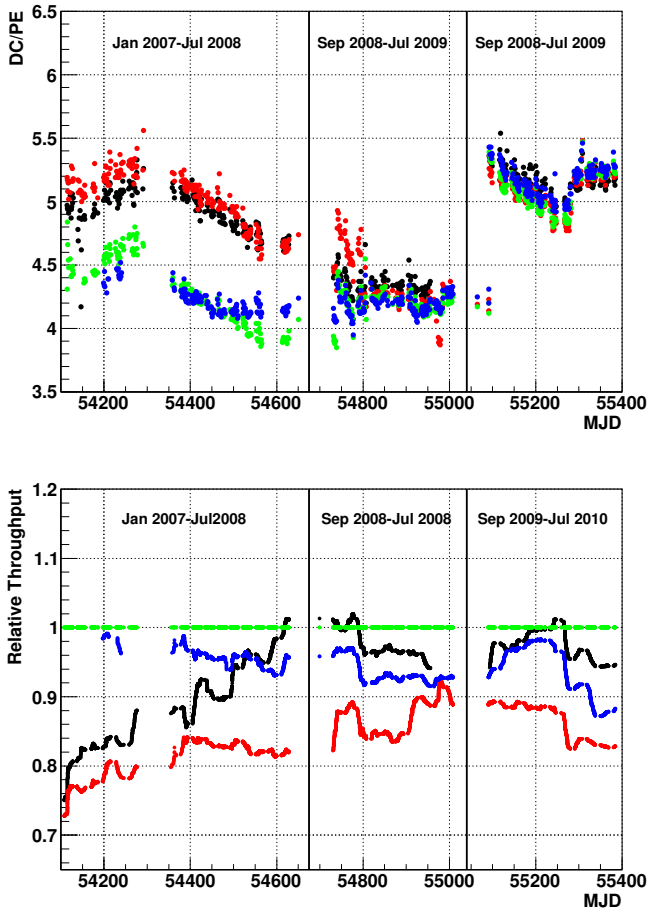

Figure 5.2 **Left:** Median DC/PE of T1 (black), T2 (red), T3 (green), and T4 (blue) as a function of MJD estimated from nightly laser runs using the photostatistics method over the period 2007–2010. Vertical lines indicate the three time periods for which separate simulation data sets were generated. **Right:** Moving average over four days of the scaling throughput factor derived from muon analysis and relative to T3 over the period 2007–2010. The correlated change of the scaling throughput factors is caused by the recoating of mirrors on the T3 telescope. The steady growth of the throughput factor of T1 in the data set A is also due to mirror replacement process occurring during this time period.

Table 5.2. Parameters used to generate the model of the VERITAS optical system. The FWHM and 68% containment diameter (θ_{68}) of this model for a simulated point-source at infinity and two field angles (ψ) is given.

Parameter	Value
Mirror Focal Length [cm]	1200
Mirror Focal Length Dispersion [cm]	8.6
Mirror Tangential Alignment Dispersion [cm]	0.55
Mirror Normal Position Dispersion [cm]	1.0
Mirror Spot Size (90% Diameter) [cm]	0.51
Mirror Spot Size Dispersion [cm]	0.2
Simulated PSF Spotsize	
θ_{FWHM} ($\psi = 0°$) [deg]	0.061
θ_{68} ($\psi = 0°$) [deg]	0.076
θ_{FWHM} ($\psi = 1°$) [deg]	0.104
θ_{68} ($\psi = 1°$) [deg]	0.120

Table 5.3. Absolute gain and telescope throughput scaling factors used to generate each simulation data set.

			Telescope Throughput Scaling			
Data Set	Epoch	DC/PE	T1	T2	T3	T4
A	Jan 2007 - Jul 2008	4.7	0.9	0.9	1.0	0.95
B	Sep 2008 - Jul 2009	4.3	0.97	0.88	1.0	0.95
C	Sep 2009 - Jul 2010	5.3	0.95	0.9	1.0	0.95

Table 5.4. Summary of gamma-ray rates, gamma-ray rate upper limits, and significances for the *Standard* and *Soft* cuts analyses.

Name	*Standard* Cuts			*Soft* Cuts		
	R[a] [min^{-1}]	$R_{\mathrm{u.l.}}$[b] [min^{-1}]	S[c] [σ]	R[a] [min^{-1}]	$R_{\mathrm{u.l.}}$[b] [min^{-1}]	S[c] [σ]
Draco	-0.010 ± 0.012	<0.017	-0.86	-0.043 ± 0.026	<0.030	-1.63
Ursa Minor	-0.006 ± 0.010	<0.017	-0.56	-0.072 ± 0.024	<0.019	-2.88
Bootes I	-0.009 ± 0.011	<0.017	-0.76	-0.060 ± 0.024	<0.022	-2.34
Willman 1	0.029 ± 0.019	<0.061	1.65	0.076 ± 0.039	<0.140	2.02
Segue 1	-0.000 ± 0.012	<0.024	-0.03	-0.025 ± 0.030	<0.045	-0.82
M5	-0.009 ± 0.009	<0.012	-0.91	-0.059 ± 0.022	<0.019	-2.43
M13	-0.025 ± 0.016	<0.019	-1.48	-0.077 ± 0.038	<0.039	-1.98
M15	0.030 ± 0.026	<0.074	1.21	0.009 ± 0.056	<0.116	0.17
M32	0.001 ± 0.017	<0.035	0.05	0.006 ± 0.038	<0.079	0.15
M33	-0.019 ± 0.015	<0.019	-1.23	-0.011 ± 0.037	<0.065	-0.31

[a]Gamma-ray rate.

[b]Gamma-ray rate 95% C.L. Upper Limit.

[c]Statistical significance.

Table 5.5. Summary of energy thresholds and upper limits on the gamma-ray spectral energy density obtained with the *Standard* and *Soft* cuts integral analyses. A power-law energy distribution with Γ of 2.5 and 3.5 was used for the calculation of the energy threshold and flux upper limit of the *Standard* and *Soft* cuts analyses respectively.

Name	*Standard* Cuts ($\Gamma = 2.5$)		*Soft* Cuts ($\Gamma = 3.5$)	
	E_{th}[a] [GeV]	E^2dF/dE[b] [erg m^{-2} s^{-1}]	E_{th}[a] [GeV]	F_{th}[b] [erg m^{-2} s^{-1}]
Draco	390	$< 2.5 \times 10^{-9}$	215	$< 6.4 \times 10^{-9}$
Ursa Minor	518	$< 3.0 \times 10^{-9}$	281	$< 4.8 \times 10^{-9}$
Bootes I	296	$< 1.9 \times 10^{-9}$	170	$< 3.2 \times 10^{-9}$
Willman 1	316	$< 7.4 \times 10^{-9}$	175	$< 2.6 \times 10^{-8}$
Segue 1	255	$< 2.2 \times 10^{-9}$	145	$< 5.3 \times 10^{-9}$
M5	373	$< 1.4 \times 10^{-9}$	211	$< 2.7 \times 10^{-9}$
M13	249	$< 2.0 \times 10^{-9}$	137	$< 5.8 \times 10^{-9}$
M15	275	$< 6.8 \times 10^{-9}$	155	$< 1.4 \times 10^{-8}$
M32	306	$< 4.5 \times 10^{-9}$	169	$< 1.5 \times 10^{-8}$
M33	309	$< 2.4 \times 10^{-9}$	163	$< 1.3 \times 10^{-8}$

[a]Energy at peak of the differential detection rate for the corresponding spectral model with power-law index Γ.

[b]95% C.L. spectral energy density (E^2dF/dE) upper limit at E_{th}.

gamma-ray emission consistent with the point-source hypothesis was detected. To search for the presence of gamma-ray sources in each $\sim 3^\circ$ observation field and to test the robustness of the point-source analysis, two-dimensional sky maps of point-source significance as a function of position in celestial coordinates were calculated (see Figures 5.3–5.5). In all cases the distribution of significances was compatible with the null hypothesis.

Upper limits on the spectral energy density of each source were derived from the limits on the integral gamma-ray rate detected with the maximum likelihood analysis. Table 5.5 summarizes the energy-independent upper limits on the spectral energy density derived assuming a power-law energy spectrum. Limits are given at energy thresholds for each set of the analysis cuts (E_{th}) which are defined to be the peaks of the differential detection rate of the corresponding spectral model. The *Soft* cuts analysis achieves an energy threshold that is 100–200 GeV lower than the *Standard* cuts analysis because it is optimized for the detection of a source with $\Gamma = 3.5$. Differences in energy threshold among the sources is primarily attributable to the differences in the average elevation of the observations. To a lesser degree these differences are also attributable to the configuration of the hardware such as PMT gains.

A set of differential (energy-dependent) flux limits were derived for each data set using the correction factor method (Section 3.6) and an energy bin size $\Delta \log_{10} E = 0.25$. Although this method has several deficiencies when used to analyze a strong gamma-ray source, it is convienient to use for determining the flux upper limits for the non-correlated energy bins. Furthermore because the energy bin size is significantly larger than the VERITAS energy resolution ($\Delta \log_{10} E \simeq 0.07$), the limits derived with the regularized unfolding method do not differ significantly from those derived with the correction factors method.

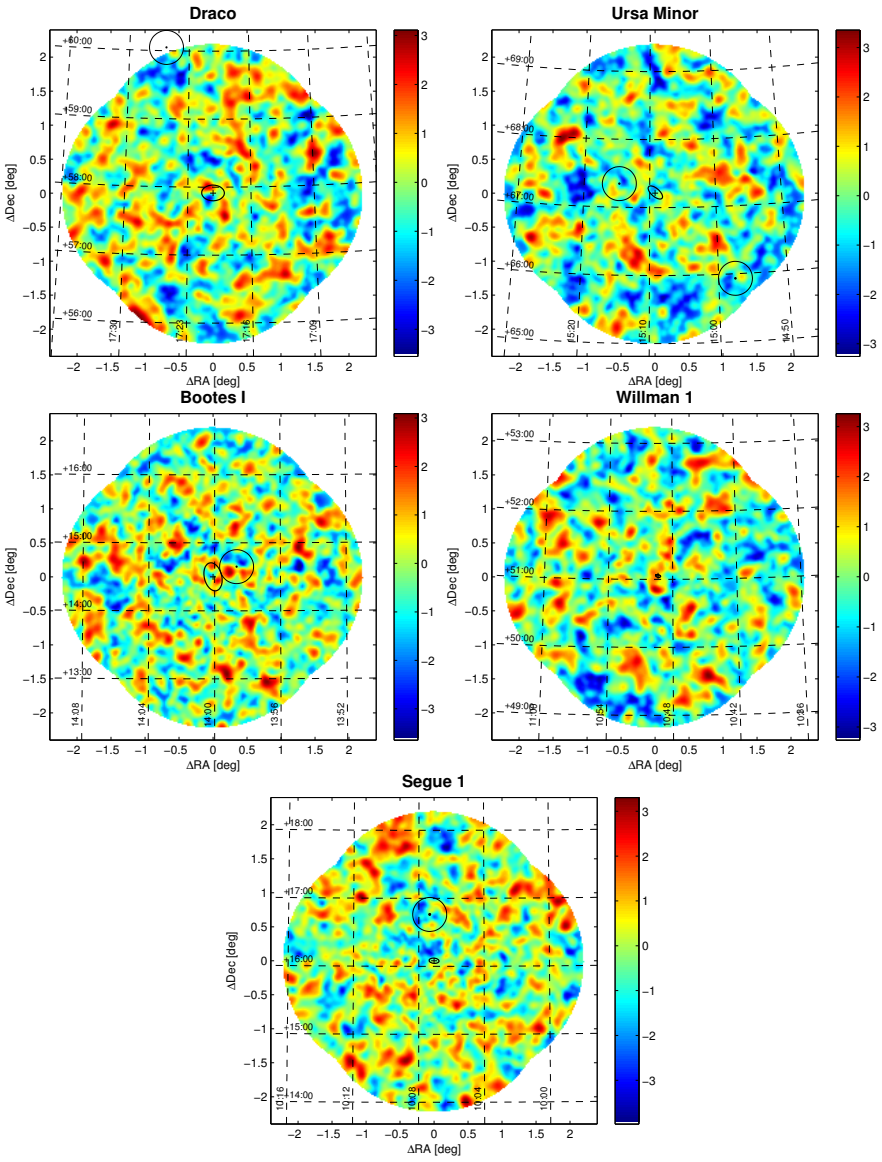

Figure 5.3 Significance map in right ascension and declination obtained with the *Standard* cuts analysis of the region around each each of the observed dSphs. The center of each source is designated by a black cross. Thin solid lines indicate the circular regions in the vicinity of bright stars ($m_V < 6$) that were excluded from background modeling. Thick black elliptical contours of constant surface brightness correspond to the half-light radius of each dSph given in Table 4.1.

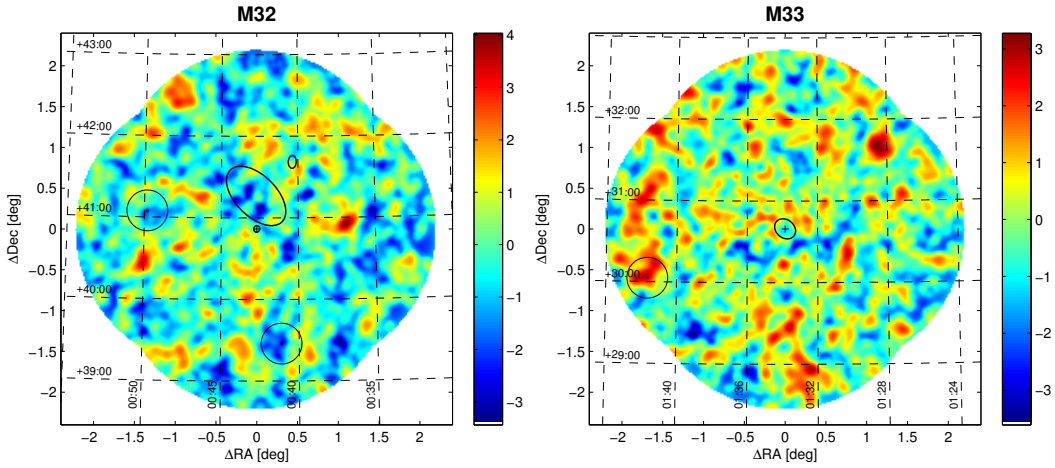

Figure 5.4 Significance map in right ascension and declination obtained with the *Standard* cuts analysis of the region around M32 and M33. The center of each source is designated by a black cross. Thin solid lines indicate the circular regions in the vicinity of bright stars ($m_V < 6$) that were excluded from background modeling. Thick black elliptical contours indicate isophotes of constant K-band surface brightness for M32, M31, and NGC 205 (**left**) and M33 (**right**) from Jarrett et al. (2003).

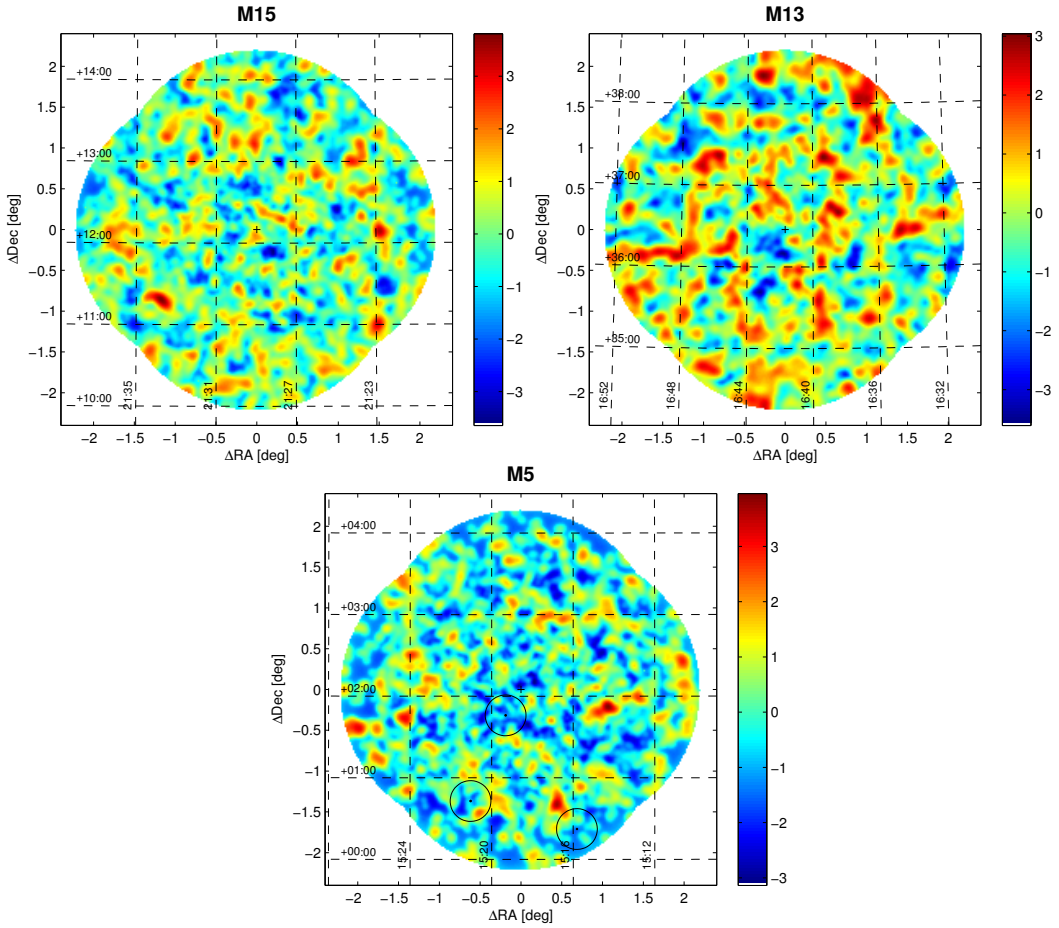

Figure 5.5 Significance map in right ascension and declination obtained with the *Standard* cuts analysis of the region around each each of the observed globular clusters. The center of each source is designated by a black cross. Thin solid lines indicate the circular regions in the vicinity of bright stars ($m_V < 6$) that were excluded from background modeling.

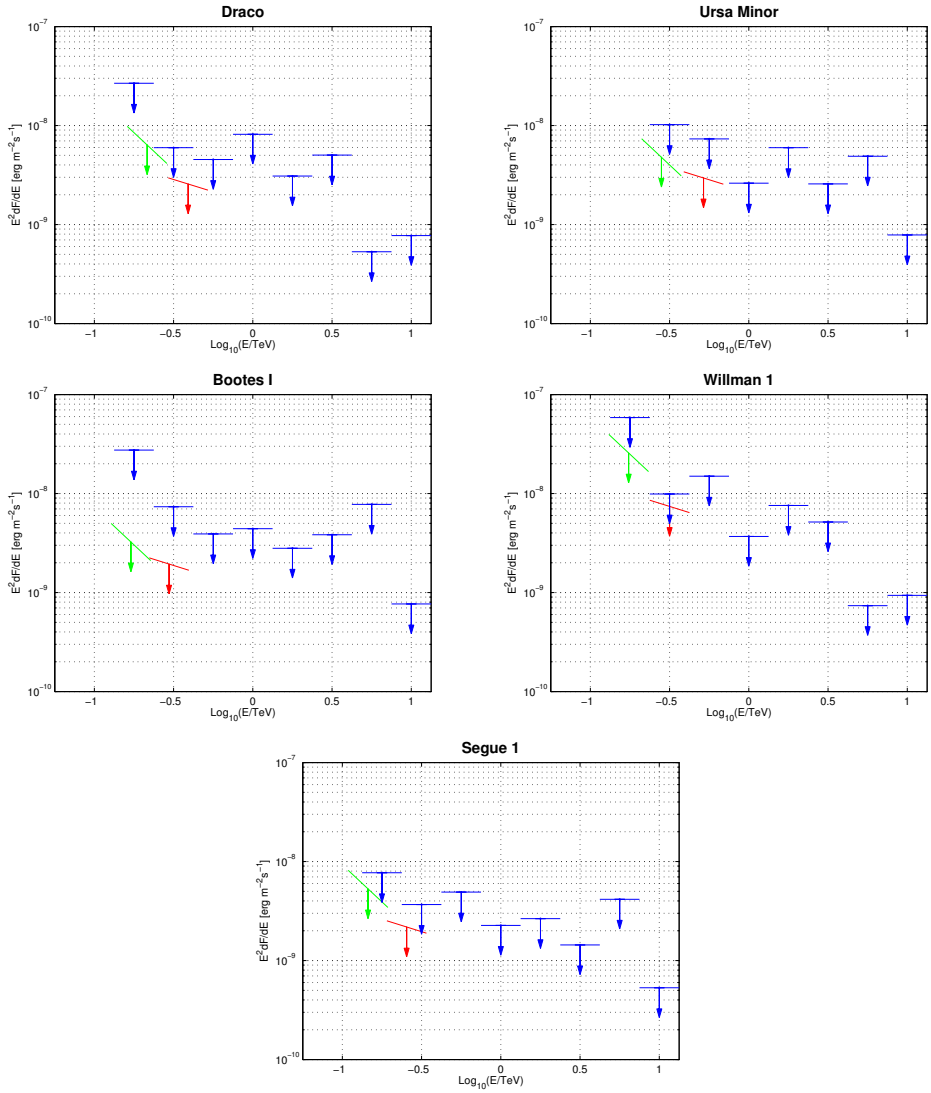

Figure 5.6 95% C.L. upper limits on the gamma-ray spectral energy density as a function of gamma-ray energy obtained with the *Standard* cuts analysis (blue arrows) for each of the observed dSphs. Upper limits on the spectral energy density from the integral analysis (see Table 5.5) are shown for the power-law energy distribution with $\Gamma = 2.5$ (red arrow) and $\Gamma = 3.5$ (green arrow). The slope of the line above each integral limit indicates the slope of the spectral energy distribution for which that limit was derived.

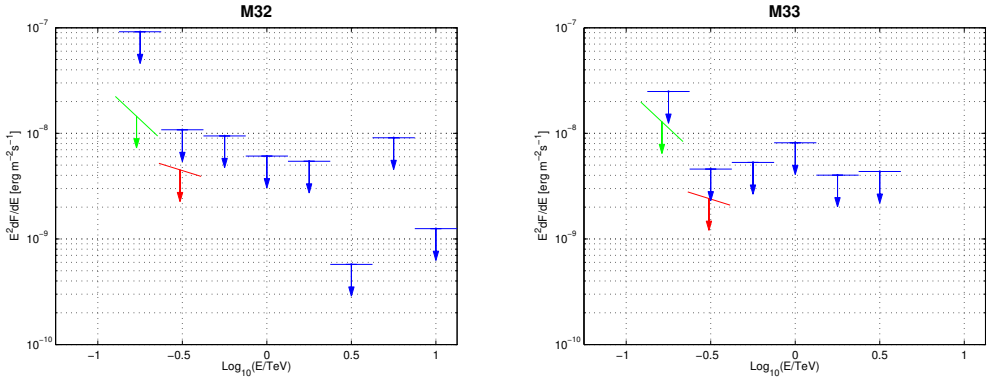

Figure 5.7 95% C.L. upper limits on the gamma-ray spectral energy density as a function of gamma-ray energy obtained with the *Standard* cuts analysis (blue arrows) for M32 (**left**) and M33 (**right**). Upper limits on the spectral energy density from the integral analysis (see Table 5.5) are shown for the power-law energy distribution with $\Gamma = 2.5$ (red arrow) and $\Gamma = 3.5$ (green arrow). The slope of the line above each integral limit indicates the slope of the spectral energy distribution for which that limit was derived.

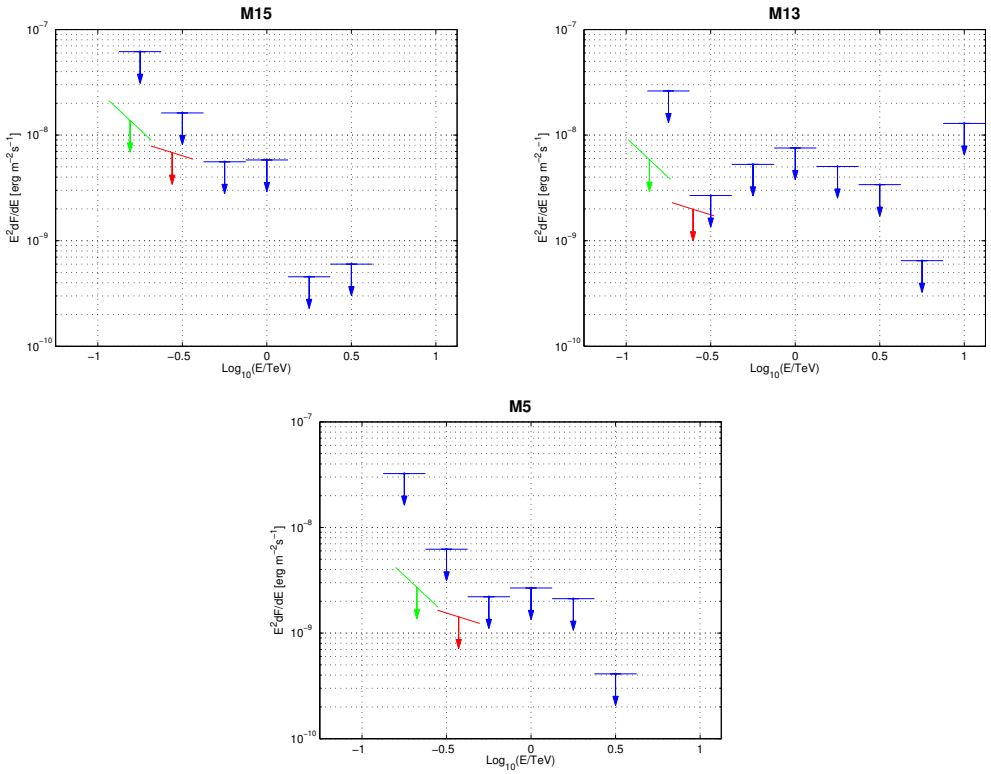

Figure 5.8 95% C.L. upper limits on the gamma-ray spectral energy density as a function of gamma-ray energy obtained with the *Standard* cuts analysis (blue arrows) for the three observed globular clusters. Upper limits on the spectral energy density from the integral analysis (see Table 5.5) are shown for the power-law energy distribution with $\Gamma = 2.5$ (red arrow) and $\Gamma = 3.5$ (green arrow). The slope of the line above each integral limit indicates the slope of the spectral energy distribution for which that limit was derived.

Figures 5.6–5.8 show the limits on the spectral energy density as a function of gamma-ray energy derived with *Standard* cuts analysis. For comparison the integral (energy-independent) limits for *Standard* and *Soft* cuts analyses are shown at the corresponding energy thresholds. Two different models of the background, maximum likelihood and reflected region, were used for integral and differential analyses respectively.

5.4 Spatial DM Distribution Constraints

The distribution of DM in the dSph systems was constrained by analyzing the distribution of stellar line-of-sight velocities and projected positions using the orbit modeling methodology (Section 4.6.1). This analysis was used to estimate both the expected spatial distribution of the annihilation signal (through the determination of the scale radius r_s) and its amplitude (through the evaluation of $\tilde{J}$) including estimate of systematic uncertainties. Stellar velocity data sets were taken from Muñoz et al. (2005) for Draco and Ursa Minor, Willman et al. (2010) for Willman 1, Geha et al. (2009) for Segue 1 and Martin et al. (2007) for Bootes I. Table 5.6 summarizes the mean velocity, velocity dispersion, and number of stars in each data set. An effective tidal radius, r_t, was chosen to be slightly larger than the most distant star in each galaxy. The tidal radius was used to construct a model for the orbital energy distribution given in Equation 4.22.

Table 5.7 shows the constraints on the spherically symmetric DM potential of each dSph derived assuming an NFW potential (Equation 4.15) and a flat orbital energy distribution truncated at the tidal radius. Constraints on $\tilde{J}$ are derived for an integration aperture of radius 0.3°. Figure 5.9 illustrates the likelihood contours for Draco and Segue 1 in the $\log_{10}\tilde{J} - \log_{10} M(r_s)$ plane. The p.d.f. for

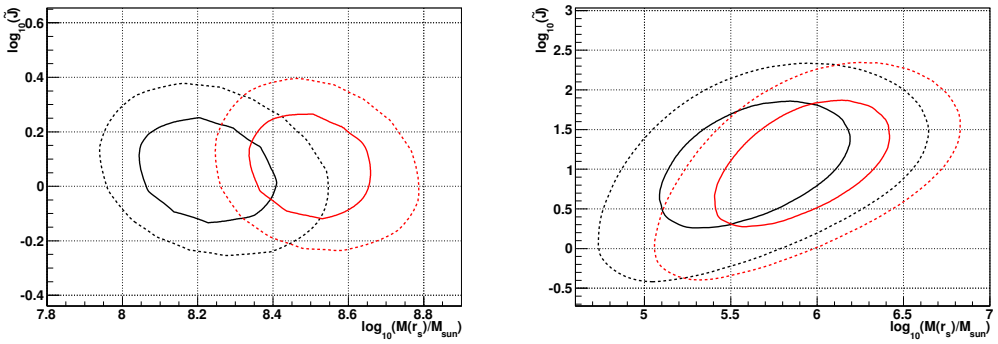

Figure 5.9 68% (solid lines) and 90% (dashed lines) C.L. regions in the $\log_{10}(\tilde{J})$-$\log_{10}(M(r_s))$ parameter space derived for the Draco (**left**) and Segue 1 (**right**) stellar velocity data sets. Black (red) lines indicate the constraints derived assuming an NFW (Hernquist) DM potential.

$\tilde{J}$ is found to follow an approximately log-normal distribution. The $\tilde{J}$ value for Draco and Ursa Minor is most well-defined due to the significantly larger data sets for these galaxies ($N_{\rm star} \simeq 200$). The three smaller dSphs have progressively larger values of $\tilde{J}$ with Segue 1 having an estimate approximately an order of magnitude larger than that of Draco and Ursa Minor but with significantly larger uncertainty. In general due to the small data samples of these systems, the trend of increasing J is not statistically significant. To evaluate the robustness of the constraints on $\tilde{J}$ and therefore potential systematic errors, the same stellar velocity analysis was performed for a Hernquist potential (Equation 4.14). Although the Hernquist profile generally provides poor fits to the DM distribution of simulated halos, this analysis demonstrates the sensitivity of $\tilde{J}$ to the assumed orbital energy distribution. Table 5.8 illustrates a comparison of the constraints on $\tilde{J}$ computed for the NFW and Hernquist potentials. Although the derived parameters r_s, ψ_0, and $M(r_s)$ differ significantly between the two models, the value of $\tilde{J}$ is negligibly

Table 5.6. Summary of the line of sight velocity data sets of the five observed dSphs. The column r_t indicates the tidal radius that was assumed for the stellar distribution.

Name	$\langle v_z \rangle$ [km s^{-1}]	σ_z [km s^{-1}]	r_t [kpc]	D [kpc]	$N_{\rm star}$	Ref.
Draco	-290.8 ± 0.7	10.8 ± 0.6	2.0	76 ± 5	210	1
Ursa Minor	-245.2 ± 0.8	11.5 ± 0.6	2.0	66 ± 3	213	1
Bootes I	99.9 ± 2.4	9.0 ± 2.2	0.5	62 ± 3	44	2,3
Willman 1	-14.1 ± 1.0	4.0 ± 0.9	0.2	38 ± 7	45	4
Segue 1	206.4 ± 1.3	4.3 ± 1.1	0.1	23 ± 2	24	5

References. — (1) Muñoz et al. (2005); (2) Martin et al. (2007); (3) Norris et al. (2008); (4) Willman et al. (2010) ; (5) Geha et al. (2009)

impacted by change of DM potential.

5.5 WIMP Annihilation Gamma-ray Flux Limits

Upper limits on the gamma-ray flux from WIMP annihilations were evaluated for each source using a model for the expected spatial emission profile and spectrum. Limits were evaluated for the case of both the neutralino of SUSY and the $B^{(1)}$ Kaluza-Klein (KK) excitation of UED. As discussed in Section 4.2, the shape of the continuum spectrum from WIMP annihilations is relatively similar for all final state channels with the exception of $\tau^+\tau^-$ which produces a significantly harder spectrum. A benchmark neutralino spectrum was adopted with

Table 5.7. Constraints on the NFW model parameters of the DM distribution of the five observed dSphs. An integration aperture of radius 0.4° was used for the calculation of line-of-sight integral $\tilde{J}$.

Name	$\log_{10}(\tilde{J})$	r_s [kpc]	ψ_0 [km^2 s^{-2}]	ρ_s [$M_\odot$ pc^{-3}]	$M(r_s)$ [$10^6 M_\odot$]
Draco	0.09 ± 0.19	1.2 ± 0.22	3020 ± 380	$0.038^{+0.027}_{-0.016}$	164^{+93}_{-53}
Ursa Minor	-0.12 ± 0.21	$3.8^{+0.7}_{-1.2}$	5200^{+700}_{-1200}	$0.0065^{+0.0074}_{-0.0026}$	883^{+68}_{-47}
Bootes I	0.18 ± 0.44	$0.22^{+0.11}_{-0.07}$	990^{+400}_{-270}	$0.39^{+0.98}_{-0.27}$	$9.7^{+17}_{-0.6}$
Willman 1	0.37 ± 0.49	$0.13^{+0.07}_{-0.05}$	590^{+270}_{-190}	$0.65^{+1.8}_{-0.46}$	$3.4^{+6.4}_{-2.1}$
Segue 1	1.07 ± 0.80	$0.027^{+0.016}_{-0.011}$	360^{+270}_{-160}	$9.2^{+43}_{-7.3}$	$0.43^{+1.1}_{-0.30}$

Table 5.8. Comparison of constraints on the line-of-sight integral $\tilde{J}$ derived assuming an NFW potential ($\tilde{J}_N$) and a Hernquist potential ($\tilde{J}_H$). The fourth column shows the estimate of $\tilde{J}$ taken from the reference in column five.

Name	$\log_{10}(\tilde{J}_N)$	$\log_{10}(\tilde{J}_H)$	$\log_{10}(\tilde{J})$	Ref.
Draco	0.09 ± 0.19	0.06 ± 0.19	0.37 ± 0.10	1
Ursa Minor	-0.12 ± 0.21	-0.14 ± 0.20	0.31 ± 0.14	1
Bootes I	0.18 ± 0.44	0.19 ± 0.44	-0.12 ± 0.50	1
Willman 1	0.37 ± 0.49	0.41 ± 0.48	0.33 ± 0.90[a]	2
Segue 1	1.07 ± 0.80	1.12 ± 0.80	0.42 ± 0.60	3

References. — (1) Abdo et al. (2010a); (2) Strigari et al. (2008b); (3) Essig et al. (2010)

[a]Errors correspond to 90% confidence level interval.

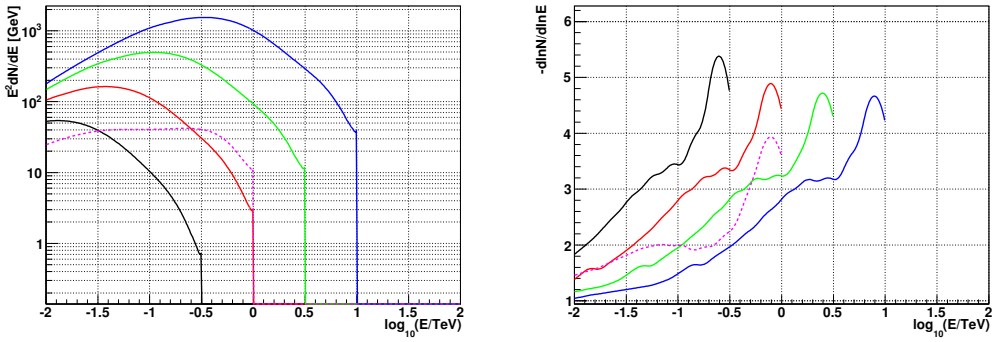

Figure 5.10 **Left:** Differential annihilation yield as a function of gamma-ray energy for a neutralino WIMP of mass 316 GeV (solid black line), 1 TeV (solid red line), 3.16 TeV (solid green line), and 10 TeV (solid blue line) and a KK WIMP of mass 1 TeV (dashed purple line). **Right:** Logarithmic slope of the differential annihilation yield ($-d\ln N/d\ln E$) as a function of energy of the five WIMP models shown in the left panel.

final state branching ratios of 90% and 10% to $b\bar{b}$ and $\tau^+\tau^-$ respectively. As shown in Figure 5.10 this spectrum exhibits strong curvature and has a peak in spectral energy density at the energy which is approximately factor of 30 lower than the neutralino mass. The slope of the neutralino spectrum in the gamma-ray energy band centered in the region of maximal VERITAS sensitivity (around $E \simeq 316$ GeV) is therefore a strong function of the neutralino mass. For the theoretically preferred mass range for the neutralino in the MSSM scenarios (100 GeV – 1 TeV), the logarithmic slope of the annihilation spectrum is relatively soft ($\Gamma \gtrsim 3$). A benchmark KK spectrum was evaluated using the final state branching ratios from Hooper & Profumo (2007). Due to the dominant contribution of charged leptons, the KK WIMP spectrum is significantly harder relative to the neutralino WIMP with $\Gamma \simeq 2$–2.5 at $E \simeq 316$ GeV.

The spatial profile of the gamma-ray emission from WIMP annihilations is determined by the line of sight integral over the DM density profile (Section 4.1). The DM distribution in the core of the local group galaxies M32 and M33 and globular clusters M5, M13, and M15 is very weakly constrained due to the dominant contribution of baryonic matter to the gravitational potential in these regions. Gravitational interactions between baryons and DM in these objects could potentially enhance the DM density on small scales (see Section 4.5 for a discussion of these effects). The dominant fraction of the DM self-annihilation emission in these systems is expected to arise from a very small region that would appear point-like as compared to the instrumental PSF of VERITAS. Therefore a point-source emission model is adopted for these five sources. For the five dSphs, the emission profiles were calculated using the NFW halo model and the scale radii from Table 5.7 that were inferred from the orbit modeling analysis. Figure 5.11 shows a comparison of the spatial emission profiles of the five dSphs calculated by convolving the line-of-sight intensity ($d\tilde{J}/d\Omega$) with the VERITAS PSF. The emission profiles of Bootes I, Willman 1, and Segue 1 are nearly point-like while Draco and Ursa Minor demonstrate significant extension.

Upper limits on the spectral energy density of both neutralino and KK WIMPs were calculated using the *Soft* cuts analysis. This analysis was found to provide improved sensitivity relative to *Standard* cuts for both KK and neutralino WIMPs in the mass range around 1 TeV which is justified by the expected logarithmic slope of annihilation spectra (Figure 5.10). Table 5.9 gives the upper limits on the gamma-ray spectral energy density and gamma-ray integral flux from neutralino and KK WIMPs with a mass of 1 TeV. Due to its steeper spectral slope, sensitivity to the neutralino WIMP is a strong function of the energy threshold which can vary by as a much as a factor of 2 (see Figure 5.12) due to the average zenith angle of the observation and changes to the instrument configuration. Figures

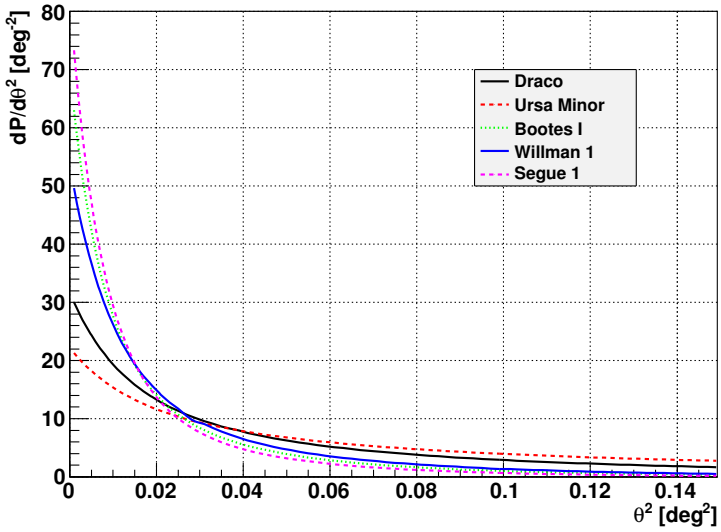

Figure 5.11 Spatial emission profile for WIMP annihilation of the five dSphs calculated using the NFW model parameters from Table 5.7 and the benchmark neutralino spectral model with mass 1 TeV. The line for Segue 1 is representative of the gamma-ray PSF.

Table 5.9. Summary of energy thresholds, upper limits on the gamma-ray spectral energy density, and upper limits on the integral gamma-ray flux derived for a 1 TeV neutralino and KK WIMP.

Name	Neutralino			KK		
	E_{th}[a] [GeV]	E^2dF/dE[b] [erg m^{-2} s^{-1}]	$\Phi_{\text{u.l.}}$[c] [m^{-2} s^{-1}]	E_{th}[a] [GeV]	E^2dF/dE[b] [erg m^{-2} s^{-1}]	$\Phi_{\text{u.l.}}$[c] [m^{-2} s^{-1}]
Draco	225	$< 1.3 \times 10^{-8}$	$< 9.5 \times 10^{-8}$	272	$< 8.8 \times 10^{-9}$	$< 4.6 \times 10^{-8}$
Ursa Minor	288	$< 1.8 \times 10^{-8}$	$< 1.8 \times 10^{-7}$	346	$< 1.3 \times 10^{-8}$	$< 7.1 \times 10^{-8}$
Bootes I	176	$< 4.3 \times 10^{-9}$	$< 2.3 \times 10^{-8}$	206	$< 2.6 \times 10^{-9}$	$< 1.3 \times 10^{-8}$
Willman 1	182	$< 2.8 \times 10^{-8}$	$< 1.6 \times 10^{-7}$	221	$< 1.8 \times 10^{-8}$	$< 9.1 \times 10^{-8}$
Segue 1	153	$< 4.9 \times 10^{-9}$	$< 2.2 \times 10^{-8}$	180	$< 3.0 \times 10^{-9}$	$< 1.5 \times 10^{-8}$
M5	216	$< 2.8 \times 10^{-9}$	$< 1.9 \times 10^{-8}$	251	$< 1.8 \times 10^{-9}$	$< 9.0 \times 10^{-9}$
M13	148	$< 5.1 \times 10^{-9}$	$< 2.2 \times 10^{-8}$	178	$< 2.9 \times 10^{-9}$	$< 1.5 \times 10^{-8}$
M15	162	$< 1.3 \times 10^{-8}$	$< 6.1 \times 10^{-8}$	190	$< 7.8 \times 10^{-9}$	$< 4.0 \times 10^{-8}$
M32	178	$< 1.4 \times 10^{-8}$	$< 7.3 \times 10^{-8}$	215	$< 8.1 \times 10^{-9}$	$< 4.1 \times 10^{-8}$
M33	174	$< 1.1 \times 10^{-8}$	$< 6.1 \times 10^{-8}$	221	$< 6.6 \times 10^{-9}$	$< 3.4 \times 10^{-8}$

[a]Energy at the peak of the differential detection rate for the corresponding WIMP spectral model.

[b]95% C.L. spectral energy density upper limit at E_{th}.

[c]95% C.L. upper limit on the integral gamma-ray flux above 100 GeV.

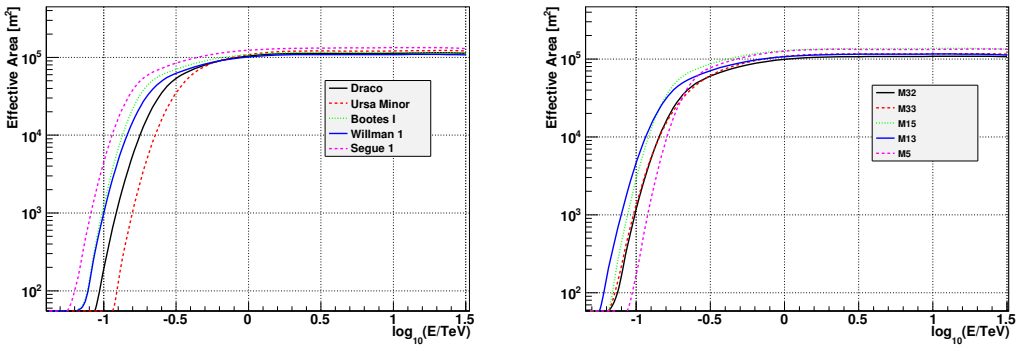

Figure 5.12 Gamma-ray effective collecting area as a function of gamma-ray energy for the *Soft* cuts analysis of the five dSph systems (**left**) and the two local group galaxies and three globular clusters (**right**). Differences in collecting area are mostly due to two factors: the average zenith angle of the observations and the change of the VERITAS layout in Summer 2009 and optimal analysis cuts.

5.13 and 5.14 show the analysis energy threshold and upper limit on the spectral energy density as a function of WIMP mass between 100 GeV and 10 TeV for the neutralino spectral model.

5.6 WIMP Parameter Space Constraints

Upper limits on $\langle\sigma v\rangle$ as a function of WIMP mass, m_{WIMP}, were calculated for each dSph using the upper limit on the gamma-ray flux from WIMP annihilation and the estimate of $\tilde{J}$ (Table 5.7). The uncertainties on the estimate of $\tilde{J}$ dominates the uncertainty of the evaluation of the limits on $\langle\sigma v\rangle$. Draco and Ursa Minor have the smallest uncertainties of $\sim$40% while the other three dSphs have uncertainties of a factor 2–5. Figure 5.15 shows the limits on $\langle\sigma v\rangle$ derived from Draco and Segue 1 data sets for the benchmark neutralino spectrum. The best

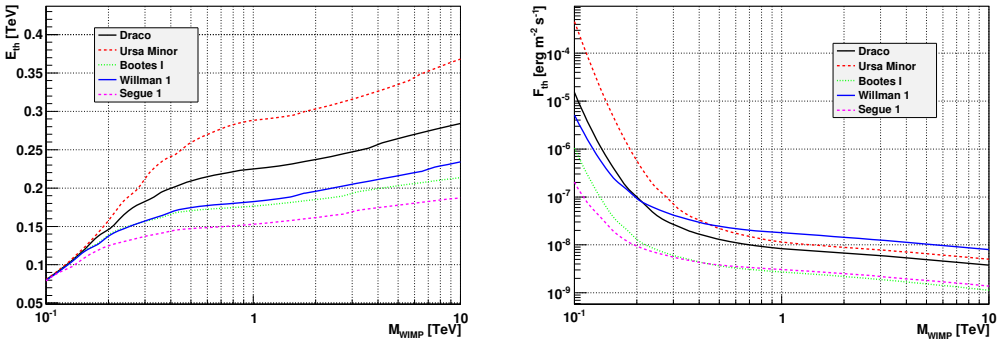

Figure 5.13 **Left:** Energy threshold (E_{th}) as a function of WIMP mass for the *Soft* cuts analysis of the five dSphs (Draco, Ursa Minor, Bootes I, Willman 1, and Segue 1) and the benchmark neutralino spectrum with BR($b\bar{b}$) = 0.9 and BR($\tau^+\tau^-$) = 0.1. **Right:** 95% C.L. upper limit on the spectral energy density from WIMP annihilations evaluated at E_{th} shown in the left figure as a function of WIMP mass.

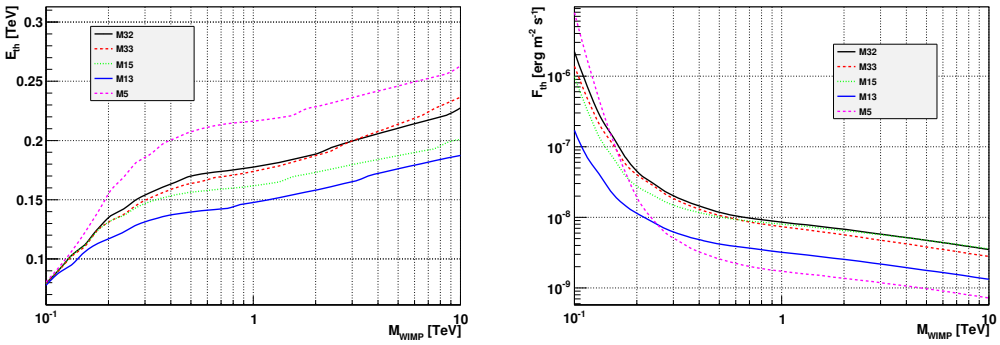

Figure 5.14 **Left:** Energy threshold (E_{th}) as a function of WIMP mass for the *Soft* cuts analysis of M32, M33, M15, M13, and M5 and the benchmark neutralino spectrum with BR($b\bar{b}$) = 0.9 and BR($\tau^+\tau^-$) = 0.1. **Right:** 95% C.L. upper limit on the spectral energy density from WIMP annihilations as a function of WIMP mass evaluated at $E_{th}(M_{\rm WIMP})$ shown in the left figure.

constraints on $\langle \sigma v \rangle$ are achieved for $M_{\rm WIMP} \simeq$ 1–2 TeV of $\sim 8 \times 10^{-23}$ cm^3 s^{-1} and $\sim 2 \times 10^{-24}$ cm^3 s^{-1} for Draco and Segue 1 respectively. Sensitivity declines rapidly for WIMP masses below 300 GeV due to the steep fall-off of the VERITAS effective area below the analysis energy threshold. A gradual change in the sensitivity at larger neutralino masses occurs due to slower increase of the VERITAS collecting area and dependence of the particle physics factor (Equation 4.1) on the neutralino mass. Although with large uncertainties, the limits from Segue 1 are more than an order of magnitude lower than for Draco. The greater sensitivity is attributable to the larger value of J (factor of 10), lower energy threshold, larger exposure, smaller angular extent consistent with the point-source, and the overall improvement of the VERITAS sensitivity after the relocation of the T1 telescope due to better background rejection.

For comparison with the limits on $\langle \sigma v \rangle$ of the neutralino, a set of MSSM models were generated with the DarkSUSY code by performing a logarithmic scan over the MSSM parameters defined in Gondolo et al. (2004): μ, M_2, m_A, $\tan\beta$, $m_{\tilde{q}}$, A_t, and A_b. The models shown in Figure 5.15 were required to have a relic density, $\Omega_\chi h^2$, within ± 3 standard deviations of the DM relic density measured with the five year WMAP data set (Komatsu et al., 2009) and satisfy various constraints imposed by accelerator searches. High accuracy measurement of the DM relic density limits the majority of models to a narrow band with $\langle \sigma v \rangle \simeq 2 - 3 \times 10^{-26}$ cm^3 s^{-1}. The limits inferred from Draco and Segue 1 are approximately 2–3 orders of magnitude above this critical for MSSM models range. For comparison the limits on $\langle \sigma v \rangle$ inferred from 1-year Fermi-LAT observations of Draco (Abdo et al., 2010a) and the extragalactic gamma-ray background (Abdo et al., 2010b) for a neutralino WIMP with a 100% branching ratio to bb are shown. In the case of Draco the line-of-sight integral J used to derive these limits is a factor of 2 larger than that adopted for the work presented here. For the extra-

galactic background there is a very significant uncertainty in the J calculation due to the non-uniform distribution of the DM and the limits shown uses the intermediate value between the most and least optimistic scenarios differing by at least two orders of magnitude. In general however Fermi-LAT is more sensitive than VERITAS in the intermediate range of WIMP masses (100–700 GeV) due to the neutralino spectrum peaking at 1–10 GeV where Fermi-LAT achieves its best sensitivity.

Limits on $\langle \sigma v \rangle$ for the KK WIMP are illustrated in Figure 5.16. An analytic expression for $\langle \sigma v \rangle$ as a function of m_{WIMP} is taken from Servant & Tait (2003). Unlike the case for the neutralino WIMP, the harder gamma-ray spectrum of the KK WIMP produces more constraining limits inferred from VERITAS observations than those derived from the Fermi-LAT data. However, all limits are 1–2 orders of magnitude above favored theoretical predictions for the KK WIMP.

The contribution of DM substructures to the gamma-ray annihilation flux could increase the line of sight integral by a boost factor of 1–100 (Section 4.4) and consequently lower the limits on $\langle \sigma v \rangle$. Martinez et al. (2009) conservatively estimate a substructure boost factor of ~ 1 by extrapolating the mass function and mass-concentration relations to the DM substructure mass cutoff. Strigari et al. (2007) set an upper limit on the boost factor of ~ 100 by using an optimistic extrapolation of the substructure gamma-ray luminosity function. The spatial distribution of the DM substructures is of critical importance for estimating their contribution to the DM annihilation luminosity. While the gamma-ray flux arising from the smooth DM distribution scales as the square of the local DM density, the luminosity from substructures scales as the substructure number density. High-resolution CDM simulations have found that the substructure number density approximately traces the DM density (Diemand & Moore, 2009). There-

fore the annihilation flux from DM substructures is distributed over significantly larger spatial scales than that of smooth DM distribution. The distribution of substructures can further be affected by tidal interaction at large scales and by interactions with the high densities of baryonic matter on small scales. For example, for Draco and Ursa Minor the relatively large scale radius of ~ 1 kpc suggests that the significant fraction of the annihilation luminosity arising from substructures is likely to be too extended relative to the VERITAS PSF to significantly boost the detectability of WIMP annihilations. For the spatially smaller systems such as Segue 1, the substructures which survived the tidal interaction are likely to contribute to the point-source-like DM annihilation luminosity. However the fraction of DM substructures surviving tidal stripping is largely uncertain. In the case of condensed baryonic systems such as galactic nuclei or globular clusters, the fate of DM substructures is even more uncertain because of intense interaction with high density baryonic matter. These considerations suggest that the boost factor of the systems observed is likely limited to a moderate range of 1–10.

The Sommerfeld enhancement has been extensively studied as a mechanism for boosting the annihilation cross section above its natural value (Hisano et al., 2004; Cirelli et al., 2007; Arkani-Hamed et al., 2009). This effect can arise due to a long-range attractive force between WIMPs which gives a WIMP velocity dependent correction to the annihilation cross section. The analog of this effect in electromagnetism is exemplified by the dependence of the cross section for a long-range screened coulomb interaction (Yukawa scattering) on the particle's energy in which case the cross section rapidly increases as energy decreases when the screening parameter vanishes (Rutherford scattering). Such a force could be mediated by the W/Z bosons (Hisano et al., 2004) or a new light force carrier introduced in theoretical considerations (Arkani-Hamed et al., 2009) to further enhance this effect. The Sommerfeld enhancement factors are predicted to be

particularly large (up to 10^4) for very large mass neutralinos (above 1 TeV) or particularly low mass light force carrier (much less than M_Z/M_W). If neutralino mass is in the TeV range or above the Sommerfeld effect can provide very significant improvement of constraints shown in Figure 5.15. In this sense the upper limit derived in this work could be interpreted as a constraint on the cumulative effect of DM substructure boost factor and Sommerfeld effect if illustrated MSSM models in regime of WIMP mass larger 1 TeV are assumed valid then this cumulative factor is constrained to be below 10^4.

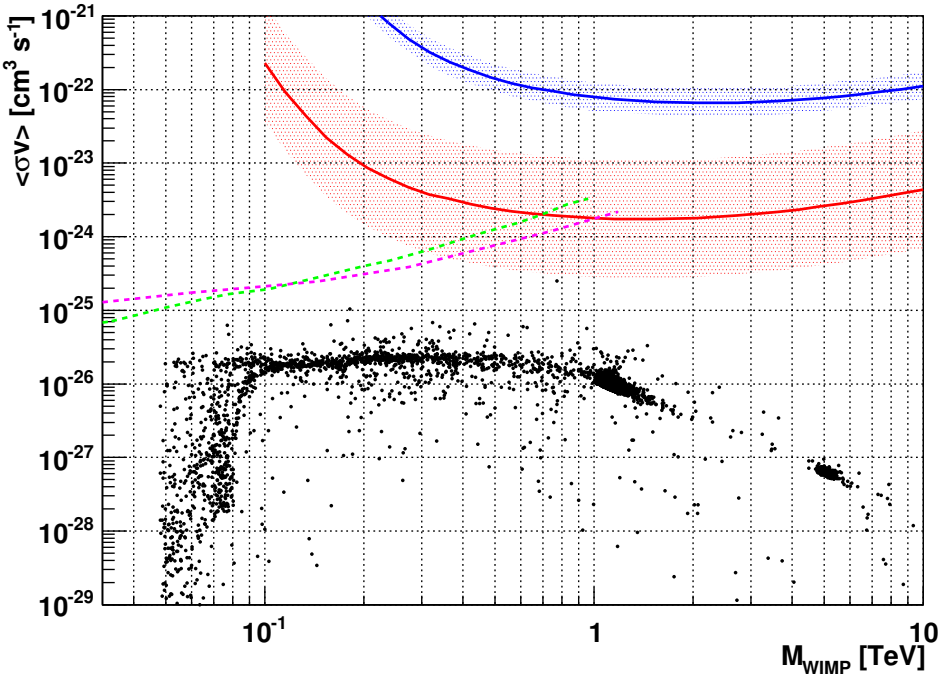

Figure 5.15 95% C.L. Upper limits on $\langle \sigma v \rangle$ of the neutralino WIMP as a function of $M_{\rm WIMP}$ as inferred from observations of Draco (blue solid curve) and Segue 1 (red solid curve) for the benchmark neutralino spectral model. Shaded regions indicate the 1σ theoretical uncertainty on the upper limit associated with the calculation of J. Shown as black circles are MSSM models generated with DarkSUSY that fall within ± 3 standard deviations of the relic density measured in the five year WMAP data set (Komatsu et al., 2009). The green dashed line indicates the upper limits on $\langle \sigma v \rangle$ inferred from Fermi-LAT observations of Draco (Abdo et al., 2010a). The purple dashed line indicates the upper limits on $\langle \sigma v \rangle$ inferred from the Fermi-LAT measurement of the high latitude ($l \geq 10^{\circ}$) extragalactic gamma-ray background (Abdo et al., 2010b).

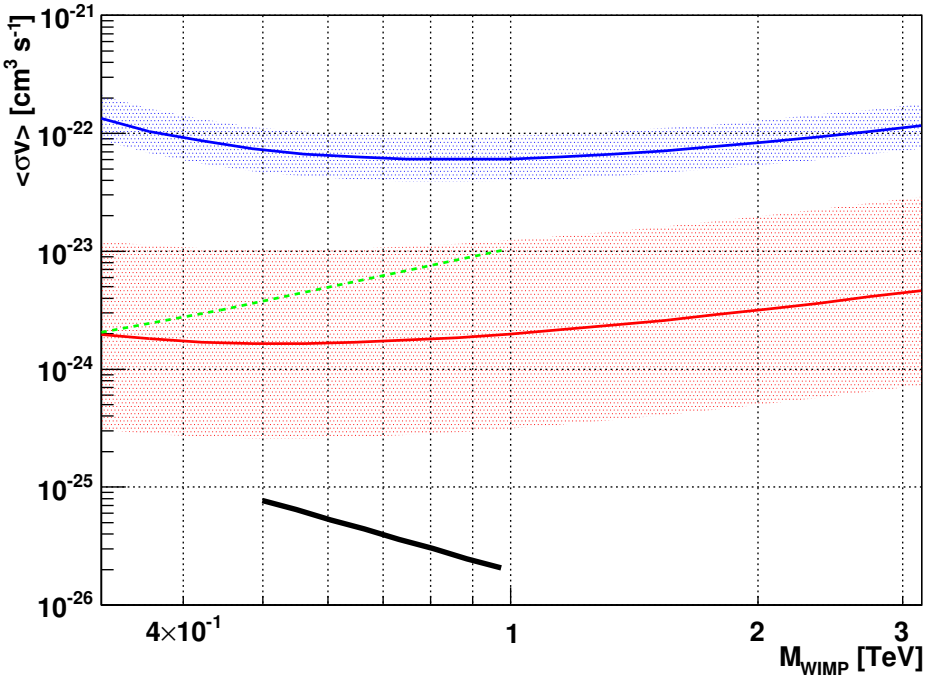

Figure 5.16 Upper limits on $\langle \sigma v \rangle$ of the KK WIMP as a function of $M_{\rm WIMP}$ as inferred from observations of Draco (blue solid curve) and Segue 1 (red solid curve) for the benchmark KK spectral model. Shaded regions indicate the 1σ theoretical uncertainty on the upper limit associated with the calculation of J. Shown as a solid black line is the preferred region for the $B^{(1)}$ LKP of UED. The green dashed line indicates the upper limits on $\langle \sigma v \rangle$ inferred from Fermi-LAT observations of Draco (Abdo et al., 2010a).

CHAPTER 6

Conclusions

This thesis reports the constraints on VHE gamma-ray emission from ten targets that were observed to search for the signature of WIMP annihilations. Analysis of these data with a standard point-source analysis (Section 5.3) found no significant emission and set limits on the spectral energy density of gamma-ray radiation from these objects at the level $\sim 5 \times 10^{-9}$ erg m^{-2} s^{-1} at 1 TeV ($\sim 1\%$ of the spectral energy density of the Crab Nebula). All fields were further studied with a two-dimensional analysis technique. No significant gamma-ray excesses were detected within any of the $\sim 3^{\circ}$ observation fields.

Five of the ten observed systems have a mass distribution dominated by baryons at small scales — the two local group galaxies (M32 and M33) and three globular clusters (M5, M13, and M15). Although large uncertainty exists in the DM content of these systems, the compression of DM through the infall of baryons into the cores of these objects suggest the possibility of very high luminosity enhancement factors up to 10^6 (Wood et al., 2008). From the point of view of the detection of DM self-annihilation flux, observations of these systems are of significant interest. However, non-detection of the WIMP annihilation signature reported in this work can be interpreted only as a joint constraint on both the particle and astrophysical properties of DM. For this reason the observational upper limits for the DM self-annihilation provided by these baryon-dominated systems can not be uniquely interpreted and used to establish reliable constraints on the

WIMP parameters.

A stellar orbit modeling analysis technique was developed to infer the distribution of DM in dSph galaxies from the distribution of stellar line-of-sight velocities and positions (Section 4.6). This method differs from conventional analyses using the spherical Jeans Equation (see for example Strigari et al. (2007)) in that it considers the p.d.f. of the observables of individual stars and makes assumptions about their distribution in energy and angular momentum space. A similar approach that utilizes the same basic methodology was previously described in the context of dSphs in Wilkinson et al. (2002) and applied to the Draco dSph in Kleyna et al. (2002). The orbit modeling analysis was used to constrain the value of the line-of-sight integral, J, over the DM distribution in each system given a parametric model for the DM potential motivated by CDM simulations. The best constraints on J were obtained for the two dSphs with the largest stellar velocity data sets, Draco and Ursa Minor, resulting in statistical uncertainties of $\sim 50\%$. These estimates of J were a factor of ~ 2 lower than those reported in Abdo et al. (2010b) but consistent within the statistical uncertainties. Estimates of J were significantly less statistically constrained for the three fainter dSph systems due to the smaller sizes of the stellar velocity samples. Segue 1 was found to have the largest J value ($\tilde{J} \simeq 10$) of the five dSphs studied but with a statistical uncertainty of nearly an order of magnitude. These constraints could be significantly improved by increasing the sample of stars with known stellar velocity and position data. The ongoing efforts in this direction (Simon et al., 2010) promise to improve these estimates and could potentially affect the limits reported in this thesis.

Constraints on the present-day thermally averaged product of the cross section and relative velocities of the WIMPs, $\langle \sigma v \rangle$, as a function of WIMP mass were

derived for neutralino and KK WIMP models based on the observations of the five dSphs in which the spatial distribution of DM is constrained to varying degrees by the stellar kinematics data. The highest sensitivity to WIMP self-annihilations is achieved for WIMP models with masses near 1 TeV. Robust upper limits on $\langle \sigma v \rangle$ of $\sim 10^{-22}$ cm^3 s^{-1} were derived from observations of Draco and Ursa Minor. Observations of Segue 1 resulted in much lower limits of 10^{-23}–10^{-24} cm^3 s^{-1} but are subject to a significantly larger uncertainty in the line-of-sight integral (J values). The constraints on $\langle \sigma v \rangle$ reported in this thesis are approximately 2–3 orders of magnitude above the predictions of conventional MSSM and KK models assuming no boost factor from substructure and no additional particle-related gamma-ray flux enhancement factors due to the Sommerfeld effect and virtual internal bremsstrahlung (Section 4.2). Should the latter effects be included, the constraints on $\langle \sigma v \rangle$ in the most optimistic regime could be pushed down by a factor as large as 10^5. If the validity of MSSM models is assumed then the reported observations limit the cumulative role of these effects. Extreme enhancement factors of 10^3–10^4 which are the upper limit for enhancement by the Sommerfeld effect with light force carriers (Arkani-Hamed et al., 2009) are therefore already ruled out by these observations. For conventional interaction between neutralinos by exchange of weak bosons, the Sommerfeld effect may be particularly large for high mass neutralinos (above 1 TeV). The data reported in this thesis suggest an upper limit in this M_{WIMP} regime of $\sim 10^4$.

Although gamma-ray searches for the WIMP have yet to exclude theoretically favored regions of the WIMP parameter space, these searches remain of critical importance to unraveling the nature of DM and are highly complementary to accelerator searches and direct DM detection experiments. Unlike the signature of WIMP-nucleon scattering, the cross section of WIMP self-annihilation is naturally constrained to a relatively narrow band defined by the bounds on the

relic DM density measured by WMAP. Gamma-ray instruments with sufficient sensitivity to reach this band can thus rule out a majority of WIMP models. VHE gamma-ray searches are also uniquely sensitive to heavy WIMPs with mass greater than 1 TeV which would be especially challenging to detect in an accelerator or direct detection experiment. Finally, the identification of the WIMP gamma-ray signature is the only way to conclusively link the particle and astrophysical properties of DM.

To begin confronting the predictions of generic MSSM models through observation of presently known dSphs, future ground-based observatories such as CTA/AGIS (Buckley et al., 2008; CTA Consortium, 2010) will need collecting areas at least an order of magnitude larger than the present-day instruments. Observation of the DM self-annihilation signal will also benefit from the extension of the energy range to a sub-100 GeV domain where the DM self-annihilation flux is rapidly increasing. The importance of a low energy threshold was effectively demonstrated by the WIMP constraints derived from observations conducted with the Fermi-LAT (Abdo et al., 2010a,b). In the neutralino mass regime of less than a few hundred GeV, the Fermi-LAT provides the best upper limits on $\langle \sigma v \rangle$ in spite of the small collecting area of this instrument relative to ground-based instruments. Combining these two strategies (increasing collecting area and decreasing energy threshold) with dedicated deep observations of dSph systems (200–500 hours), may allow a future ground-based instrument to rule out the majority of conventional MSSM models. The list of dSphs favorable for observations of DM self-annihilation has grown over the last years by a factor of roughly two, and it is anticipated that newly discovered dSphs may offer larger J values. Perhaps more importantly the rapidly growing kinematic data for dSphs will provide increasingly robust constraints on the DM distribution in these systems thereby reducing uncertainty on the allowable parameter space of the WIMP

particle physics characteristics.

CHAPTER 7

Bibliography

Bibliography

Abdo, A. A. et al. 2009a, Physical Review Letters, 102, 181101

—. 2009b, Science, 325, 845

—. 2010a, ApJ, 712, 147

—. 2010b, Journal of Cosmology and Astro-Particle Physics, 4, 14

Acciari, V. A. et al. 2010, ApJ, 720, 1174

—. 2008, ApJ, 679, 1427

Adriani, O. et al. 2009a, Nature, 458, 607

—. 2009b, Physical Review Letters, 102, 051101

Aharonian, F. et al. 2009a, A&A, 508, 561

—. 2008a, Physical Review Letters, 101, 261104

—. 2006, Physical Review Letters, 97, 221102

—. 2008b, Astroparticle Physics, 29, 55

—. 2009b, ApJ, 691, 175

Aharonian, F. A. et al. 2004, A&A, 425, L13

—. 2003, A&A, 400, 153

Albert, J. et al. 2008, ApJ, 679, 428

Aliu, E. et al. 2009, ApJ, 697, 1299

Aparicio, A., Carrera, R., & Martínez-Delgado, D. 2001, AJ, 122, 2524

Appelquist, T., Cheng, H.-C., & Dobrescu, B. A. 2001, Phys. Rev. D, 64, 035002

Aprile, E. et al. 2009, Phys. Rev. C, 79, 045807

Aprile, E., & XENON Collaboration. 2010, Journal of Physics Conference Series, 203, 012005

Arkani-Hamed, N., Finkbeiner, D. P., Slatyer, T. R., & Weiner, N. 2009, Phys. Rev. D, 79, 015014

Asztalos, S. J. et al. 2010, Physical Review Letters, 104, 041301

Atwood, W. B. et al. 2009, ApJ, 697, 1071

Bahcall, J. N., & Wolf, R. A. 1976, ApJ, 209, 214

Baltz, E. A., Battaglia, M., Peskin, M. E., & Wizansky, T. 2006, Phys. Rev. D, 74, 103521

Baltz, E. A., Briot, C., Salati, P., Taillet, R., & Silk, J. 2000, Phys. Rev. D, 61, 023514

Battaglia, G. et al. 2005, MNRAS, 364, 433

Bednarek, W., & Sitarek, J. 2007, MNRAS, 377, 920

Bekki, K., Couch, W. J., Drinkwater, M. J., & Gregg, M. D. 2001, ApJ, 557, L39

Bellazzini, M., Ferraro, F. R., Origlia, L., Pancino, E., Monaco, L., & Oliva, E. 2002, AJ, 124, 3222

Belokurov, V. et al. 2007, ApJ, 654, 897

—. 2006, ApJ, 647, L111

Berezinsky, V., Dokuchaev, V., & Eroshenko, Y. 2006, Phys. Rev. D, 73, 063504

Berge, D., Funk, S., & Hinton, J. 2007, A&A, 466, 1219

Bergström, L., Bringmann, T., Eriksson, M., & Gustafsson, M. 2005, Physical Review Letters, 94, 131301

Bergström, L., Edsjö, J., & Gondolo, P. 1998a, Phys. Rev. D, 58, 103519

Bergström, L., & Hooper, D. 2006, Phys. Rev. D, 73, 063510

Bergström, L., & Ullio, P. 1997, Nuclear Physics B, 504, 27

Bergström, L., Ullio, P., & Buckley, J. H. 1998b, Astroparticle Physics, 9, 137

Bernabei, R. et al. 2008, European Physical Journal C, 167

Bernlohr, K. 2000, Astroparticle Physics, 12, 255

Bertone, G., Hooper, D., & Silk, J. 2005, Phys. Rep., 405, 279

Bertone, G., Sigl, G., & Silk, J. 2002, MNRAS, 337, 98

Binney, J., & Tremaine, S. 1987, Galactic dynamics (Princeton, NJ, Princeton University Press, 1987, 747 p.)

Birkedal, A., Matchev, K. T., Perelstein, M., & Spray, A. 2005, ArXiv High Energy Physics - Phenomenology e-prints

Blumenthal, G. R., Faber, S. M., Flores, R., & Primack, J. R. 1986, ApJ, 301, 27

Bonanos, A. Z., Stanek, K. Z., Szentgyorgyi, A. H., Sasselov, D. D., & Bakos, G. Á. 2004, AJ, 127, 861

Bottino, A., Donato, F., Fornengo, N., & Scopel, S. 2003, Phys. Rev. D, 68, 043506

—. 2004, Phys. Rev. D, 69, 037302

Bradač, M., Allen, S. W., Treu, T., Ebeling, H., Massey, R., Morris, R. G., von der Linden, A., & Applegate, D. 2008, ApJ, 687, 959

Bradbury, S. M., & Rose, H. J. 2002, Nuclear Instruments and Methods in Physics Research A, 481, 521

Bringmann, T., Bergström, L., & Edsjö, J. 2008, Journal of High Energy Physics, 1, 49

Bringmann, T., Doro, M., & Fornasa, M. 2009, Journal of Cosmology and Astro-Particle Physics, 1, 16

Buckley, J. et al. 2008, ArXiv e-prints

Bullock, J. S., Kolatt, T. S., Sigad, Y., Somerville, R. S., Kravtsov, A. V., Klypin, A. A., Primack, J. R., & Dekel, A. 2001, MNRAS, 321, 559

Burkert, A. 1995, ApJ, 447, L25+

Cawley, M. F. et al. 1990, Experimental Astronomy, 1, 173

CDMS II Collaboration. 2010, Science, 327, 1619

Cheng, H.-C., Feng, J. L., & Matchev, K. T. 2002, Physical Review Letters, 89, 211301

Cholis, I., Dobler, G., Finkbeiner, D. P., Goodenough, L., & Weiner, N. 2009, Phys. Rev. D, 80, 123518

Cirelli, M., Kadastik, M., Raidal, M., & Strumia, A. 2009, Nuclear Physics B, 813, 1

Cirelli, M., Strumia, A., & Tamburini, M. 2007, Nuclear Physics B, 787, 152

Clowe, D., Bradač, M., Gonzalez, A. H., Markevitch, M., Randall, S. W., Jones, C., & Zaritsky, D. 2006, ApJ, 648, L109

Colafrancesco, S., Profumo, S., & Ullio, P. 2007, Phys. Rev. D, 75, 023513

Corbelli, E., & Salucci, P. 2000, MNRAS, 311, 441

Corbin, M. R., O'Neil, E., & Rieke, M. J. 2001, AJ, 121, 2549

CTA Consortium, T. 2010, ArXiv e-prints

Dall'Ora, M. et al. 2006, ApJ, 653, L109

Davies, J. M., & Cotton, E. S. 1957, Journal of Solar Energy, Science and Engineering, 1(2), 16

de Blok, W. J. G. 2005, ApJ, 634, 227

de Blok, W. J. G., McGaugh, S. S., Bosma, A., & Rubin, V. C. 2001, ApJ, 552, L23

del Burgo, C., Peletier, R. F., Vazdekis, A., Arribas, S., & Mediavilla, E. 2001, MNRAS, 321, 227

Diemand, J., Kuhlen, M., & Madau, P. 2006, ApJ, 649, 1

—. 2007, ApJ, 657, 262

Diemand, J., Kuhlen, M., Madau, P., Zemp, M., Moore, B., Potter, D., & Stadel, J. 2008, Nature, 454, 735

Diemand, J., & Moore, B. 2009, ArXiv e-prints

Dimopoulos, S., & Georgi, H. 1981, Nuclear Physics B, 193, 150

Dress, W. B., Miller, P. D., Pendlebury, J. M., Perrin, P., & Ramsey, N. F. 1977, Phys. Rev. D, 15, 9

Driscoll, D. D. et al. 2008, Phys. Rev. D, 78, 087101

Dull, J. D., Cohn, H. N., Lugger, P. M., Murphy, B. W., Seitzer, P. O., Callanan, P. J., Rutten, R. G. M., & Charles, P. A. 1997, ApJ, 481, 267

Edsjö, J., & Gondolo, P. 1997, Phys. Rev. D, 56, 1879

El-Zant, A., Shlosman, I., & Hoffman, Y. 2001, ApJ, 560, 636

El-Zant, A. A., Hoffman, Y., Primack, J., Combes, F., & Shlosman, I. 2004, ApJ, 607, L75

Ellis, J., Hagelin, J. S., Nanopoulos, D. V., Olive, K., & Srednicki, M. 1984, Nuclear Physics B, 238, 453

Ellis, J., Olive, K. A., Santoso, Y., & Spanos, V. C. 2005, Phys. Rev. D, 71, 095007

Essig, R., Sehgal, N., Strigari, L. E., Geha, M., & Simon, J. D. 2010, ArXiv e-prints

Evans, N. W., Ferrer, F., & Sarkar, S. 2004, Phys. Rev. D, 69, 123501

Fegan, S. J., & Vassiliev, V. V. 2005, VERITAS Collaboration Memo

—. 2007, VERITAS Collaboration Memo

Fegan, S. J., & Wood, M. D. 2008, VERITAS Collaboration Memo

Fellhauer, M., Wilkinson, M. I., Evans, N. W., Belokurov, V., Irwin, M. J., Gilmore, G., Zucker, D. B., & Kleyna, J. T. 2008, MNRAS, 385, 1095

Feng, J. L. 2010, ARA&A, 48, 495

Feng, J. L., Su, S., & Takayama, F. 2004, Phys. Rev. D, 70, 075019

Galbraith, W., & Jelley, J. V. 1953, Nature, 171, 349

Gebhardt, K. et al. 2001, AJ, 122, 2469

Geha, M., Willman, B., Simon, J. D., Strigari, L. E., Kirby, E. N., Law, D. R., & Strader, J. 2009, ApJ, 692, 1464

Georgi, H., & Glashow, S. L. 1974, Physical Review Letters, 32, 438

Gnedin, O. Y., Kravtsov, A. V., Klypin, A. A., & Nagai, D. 2004, ApJ, 616, 16

Gondolo, P., Edsjö, J., Ullio, P., Bergström, L., Schelke, M., & Baltz, E. A. 2004, Journal of Cosmology and Astro-Particle Physics, 7, 8

Gondolo, P., & Silk, J. 1999, Physical Review Letters, 83, 1719

Graham, A. W., Merritt, D., Moore, B., Diemand, J., & Terzić, B. 2006, AJ, 132, 2701

Grasso, D. et al. 2009, Astroparticle Physics, 32, 140

Green, A. M., Hofmann, S., & Schwarz, D. J. 2005, Journal of Cosmology and Astro-Particle Physics, 8, 3

Griest, K., & Kamionkowski, M. 1990, Physical Review Letters, 64, 615

Gustafsson, M., Fairbairn, M., & Sommer-Larsen, J. 2006, Phys. Rev. D, 74, 123522

Haber, H. E., & Kane, G. L. 1985, Phys. Rep., 117, 75

Hall, J., Vassiliev, V. V., Kieda, D. B., Moses, J., Nagai, T., & Smith, J. 2003, in International Cosmic Ray Conference, Vol. 5, International Cosmic Ray Conference, 2851–+

Hanna, D., McCann, A., McCutcheon, M., & Nikkinen, L. 2010, Nuclear Instruments and Methods in Physics Research A, 612, 278

Harris, W. E. 1996, AJ, 112, 1487

Hays, E. 2008, in International Cosmic Ray Conference, Vol. 3, International Cosmic Ray Conference, 1543–1546

Heck, D., Knapp, J., Capdevielle, J. N., Schatz, G., & Thouw, T. 1998, CORSIKA: a Monte Carlo code to simulate extensive air showers.

Hernquist, L. 1990, ApJ, 356, 359

Hillas, A. M. 1985, in International Cosmic Ray Conference, ed. F. C. Jones, 445–448

Hisano, J., Matsumoto, S., & Nojiri, M. M. 2004, Physical Review Letters, 92, 031303

Hofmann, W., & H. E. S. S. Collaboration. 2003, in International Cosmic Ray Conference, Vol. 5, International Cosmic Ray Conference, 2811–+

Holder, J. et al. 2006, Astroparticle Physics, 25, 391

Hooper, D., Blasi, P., & Dario Serpico, P. 2009, Journal of Cosmology and Astro-Particle Physics, 1, 25

Hooper, D., & Profumo, S. 2007, Phys. Rep., 453, 29

Irwin, M., & Hatzidimitriou, D. 1995, MNRAS, 277, 1354

Irwin, M. J. et al. 2007, ApJ, 656, L13

Jarrett, T. H., Chester, T., Cutri, R., Schneider, S. E., & Huchra, J. P. 2003, AJ, 125, 525

Joseph, C. L. et al. 2001, ApJ, 550, 668

Jungman, G., Kamionkowski, M., & Griest, K. 1996, Phys. Rep., 267, 195

Kleyna, J., Wilkinson, M. I., Evans, N. W., Gilmore, G., & Frayn, C. 2002, MNRAS, 330, 792

Kleyna, J. T., Wilkinson, M. I., Gilmore, G., & Evans, N. W. 2003, ApJ, 588, L21

Klypin, A., Zhao, H., & Somerville, R. S. 2002, ApJ, 573, 597

Kolb, E. W., & Turner, M. S. 1990, The early universe

Komatsu, E. et al. 2009, ApJS, 180, 330

Kowalski, M. et al. 2008, ApJ, 686, 749

Krawczynski, H., Carter-Lewis, D. A., Duke, C., Holder, J., Maier, G., Le Bohec, S., & Sembroski, G. 2006, Astroparticle Physics, 25, 380

Lauer, T. R., Faber, S. M., Ajhar, E. A., Grillmair, C. J., & Scowen, P. A. 1998, AJ, 116, 2263

Lavalle, J. et al. 2006, A&A, 450, 1

Lebedenko, V. N. et al. 2009, Phys. Rev. D, 80, 052010

Łokas, E. L. 2002, MNRAS, 333, 697

Łokas, E. L., Mamon, G. A., & Prada, F. 2005, MNRAS, 363, 918

Martin, N. F., de Jong, J. T. A., & Rix, H. 2008, ApJ, 684, 1075

Martin, N. F., Ibata, R. A., Chapman, S. C., Irwin, M., & Lewis, G. F. 2007, MNRAS, 380, 281

Martinez, G. D., Bullock, J. S., Kaplinghat, M., Strigari, L. E., & Trotta, R. 2009, Journal of Cosmology and Astro-Particle Physics, 6, 14

Mashchenko, S., Couchman, H. M. P., & Wadsley, J. 2006a, Nature, 442, 539

Mashchenko, S., & Sills, A. 2005a, ApJ, 619, 243

—. 2005b, ApJ, 619, 258

Mashchenko, S., Sills, A., & Couchman, H. M. 2006b, ApJ, 640, 252

McCann, A., Hanna, D., Kildea, J., & McCutcheon, M. 2010, Astroparticle Physics, 32, 325

Merritt, D., & Cruz, F. 2001, ApJ, 551, L41

Merritt, D., Ferrarese, L., & Joseph, C. L. 2001, Science, 293, 1116

Merritt, D., Graham, A. W., Moore, B., Diemand, J., & Terzić, B. 2006, AJ, 132, 2685

Milosavljević, M., Merritt, D., Rest, A., & van den Bosch, F. C. 2002, MNRAS, 331, L51

Moore, B. 1996, ApJ, 461, L13+

Moskalenko, I. V., & Strong, A. W. 1998, ApJ, 493, 694

Muñoz, R. R., Carlin, J. L., Frinchaboy, P. M., Nidever, D. L., Majewski, S. R., & Patterson, R. J. 2006, ApJ, 650, L51

Muñoz, R. R. et al. 2005, ApJ, 631, L137

Navarro, J. F., Frenk, C. S., & White, S. D. M. 1997, ApJ, 490, 493

Navarro, J. F. et al. 2004, MNRAS, 349, 1039

—. 2010, MNRAS, 402, 21

Niederste-Ostholt, M., Belokurov, V., Evans, N. W., Gilmore, G., Wyse, R. F. G., & Norris, J. E. 2009, MNRAS, 398, 1771

Nilles, H. P. 1984, Phys. Rep., 110, 1

Nolta, M. R. et al. 2009, ApJS, 180, 296

Norris, J. E., Gilmore, G., Wyse, R. F. G., Wilkinson, M. I., Belokurov, V., Evans, N. W., & Zucker, D. B. 2008, ApJ, 689, L113

Pagels, H., & Primack, J. R. 1982, Physical Review Letters, 48, 223

Palma, C., Majewski, S. R., Siegel, M. H., Patterson, R. J., Ostheimer, J. C., & Link, R. 2003, AJ, 125, 1352

Particle Data Group et al. 2008, Physics Letters B, 667, 1

Peccei, R. D., & Quinn, H. R. 1977, Phys. Rev. Lett., 38, 1440

Peebles, P. J. E. 1984, ApJ, 277, 470

Petriello, F. J., & Zurek, K. M. 2008, Journal of High Energy Physics, 9, 47

Piatek, S., Pryor, C., Armandroff, T. E., & Olszewski, E. W. 2002, AJ, 123, 2511

Picozza, P. et al. 2007, Astroparticle Physics, 27, 296

Preskill, J., Wise, M. B., & Wilczek, F. 1983, Physics Letters B, 120, 127

Press, W. H. 2002, Numerical recipes in C++ : the art of scientific computing, ed. Press, W. H.

Pühlhofer, G. et al. 2003, Astroparticle Physics, 20, 267

Rebillot, P. F., Buckley, J. H., Dowkontt, P., & Kosack, K. 2003, in International Cosmic Ray Conference, Vol. 5, International Cosmic Ray Conference, 2827–+

Reid, B. A. et al. 2010, MNRAS, 404, 60

Riess, A. G. et al. 2009, ApJ, 699, 539

Roache, E., Irvin, R., Perkins, J. S., & et al. 2008, in International Cosmic Ray Conference, Vol. 3, International Cosmic Ray Conference, 1397–1400

Romano-Díaz, E., Shlosman, I., Heller, C., & Hoffman, Y. 2009, ApJ, 702, 1250

—. 2010, ApJ, 716, 1095

Romano-Díaz, E., Shlosman, I., Hoffman, Y., & Heller, C. 2008, ApJ, 685, L105

Roszkowski, L., Ruiz de Austri, R., & Trotta, R. 2007, Journal of High Energy Physics, 7, 75

Rubin, V. C., & Ford, Jr., W. K. 1970, ApJ, 159, 379

Saitoh, T. R., Koda, J., Okamoto, T., Wada, K., & Habe, A. 2006, ApJ, 640, 22

Sánchez-Conde, M. A., Prada, F., Łokas, E. L., Gómez, M. E., Wojtak, R., & Moles, M. 2007, Phys. Rev. D, 76, 123509

Sanglard, V. et al. 2005, Phys. Rev. D, 71, 122002

Savage, C., Freese, K., Gondolo, P., & Spolyar, D. 2009a, Journal of Cosmology and Astro-Particle Physics, 9, 36

Savage, C., Gelmini, G., Gondolo, P., & Freese, K. 2009b, Journal of Cosmology and Astro-Particle Physics, 4, 10

Scannapieco, C., White, S. D. M., Springel, V., & Tissera, P. B. 2009, MNRAS, 396, 696

Schnee, R. W. et al. 2005, in Dark matter in astro- and particle physics, ed. H. V. Klapdor-Kleingrothaus & R. Arnowitt, 259–268

Scott, P., Conrad, J., Edsjö, J., Bergström, L., Farnier, C., & Akrami, Y. 2010, Journal of Cosmology and Astro-Particle Physics, 1, 31

Seljak, U., Makarov, A., McDonald, P., & Trac, H. 2006, Physical Review Letters, 97, 191303

Servant, G., & Tait, T. M. P. 2003, Nuclear Physics B, 650, 391

Shetrone, M. D., Côté, P., & Sargent, W. L. W. 2001, ApJ, 548, 592

Siegel, M. H., Shetrone, M. D., & Irwin, M. 2008, AJ, 135, 2084

Simon, J. D. et al. 2010, ArXiv e-prints

Spooner, N. J. C. 2007, Journal of the Physical Society of Japan, 76, 111016

Springel, V. et al. 2008a, MNRAS, 391, 1685

—. 2008b, Nature, 456, 73

Steigman, G. 2007, Annual Review of Nuclear and Particle Science, 57, 463

Strigari, L. E., Bullock, J. S., Kaplinghat, M., Simon, J. D., Geha, M., Willman, B., & Walker, M. G. 2008a, Nature, 454, 1096

Strigari, L. E., Koushiappas, S. M., Bullock, J. S., & Kaplinghat, M. 2007, Phys. Rev. D, 75, 083526

Strigari, L. E., Koushiappas, S. M., Bullock, J. S., Kaplinghat, M., Simon, J. D., Geha, M., & Willman, B. 2008b, apj, 678, 614

Taoso, M., Bertone, G., & Masiero, A. 2008, Journal of Cosmology and Astro-Particle Physics, 3, 22

Thompson, D. J. et al. 1995, ApJS, 101, 259

Tikhonov, A. N., & Arsenin, V. 1977, Solutions of Ill-Posed Problems (Washington, DC, Winston & Sons)

Tissera, P. B., White, S. D. M., Pedrosa, S., & Scannapieco, C. 2010, MNRAS, 406, 922

Tolstoy, E., Hill, V., & Tosi, M. 2009, ARA&A, 47, 371

Tyler, C. 2002, Phys. Rev. D, 66, 023509

Ullio, P., & Bergström, L. 1998, Phys. Rev. D, 57, 1962

Ullio, P., Zhao, H., & Kamionkowski, M. 2001, Phys. Rev. D, 64, 043504

van den Bosch, R., de Zeeuw, T., Gebhardt, K., Noyola, E., & van de Ven, G. 2006, ApJ, 641, 852

Vassiliev, V. V., & Fegan, S. J. 2005, VERITAS Collaboration Memo

Vassiliev, V. V., & Wood, M. D. 2010, Internal Memo

Walker, M. G., Mateo, M., Olszewski, E. W., Gnedin, O. Y., Wang, X., Sen, B., & Woodroofe, M. 2007, ApJ, 667, L53

Walker, M. G., Mateo, M., Olszewski, E. W., Peñarrubia, J., Wyn Evans, N., & Gilmore, G. 2009, ApJ, 704, 1274

Weekes, T. C. et al. 2002, Astroparticle Physics, 17, 221

—. 1989, ApJ, 342, 379

Weinstein, A. 2008, in International Cosmic Ray Conference, Vol. 3, International Cosmic Ray Conference, 1539–1542

White, R. J., Rose, H. J., Bradbury, S. M., & et al. 2008, in International Cosmic Ray Conference, Vol. 3, International Cosmic Ray Conference, 1527–1530

Wilkinson, M. I., Kleyna, J., Evans, N. W., & Gilmore, G. 2002, MNRAS, 330, 778

Wilkinson, M. I., Kleyna, J. T., Evans, N. W., Gilmore, G. F., Irwin, M. J., & Grebel, E. K. 2004, ApJ, 611, L21

Willman, B. et al. 2005, AJ, 129, 2692

Willman, B., Geha, M., Strader, J., Strigari, L. E., Simon, J. D., Kirby, E., & Warres, A. 2010, ArXiv e-prints

Wood, M. D. et al. 2008, ApJ, 678, 594

Wood, M. D., Fegan, S. J., & Vassiliev, V. V. 2007, VERITAS Collaboration Memo

Wood, M. D., & Vassiliev, V. V. 2009, VERITAS Collaboration Memo

Xue, X. X. et al. 2008, ApJ, 684, 1143

York, D. G. et al. 2000, AJ, 120, 1579

Yüksel, H., Kistler, M. D., & Stanev, T. 2009, Physical Review Letters, 103, 051101

Zwicky, F. 1933, Helvetica Physica Acta, 6, 110